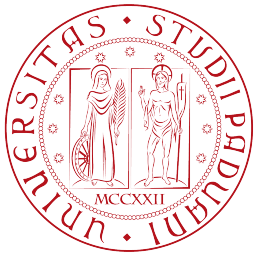

UNIVERSITÀ DEGLI STUDI DI PADOVA

Dipartimento di Fisica e Astronomia "Galileo Galilei"

Master Degree in Physics

Final Dissertation

Modeling of water droplets response in a time- and space-dependent light-induced electric field

Thesis supervisor

Prof.ssa Cinzia Sada

Thesis co-supervisor

Dr. Giovanni Bragato

Candidate

Maddalena De Ros

Academic Year 2022/2023

Contents

Introduction

The idea that physics evolves dynamically is one of crucial importance. Indeed, the continuous endeavor of theory construction is characterized by a dynamic process. As an essential element in constructing theory, scientists rely upon models. Theoretical models constitute a major tool in many aspects of scientific activity. Their purpose is not only to organize or explain data but also, in some cases, to provide useful insight into physical systems or problems that are too complex to be addressed with full details. It is feasible to provide a comprehensive description of a real system by including the maximum number of parameters that can be adjusted. The advantage is that a detailed description is closer to the actual system. However, usually the complexity that characterizes these models makes it impossible to find an analytical solution in certain cases, which is the major drawback. One possible solution is to introduce a simpler model that meets few essential properties of the real system (such as its symmetries) in order to reproduce its main characteristics. It is more likely that the models will be solved analytically by doing so.

With the terms *Electrohydrostatics* (EHS) *Electrohydrodynamics* (EHD) we refer to the study of those phenomena regarding, respectively, the statics and the dynamics of electrically charged fluids. Electrohydrostatic (EHS) and Electrohydrodynamic (EHD) can be nowadays considered as theories, but they both were born as models. Even though there are different possibilities of formulation of problems, electrohydrodynamics concerns for all the interaction between the flow of fluid and the electric field. Early interest in the subject arose from the deformation and rupture of raindrops during storms (Macky, [1]), and the effect of aerosol deformation on optical studies of dispersed systems [2].

Taylor was actually the first to try to expand already-existing, not satisfactory studies in electrohydrostatics in his paper that dates back to 1966, a proposal for a novel model – that will go down in history as the leaky-dielectric model [3] – taking into account some new elements. Despite more than fifty years on, the interaction of weakly conducting fluids with electric fields is still a source of intriguing phenomena and is employed in a variety of fields.

Even if EHD was born as a specific model that aimed to fill in the gaps of the lacking theories, over the years electrohydrodynamic is emerged as a theory on its own. In fact, its governing laws can be presented in a general way and in its most basic formulation, the differential equations describing EHS or EHD come from Stokes equations coupled with Maxwell's equations. In principle, there is no need to refer to a specific, experimental setup addressing a particular problem.
The starting point is generally the formulation of the problem, for which it is necessary to specify the appropriate coordinate system (Cartesian, spherical, cylindrical, ellipsoidal) that will be adopted. This decision will affect the whole derivation of the eventual analytic solution, since equations will be then written in these specific coordinates from the very early beginning. Obviously, such a choice depends on the shape of the drop and has to be suitable to describe the

problem. In most cases is accompanied by some further assumptions (geometrical symmetries, discard of nonlinear effects, limited range for certain parameters), whose goal is to simplify even more the equations in order to increase the possibility of finding analytical solutions.

As far as more complex situations are involved – and that is actually the case of almost all real systems – just a few (if any) attempts have been done to extend or at least examine the limitations of EHS/EHD theories to describe such problems. This can be better justified if one considers that normally these situations are solved by means of numerical simulations. The issue is that numerical simulations rely on theory, too: therefore, systems can be simulated only under certain specific conditions, which are not always satisfied by all real devices. For example, the majority of the simulations taking into account external confinement of the outer fluid (a situation that is very frequent in microfluidic devices) considers for simplicity small drops placed at the center of the confinement system. Despite being insightful, this is quite distant from reality, where drops are instead large entities occupying a big portion of the cross section of the channel.

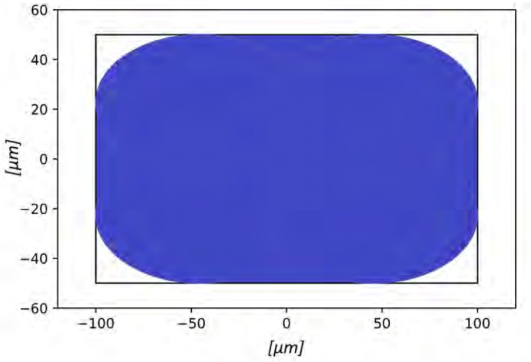

An example of real droplet [4].

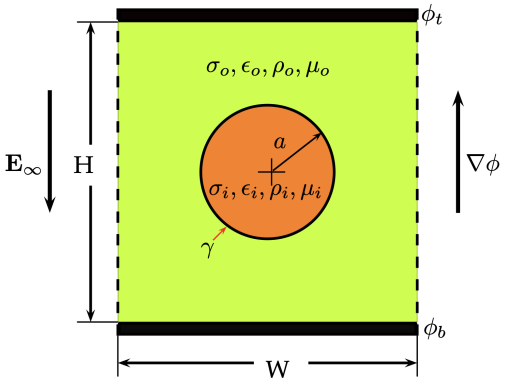

An example of a droplet in a computational simulation [5].

In the right picture, ρ, μ, σ, ϵ and γ represents, respectively, the density, the viscosity, the electric conductivity, the electric permittivity and the surface tension.

There is therefore a need to extend existing theoretical models or at least to analyze their strengths, limitations and weaknesses in order to pave the way for the development of more complicated analytical models, on the basis of which essential features of more complex phenomena can be captured and new numerical simulations can be performed. This thesis aims primarily at addressing this issue: this is obtained by the comparison with data coming from measurements of the response of water droplets to a time-varying, spatially nonuniform electric field. The research is based on a wide-ranging scientific project taking place at UNIPD that has already developed several new methods of real-time detection and monitoring of micro and submicrometric objects dispersed in fluid media.

Microfluidics holds great promise as it can perform typical laboratory applications using a fraction of the volume of fluids and allows for investigation of unexpected effects due to the different surface-to-volume ratio that are not detectable in the macro-scale[1]. On-chip droplet enhanced fluorescence emission for low concentration of fluorescent constituents has been recently demonstrated thanks to the light confinement by total internal reflection as well as the

[1]In fact, micron-sized liquid droplets exhibit unique optical properties, including lower threshold energies for non-linear optical processes than those observed in the bulk liquid phase

excitation of Whispering Gallery Modes (WGMs), i.e electromagnetic waves guided by total internal reflection around a circumference close to the surface of the resonator [6].
These pioneering works have paved the way to the exploitation of liquid droplet resonators with great interest for applications in biological, chemicals detection and measurements [7]. It is however known that in microfluidics, droplets suffer from size's distribution, a critical aspect when matching conditions to get WGMs are quite restrictive in terms of size requirements. Droplets should have the correct size to support WGMs and actually this requirement still represents the most limiting and hindering factor. The UNIPD Opto-microfluidic group has therefore started a pioneering project to verify whether this limiting factor can be bypassed by finely tune the droplet size on demand.

The basic idea relies on the experimental observation that light induced phenomena such as the photovoltaic effect can generate local electric fields. The last, if intense enough and suitably oriented, can move isolated droplets and shape changes have been detected. No data are instead available on droplets immersed and moving in another liquid phase as in the case of droplets microfluidics. The project aimed to test whether photoinduced local electric fields can be strong enough to change a droplet size when it moves immersed in another phase (said continuous phase) inside a microfluidic channel. Although screening effects could have been claimed as hindering factors, the experimental data showed photovoltaic local electric field if properly generated are responsible for droplets elongation of 3-4 %, enough to match the WGMs conditions. Real measurements for this elongation – whose physical origin has yet to be understood in detail – are used to compare the analytical results of already-existing theoretical models presented in the first place.

In this thesis, three chapters are presented:

- *Chapter 1* contains the main theoretical elements to deal with elecrohydrostatic and elecrohydrodynamic, namely the.
- In *Chapter 2*, some particular cases of analytically solvable EHD problems are presented. For some of them, a detailed solution is shown. A significant number of them is devoted to spherical droplets, which are the most studied in literature due to their geometrical simplicity. The cases of a cylinder with circular and an elliptic cross section are also analyzed and the former is solved in detail.
- The last one, *Chapter 3*, contains an insightful comparison with real data coming from measurements of the response of microfluidic water droplets to a time-varying, spatially nonuniform electric field of a particular system; in the perspective of the necessity to revise some already-existing theoretical models to expand their validity, some novel improvements are presented.

Chapter 1

A theoretical overview

The attempt to analytically model the response of water droplets in an electric field is not only about theoretical considerations on the field and the drop: it includes the estimation of the intensity and field distribution in time and space as well as its effects on the droplet and its response.
Theoretical treatment is therefore required for each of these three aspects.

1.1 The electric field and the shape of the drop

As far as the **electric field** is concerned, two main characteristics emerge among several ones:

- the time variation of the field; with "time variation" we mean that the intensity of the external imposed field is not constant but rather depends on time: $E_\infty(t)$ is a generic function of time (a periodic or non periodic one).

- The space dependence of the field. Even if spatial nonuniformity of the field is always present in real situations and is mainly due to fringing effects, generally electric fields are treated as *it were* uniform in the region of application by choosing appropriate approximations. Consequently, the space dependence of the field is employed when attempting to provide a more faithful description of a physical situation at the cost of dealing with a more complicated treatment, both from a conceptual and a mathematical perspective.

In this way, the electric field may be written as a generic function of space $\mathbf{r} = (x, y, z)$ and time t, $E(\mathbf{r}, t)$. A simplifying hypothesis may be then:

$$E(\mathbf{r}, t) = f(\mathbf{r})E(t) = f(x, y, z)E(t) \tag{1.1}$$

i.e. by separation of variables; $\mathbf{r}$ and t are thus independent. Such approximation must be justified on the basis of the physical situation one considers.
If one wants to treat analytically the problem of the interaction between a drop of fluid an the electric field, an expression for its space dependency has to be given in order to solve the Laplace's equation,

$$\nabla^2 V = 0$$

with pertinent boundary conditions (in this regard, see section 1.4).

The first attempt to provide a general theoretical treatment for nonuniform fields has been presented by Feng [8], who proposed an analytic form for the external electric potential suitable for the case of spatial nonuniformity:

$$V(r,\theta) = -E_\infty[rP_1(\cos\theta) + \Lambda r^2 P_2(\cos\theta)], \tag{1.2}$$

where the expression is given in a spherical coordinate system assuming axisymmetric behavior with respect to ϕ, Λ is a measure of the relative magnitude of the field nonuniformity (trivially, if $\Lambda = 0$ one regains the uniform case) and $P_l(\cos\theta)$ are the Legendre polynomials[1].
The applied electric field is therefore seen as a linear combination of uniform and quadrupole components, which results in a nonuniform but axisymmetric electric field. Of many possibilities, the combination of $P_1(\cos\theta)$ and $P_2(\cos\theta)$ can actually be considered as the simplest one. As we will see in the following, the latter may not be the only possibility for the analytic expression for a nonuniform field.

The **shape of droplets** is usually modeled as a very complicated three-dimensional figure that can not be described by theoretical shapes. If one is interested in the possibility of solving the equations analytically, there are some standard shapes to be considered:

- a sphere, the easiest shape for the drop since it is symmetrical in all directions;
- a cylinder, which is usually employed to describe liquid jets/columns or long drops;
- a spheroid, a geometric shape that resembles a sphere in three dimensions, but has a slight flattening at the poles or bulging at the equator. All points on the surface of the spheroid are equidistant from a central point, but not necessarily from the center, as defined by its semi-major and semi-minor axes;
- an ellipsoid, that is in turn defined by semi-axes, which are in general three and are not necessarily equal. Unlike a spheroid, an ellipsoid can be elongated or squashed in any direction, not just at the poles or equator. The center of an ellipsoid may not always be the center of symmetry.

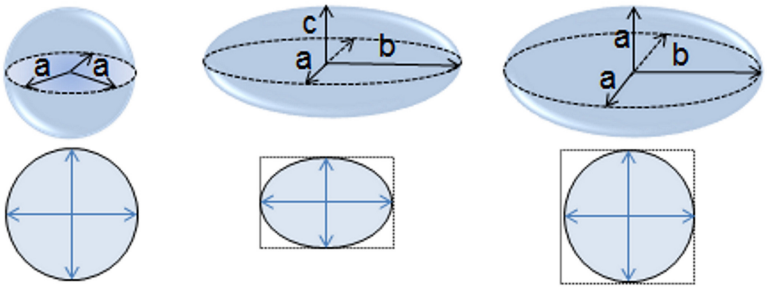

Figure 1.1: On the left, a sphere. In the middle, an ellipsoid and on the right a spheroid. Taken from [9].

However, as far as an analytical solution is concerned, the sphere and the cylinder are the most common shapes adopted to mime dynamics of the fluid-field interaction due to their simplicity with respect to the spheroid and the ellipsoid (e.g. the Laplacian operator expressed in spherical/cylindrical coordinates is much easier than the one used in the elliptic case).

[1] In this work we will only need two of them, specifically: $P_1(\cos\theta) = \cos\theta$ and $P_2(\cos\theta) = (3\cos^2\theta - 1)/2$.

We conclude this section with the definition of a parameter that is important for this type of problems, $\mathcal{D}_T$. It is called *Taylor's deformation*, since it was Taylor the one who first introduced it. For two-dimensional systems, it is defined as:

$$\mathcal{D}_T = \frac{r_\parallel - r_\perp}{r_\parallel + r_\perp} \tag{1.3}$$

where $r_\parallel$ and $r_\perp$ are the droplet axes parallel and perpendicular to the direction of the field. Note that, to simplify the notation the subscript T may be omitted when doing mathematical computations.

The choice of defining $\mathcal{D}$ as a theoretical parameter stems from the need to identify a common parameter for the shape that is adopted to model the interface of the drop. In fact, EHD theory has been "built" in such a way that $\mathcal{D}$ can be determined by properly solving the equations, being therefore a standard, non dimensional quantity expressing a degree of deformation.
In this perspective, since $\mathcal{D}$ refers to two-dimensional drops of circular shape deforming into a two-dimensional ellipsoid, it follows that: in the case of a three-dimensional droplet, $\mathcal{D}$ can be employed carefully bearing in mind its geometrical meaning (it quantifies the deformation of circular cross sections and not of the whole shape). Again, in the case of a three-dimensional drop, $\mathcal{D}$ may not be an appropriate parameter to model the deformation of the droplet (each problem has to be treated carefully).

1.2 Interfaces and surface tension: essential elements

Interfaces are another key element of the problem. On this regard, one needs to develop a suitable treatment for analytically handling those forces, e. g. surface tension, that are typically ignored at the macroscopic level but have a significant impact on the understanding of the dynamics of the interaction between drops of fluid and electric fields.
In mathematical terms, in our context an interface is the geometrical surface that separates two fluid domains. The definition implies that an interface is neither thick nor smooth (i.e., has no roughness). Reality is more complicated, since separating two immiscible fluids is a result of both molecular interactions between the molecules of each fluid and Brownian diffusion (that is, thermal agitation) [10].
In figure 1.2 a schematic view of an interface at the molecular size is provided. On the right, in figure 1.3, its macroscopic counterpart for the interface of a drop [10] is represented.

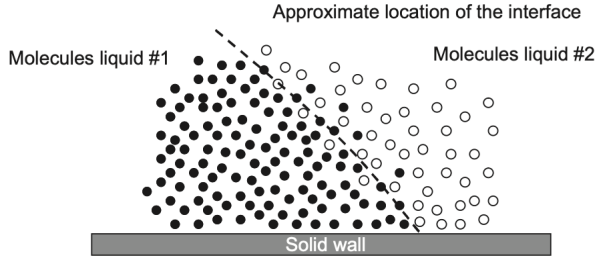

Figure 1.2: Microscopic interface.
Source: [10].

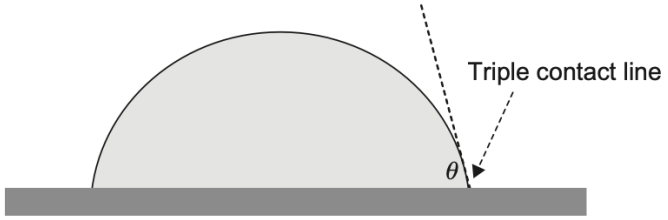

Figure 1.3: Macroscopic interface.
Source: [10]

Let us start by describing the concept of curvature.

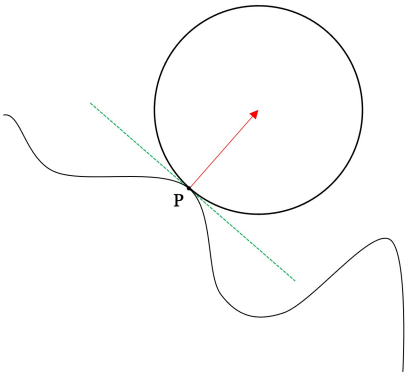

Figure 1.4: Schematic representation for the curvature.

For a planar curve, the curvature is defined as:

$$\kappa := \frac{1}{r} \tag{1.4}$$

where r is the radius of the osculating circle that is closest to the curve at the contact point P. It also referred as radius of curvature and is a *signed* quantity, meaning that it can assume positive or negative value (so also the curvature does, depending on the curve being concave or convex).

It has been demonstrated that [10]:

- for a parametric curve, $c(t) = (x(t), y(t)$ it results that:

$$\kappa = \frac{\dot{x}\ddot{y} - \dot{y}\ddot{x}}{(\dot{x}^2 + \dot{y}^2)^{3/2}}; \tag{1.5}$$

- for plane curve given in an implicit form, $f(x, y) = 0$ it is the divergence of the direction of the gradient of the function f then:

$$\kappa = \nabla \cdot \left(\frac{\nabla f}{||\nabla f||} \right); \tag{1.6}$$

- plane curve given in an explicit form:

$$\kappa = \frac{\mathrm{d}^2 y/\mathrm{d}x^2}{[1 + (\mathrm{d}y/\mathrm{d}x)^2]^{3/2}}; \tag{1.7}$$

- surface:

$$\kappa = \frac{1}{2}\left(\frac{1}{R_1} + \frac{1}{R_2} \right) \tag{1.8}$$

  where $R_{1,2}$ are, respectively, the two principal radii of curvature of the specific, chosen surface [10].

Note that for simplicity of notation, in all the equations (1.5) - (1.8) the dot over a quantity is used ad the time differentiation.

Now it is possible to state (details for derivation can be found, for example, in [10]) that a simple mathematical equation describing the capillary pressure difference ΔP that is maintained across the interface between two static fluids due to surface tension holds:

$$\Delta P = \gamma \left(\frac{1}{R_1} + \frac{1}{R_2} \right) \tag{1.9}$$

which is the Laplace and Young's law, one of essential importance when addressing interfaces because it links the pressure inside a droplet to its curvature.

1.3 Droplet response

With the terms *Electrohydrostatics* (EHS) *Electrohydrodynamics* (EHD) we refer to the study of those phenomena regarding, respectively, the statics and the dynamics of electrically charged fluids.
If an electric field is established in a region where two immiscible fluids are separated by an interface, one observes a jump in it. This is caused by the difference in the physical (dielectric) properties from one medium to the other one. Among all the various consequences of such a field discontinuity, we can emphasize the emerging of an electric stress on the fluid-fluid interface. The curvature of the interface of a droplet suspended in an uniform electric field, for example, produces surface gradients of the electric that are likely to establish a deformation of the droplet or even break it.

1.3.1 The birth of EHD

As far as we know, it was William Gilbert that first reported on electrohydrodynamics: in his seventeenth century treatise *de Magnete* one can read about the formation of a conical shape upon bringing a charged rod above a sessile drop [11].
Some work was later done by Rayleigh in the nineteenth century: he addressed droplet dynamics in terms of surface tension offsets due to interfacial charges. All subsequent studies concentrated mainly either on perfect conductor fluids (such as water or mercury) or on perfect apolar liquids (so perfect dielectrics like benzene).

Considering the two fluids as ideally insulating dielectrics – or if the drop and the ambient fluid can be regarded as a perfect *conductor-insulator* system – in the absence of free charge, electrostatic theory is used to make predictions on such a system. In fact, in the easiest case, the surface tension might balance it and the system may reach a steady state. Consequently, one refers to *electrohydrostatics* to indicate such steady states, which are characterized by the fact that both phases are at rest.
In this static case, theory predicts that the interfacial stress (that actually is an electric pressure) will be perpendicular to the surface and oriented such that it will be directed from the fluid of higher permittivity/resistivity to the lower one. Lastly, according to EHS, in this case the drop will **always** deform into a prolate ellipsoid [11].

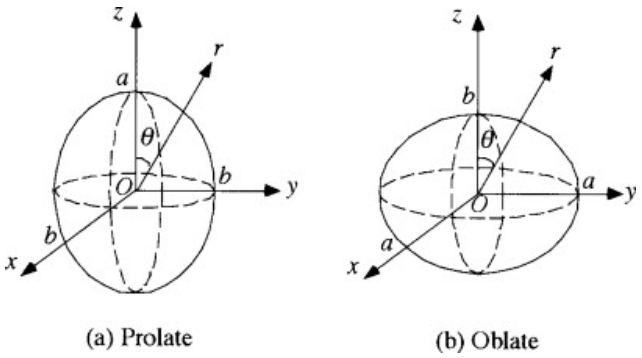

Figure 1.5: A simple, schematic representation of a prolate and an oblate shape for an ellipsoid, source: [12].

Despite its simplicity, the above description is not that attainable, since both fluids need to be considered as slightly conducting to mach reality. The two liquids need to be given a

finite value of permittivity and conductivity. In this case, there will be an accumulation of free charge at the interface and the electric field will act on those.
A tangential interfacial stress on the interface has to be added to the already-existing electric pressure. The imbalance in the electrical shear stresses[2] is compensated by hydrodynamic shear ones at equilibrium. In an attempt to account for this effect, one comes to the simple but crucial conclusion. The new electric stress has to be balanced by "something different" and it is also possible that it leads to new types of deformation.

This reasoning encodes the essence of what is known as *electrohydrodynamics*, which can be dated back to the appearance of a seminal work by Taylor in 1966. The latter actually contained the so-called *leaky-dielectric model* and followed 1962 experimental studies on poorly conducting liquids by Allan and Mason, who reported some anomalous behavior of fluid deformation. As already mentioned, EHS was predicting that a drop would have always deformed into a prolate ellipsoid. On the contrary, Allan and Mason observed some drops of certain fluids becoming oblate – meaning that their major axes was perpendicular to the direction of the field – thus violating theoretical expectations. Taylor was actually the first to address that "something different" we mentioned earlier to balance the tangential electric stress and justify Allan and Mason findings. He identified it as fluid motion inside and outside the drop.

Both the stability and the deformation of a drop as a consequence of the interaction with an electric field have been extensively treated in literature and research is still being conducted. The following table, that is by no means exhaustive, summarizes the most relevant results [14], [15]:

EHS	Experimental work:	Allan and Mason (1962); Torza *et al.* (1971); Vizika and Saville (1992).
	Theoretical modelling:	Allan and Mason (1962); Taylor (1964).
EHD	Theoretical modelling:	Taylor (1966); Torza *et al.* (1971); Ajayi (1978); Baygents *et al.* (1989).
	Numerical simulation:	Feng and Scott (1996;) Feng (1999).
	Reviews:	Melcher and Taylor (1969); Saville (1997).

If Taylor can be considered without a doubt the father of the leaky-dielectric model, Melcher is the one who employed it extensively to develop EHD. A crucial paper is in fact the review by both Taylor and Melcher that dates back to 1969 and actually defines the field of electrohydrodynamics. In 1971 some experiments by Torza *et al.* pointed out new mismatches between theory and experiments. The model was extended and improved both by Ajayi[3] and Baygents *et al*[4]. New experiments were than performed in 1992 by Vizika and Saville and they reported good agreement with updated theoretical models.

[2]Shear stress is a coplanar element of stress with a cross-section of a material. It derives from the shear force, which is the component of the force vector parallel to the transverse section of the material. [13].

[3]He worked and succeeded in including higher order terms into Taylor's linearized theory.

[4]They analyzed a specific issue highlighted by Torza *et al.* by replacing the leaky-dielectric model by an elecrokinetic.

1.4 Fundamental equations ruling the theory

In its most basic formulation, the differential equations describing electrohydrodynamics come from equations describing the conservation of mass and momentum for the fluid (Stokes equations), coupled with Maxwell's equations. Even if there are different possibilities for problem formulation for all of them (as one can see from the diagram below), electrohydrodynamic concerns the interplay between fluid flow and electric field: as a consequence, the laws governing EHD can be presented in a general way.

The coupling between electric and mechanical phenomena occurs at fluid-fluid interface. As noted earlier, if one considers perfect conductors or dielectrics, only the component of the electric stress perpendicular to the interface is nonzero; the latter is balanced by both modifications of the shape of the interface and interfacial tension changes. On the contrary, leaky dielectrics fluids are characterized by the accumulation of an amount of free charge and this alters the field. Moreover, a viscous flow arises to balance the action of the tangential components of the field, which now are nonzero, too [11].

1.4.1 Notation and scale analysis

The electrohydrodynamic theory analyzes systems of drops of one particular fluid – normally the droplet – immersed in another one. Generally, fluids are assumed to be Newtonian[5] and the properties of major interest are their density, ρ and viscosity μ. γ labels the surface tension at the interface of the two fluids. As Feng reports in [8], Newtonian fluids of constant viscosities may be considered as a simple yet adequate first approximation for the EHD theory[6]. Obviously, including of nonlinearities may provide more accurate results than a linearized asymptotic analysis. Nonetheless, physical insights into the primary electrohydrodynamic effects can be gained by analytical solutions of the linearized problem and provide invaluable guidance for more comprehensive numerical computations.

As for the electrical properties, the two relevant ones are usually the electric conductivity σ and the electric permittivity ϵ, which are assumed to be constant for the two fluids.
Several notations (for example, barred/unbarred characters or specific subscripts) are employed to indicate the characteristics of the two fluids. In this work, we adopt hereafter the following notation: a subscript i will indicate the "inner" fluid – that of which the drop is made of, also named "dispersed phase" – whereas o will be used for the "outer" one – namely the external fluid containing the drop, also named "continuous phase".

Capital letters are used to denote specific ratios of these physical properties:

$$R = \frac{\sigma_i}{\sigma_o} \quad \text{and} \quad S = \frac{\epsilon_i}{\epsilon_o}$$

$$\lambda = \frac{\rho_i}{\rho_o} \quad \text{and} \quad \eta = \frac{\mu_i}{\mu_o}.$$

[5] A fluid is said to be *Newtonian* if the viscous stresses that arises due to its flow is linearly correlated to the local strain rate – which is the rate of change of the fluid deformation with respect to time – at every point of the fluid [13].

[6] Feng in [8] writes "*Even for Newtonian fluids, nonlinearities may appear in general governing equations because of the fluid inertia and the capillarity of deformable fluid interfaces. [...] Nonlinearities may also arise from the charge convection by fluid flow at the interface, which have not been rigorously investigated in existing theoretical work*".

For example, if $\eta \to 0$ a bubble is being considered, whereas if $\eta \to \infty$ the drop becomes a rigid particle. In many cases, the drop is considered to be neutrally buoyant, meaning that the effect of gravity on it can be neglected. With respect to what we have stated above, this can be achieved theoretically by setting $\lambda = 1$ [11], [14], [16].

Fluids can be classified in terms of electric conductivity σ and the dielectric constant $\epsilon_r = \epsilon/\epsilon_0$ as

- conductor: $\sigma \gg 1$, $\epsilon_r = 1$;
- dielectric (insulator): $\sigma \ll 1$, $\epsilon_r \geq 1$.

Moreover, one can distinguish between:

- perfect dielectrics fluids, meaning that the fluids are either perfect conductor or on perfect apolar liquids;
- leaky dielectrics fluids, where both fluids are considered to be slightly conducting.

Lastly, note that $[[X]]$ is the notation employed to indicate the variation of a generic quantity $X - [[X]] = X_i - X_o$ across the interface of the drop.

When dealing with EHD problems it is possible to perform a so called *scale* analysis, based on the following considerations:

- the electric field is scaled by the intensity of the external applied field, E_∞;
- the natural scale for lengths depends on the conditions of the external fluid:
  - unbounded situation, in which the natural length scale is given by the initial characteristic length of the drop (e. g. the initial radius r_0 in case of a sphere);
  - bounded situation; in this case, the typical length can not be established *a priori*, since the length scale has to be determined specifically for the problem depending on the type of confinement to which the physical system is subjected. Unfortunately, no comprehensive analytical model exists for *bounded* situations, which have been mainly addressed by means of numerical simulations and are currently being studied.
- the natural scale for velocities depends on the conditions of flow:
  - if the drop is suspended (that is, it does not move), there is no natural velocity, so one can be defined as [7] as $u_s = \dfrac{\epsilon (E_\infty)^2 r_0}{\mu}$;
  - if there is a background flow, the velocity is scaled by means of the characteristic velocity u_c of the imposed field.

Physical properties and dimensional analysis let us define four dynamical parameters:

$$Ca_{el} = \frac{\mu_o u_s}{\gamma}, \qquad Re_{el} = \frac{u_s \epsilon_o}{\sigma_o r_0}, \qquad Re_{fl} = \frac{\rho_o r_0 u_s}{\mu_o} \quad \text{and} \quad M = \frac{r_0 \epsilon_o E_\infty^2}{\mu_e u_c} \tag{1.10}$$

[7] Anticipating what we will see in the next section, the presented formula can be obtained by simple rearrangement of the balance of two stresses, the electric and the hydrodynamic shear stress, respectively $\tau^e_{r\theta} = \epsilon (E_\infty)^2$ and $\tau^h_{r\theta} = \mu u_s / r_0$.

which are obtained by specific ratios and thus have an interesting physical interpretation. Ca_{el}, the capillary number, is the ratio between the viscous force and the surface tension, signifying then the relative strength of the viscous stress in deforming the the interface of the drop with respect to the resistance to deformation due to surface tension.
Re_{el}, the so-called electric Reynolds number, comes from the ratio of two time scales: the one of charge relaxation from the fluid bulk to the interface, ϵ/σ and the time-scale of charge convection by the flow, r_0/u_s. Re_{fl} is the flow Reynolds number, representing the ratio of inertia force to the viscous force. Lastly, the Mason number M quantifies the relative importance of the electrical stress as compared with the viscous one.

Scaling yields five dimensionless groups [14]. Three of them are provided by R, S and η. The remaining two can be chosen as Ca_{el} and M, for example.
Re_{fl}, Re_{el} and Ca_{el} play a crucial role, since electrohydrodynamics equations can be analytically solved only if [16]:

$$Ca_{el} \ll 1 \qquad Re_{el} \ll 1 \qquad Re_{fl} \ll 1 \tag{1.11}$$

meaning respectively that the deformation of the surface of the drop is small, that the time scale of charge relaxation is much less than the time-scale of charge convection and that inertial forces can be safely ignored.

1.4.2 Flows of fluids

As far as flows are concerned, one has to consider the following equations:

$$\nabla \cdot \mathbf{u} = 0 \tag{1.12}$$

and

$$-\nabla p + \mu \nabla^2 \mathbf{u} + \mathbf{F^e} = 0 \tag{1.13}$$

expressing, respectively, conservation of mass and momentum. Note that $\mathbf{u}$ is the fluid velocity, p indicates the pressure and $\mathbf{F^e}$ corresponds to the electric force per unit area (equivalently, per unit volume if the system under study is a three-dimensional one). ∇^2 stands for the Laplacian operator, which can be expressed in different coordinate systems (Cartesian, polar, cylindrical) according to one's needs.

In order to solve the momentum and continuity equation, is also possible to write an equation for the so-called *streamfunction*, ψ. The streamfunction formulation makes it possible to reduce the number of equation to be solved. Nevertheless, the consequence is to solve a higher-order differential equation. This is done by taking the curl of (1.19) and considering that:

- the curl of a gradient is zero;
- the curl of the velocity is the vorticity, ω.

so that one has

$$\nabla^4 \omega = 0 \tag{1.14}$$

where ∇^4 is the biarmonic operator [16]. The latter satisfies both the continuity and the momentum equation and can be solved specifically according to the chosen coordinate system by assigning boundary conditions that are specific for an electrohydrodynamic problem.
For further details on the streamfunction-vorticity formulation, see **Appendix A**.

1.4.3 The electric force and field

The fundamentals of electricity and magnetism are stated in Maxwell's equations in a way that is both elegant and concise: the majority of the field's working relationships can be developed through them. Electric and magnetic phenomena are independent under static conditions because their fields are uncoupled [11]. Electrostatic equations provide an accurate approximation because the characteristic time of electrostatic processes is larger than that of magnetic phenomena. So, in the absence of external magnetic fields, magnetic effects can be completely ignored.

The latter can be easily demonstrated as follows [11]. One can start from three characteristic times, τ_C for electric phenomena

$$\tau_C := \frac{\epsilon\epsilon_0}{\sigma}, \tag{1.15}$$

τ_M for magnetic ones,

$$\tau_M := \mu\mu_0\sigma l^2 \tag{1.16}$$

where l^2 is the square of a characteristic length, and τ_P for the time-scale of transport process[8].

A process is said to be slow if $\tau_P \geq \tau_C \gg \tau_M$. Rearrangement of the second inequality can be shown [11] to be equal to:

$$(\epsilon/\mu)^{1/2} \gg l(\mu_0\epsilon_0)^{1/2} \tag{1.17}$$

and since $(\mu_0\epsilon_0)^{-1/2} = c$, being c the speed of light, the factor $l(\mu_0\epsilon_0)^{1/2}$ is very small for the systems that are taken into consideration. Thus, the electrostatic approximation is valid on a millimeter-scale, if the electrical relaxation time τ_C must be longer than 10^{12} s. The inequality is satisfied easily because the conductivity is seldom larger than 1 μS per meter for liquids of the sort under study in EHD [11].

Accordingly to all that has been said, the electric body force on a fluid is made of three components, the Coulomb force – known as electrophoretic one – the dielectrophoretic one and the electrostriction force. They correspond to the three terms[9] in the following equation [16]:

$$\mathbf{F^e} = q_v\mathbf{E} - \frac{1}{2}\mathbf{E}\cdot\mathbf{E}\nabla\epsilon + \nabla\left[\rho\left(\frac{\partial\epsilon}{\partial\rho}\right)_T \mathbf{E}\cdot\mathbf{E}\right] \tag{1.18}$$

The latter suggests that, generally, there is a mismatch of the value of the electric force across the interface.

Equation (1.13) becomes then:

$$-\nabla p + \mu\nabla^2\mathbf{u} + q_v\mathbf{E} - \frac{1}{2}\mathbf{E}\cdot\mathbf{E}\nabla\epsilon + \nabla\left[\rho\left(\frac{\partial\epsilon}{\partial\rho}\right)_T \mathbf{E}\cdot\mathbf{E}\right] = 0$$

which is rather complex do deal with. However, one may note that if the fluids under study are characterized by constant electric properties, both the electro- and dielectrophoretic contributions in (1.18) go to zero in the fluid bulk:

[8]For example, such processes can stem from viscous relaxation, diffusion, oscillation of an imposed field, or moving of a boundary.

[9]The Coulomb term is due to the action of the electric field $\mathbf{E}$ on the free charges in the fluid bulk q_v, the dielectrophoretic force accounts either for the fact that either the electric permittivity or the electric field may be nonuniform and the electrostriction expression depends on the variation of the electric permittivity with respect to the fluid density, ρ.

$$-\nabla p + \mu\nabla^2\mathbf{u} + \nabla\left[\rho\left(\frac{\partial\epsilon}{\partial\rho}\right)_T \mathbf{E}\cdot\mathbf{E}\right] = 0$$

which, in the case of incompressible flows, can be further rewritten by incorporating the electrostriction term[10] inside a "modified pressure", $P := p - \rho\left(\frac{\partial\epsilon}{\partial\rho}\right)_T \mathbf{E}\cdot\mathbf{E}$ yielding thus:

$$-\nabla P + \mu\nabla^2\mathbf{u} = 0. \tag{1.19}$$

As far as the electric field laws, one has to start from Maxwell's equations: the electric and magnetic field are coupled together. However, in the absence of an external magnetic field, and for very small dynamic electrical currents, it is possible to ignore the degree of magnetic induction and to decouple the electric and magnetic field.

$$\nabla\times\mathbf{E} = 0 \tag{1.20}$$

$$\nabla\cdot(\sigma\mathbf{E}) = 0 \tag{1.21}$$

and

$$\nabla\cdot(\epsilon\mathbf{E}) = q_v. \tag{1.22}$$

Equation (1.20) is also known as the fact that the electric field is irrotational, since $\frac{\partial\mathbf{B}}{\partial t}+\nabla\times\mathbf{E} = 0$ but with $\mathbf{B} = 0$. (1.21) can be obtained by the conservation of electric charge $\frac{D}{Dt}(q_v)+\nabla\cdot\mathbf{J} = 0$ where $\frac{D}{Dt}$ indicates the material derivative and $\mathbf{J}$ is the free electric current density[11]. Moreover, $q_v = 0$ for both fluids, since for leaky-dielectric fluids the electric free charge migrates instantaneously to the interface. Finally, equation (1.22) is Gauss's law relating the electric displacement $\mathbf{D} = \epsilon\mathbf{E}$ to the free charge. Equations [(1.20)-(1.22)] need to be consider together with jump conditions established *ad hoc* at the interface of the drop.

From (1.20), it is possible to define the following:

$$\mathbf{E} = -\nabla V. \tag{1.23}$$

Substitution of (1.21) inside (1.20) results in $\nabla^2 V = 0$ since, as noted before, the fluid has constant electric properties. Equation (1.23) must be solved for the electric field with specific boundary and jump conditions inside and outside the droplet. To conclude, we note that the electric field laws are decoupled from the momentum equation: this means that the expression of $\mathbf{E}$ can be determined without needing the momentum equation. The latter is instead coupled to the electric field equations in the fluid bulk and at the interface.

1.4.4 The electric free charge at the interface

When a fluid is exposed to an external electric field, it is polarized. In the case of perfect conductors, the polarization leads to formation of free charges in the bulk of the fluids and since the electric field in a perfect conductor should be zero according to Ohm's law, the free charges will immediately migrate to the fluid boundary.
Perfect dielectrics, on the other hand, do not have free electrons in their outermost atomic

[10] According to Stratton [16], this term is simpler for non-polar fluids, since it can be written by means of the Clausius-Mossotti factor: $\rho\left(\frac{\partial\epsilon}{\partial\rho}\right)_T = \frac{(\epsilon-\epsilon_0)(\epsilon+2\epsilon_0)}{3\epsilon_0}$.

[11] $\mathbf{J}$ is connected to $\mathbf{E}$ by the Ohm's law, $\mathbf{J} = \sigma\mathbf{E}$.

shells. For these fluids, the polarization leads to dipole moments which align themselves in the direction of the electric field. The surface charge per unit length q_s (area in three dimensions) can be calculated by integration of (1.22) over a two-dimensional pillbox spanning a portion of the boundary and application of Gauss theorem [16]:

$$\int_A \nabla \cdot (\epsilon \mathbf{E}) = \int_A q_v dA. \tag{1.24}$$

This results in $q_s = \epsilon_0 E_{n_0} - \epsilon_i E_{n_i}$, where $q_s = \lim_{A\to 0} \int_A q_v dA$ and $\mathbf{n}$ is the outward unit vector normal to the interface. Since $\sigma_0 E_{n_0} - \sigma_i E_{n_i}$ at the interface, one can rearrange the result into the following:

$$q_s = \epsilon_0 E_{n_0} \left(1 - \frac{S}{R}\right) \tag{1.25}$$

1.4.5 The electrohydrodynamic stresses

To derive the momentum jump condition needed in solving the momentum equation, it is necessary to find the stresses associated with the electric force. This is done by treating the electric force as divergence of the electric stress tensor: $\mathbf{F^e} = \nabla \cdot \tau^e$, where τ^e is the Maxwell stress tensor. If one applies, respectively, equations (1.18), (1.20) and (1.22) obtains:

$$\tau^{\mathbf{e}} = \epsilon \mathbf{E}\mathbf{E} - \frac{1}{2}\mathbf{E}\cdot\mathbf{E}\epsilon\mathbf{I} + \frac{1}{2}\rho\left(\frac{\partial \epsilon}{\partial \rho}\right)_T \mathbf{E}\cdot\mathbf{E}\mathbf{I} \tag{1.26}$$

where $\mathbf{I}$ is the identity tensor. Using instead (1.19), the Maxwell stress tensor has a simple formula:

$$\tau^{\mathbf{e}} = \epsilon \mathbf{E}\mathbf{E} - \frac{1}{2}\mathbf{E}\cdot\mathbf{E}\epsilon\mathbf{I}. \tag{1.27}$$

The key parameters that affect the sense of deformation and fluid circulation are the net normal and tangential electric traction forces at the interface:

$$[[f^e_{sn}]] = f^e_{sn_0} - f^e_{sn_i} \tag{1.28}$$

and

$$[[f^e_{st}]] = f^e_{st_0} - f^e_{st_i} \tag{1.29}$$

where f_{sn} and f_{st} are, respectively, the normal and tangential components of the electric force at the interface. The traction force s $\mathbf{f^e}$ at a general surface are related to the surface stresses τ^e_s through $\mathbf{f^e} = \tau^e_s \cdot \mathbf{n}$.

In a $t-n$ coordinate system one has that $f^e_{sn} = \tau^e_{nn}$ and $f^e_{st} = \tau^e_{tt}$ and therefore:

$$[[f^e_{sn}]] = [[\tau^e_{nn}]]$$

and

$$[[f^e_{st}]] = [[\tau^e_{nt}]].$$

It is easy to demonstrate that:

$$[[\tau^e_{nn}]] = \frac{1}{2}\epsilon_0(E^2_{n_0} - E^2_{t_0}) - \frac{1}{2}\epsilon_i(E^2_{n_i} - E^2_{t_i}) \tag{1.30}$$

$$[[\tau^e_{nt}]] = \epsilon_0 E_{n_0} E_{t_0} - \epsilon_i E_{n_i} E_{t_i} \tag{1.31}$$

that, together with the fact that $E_{t_i} = E_{t_0} \equiv E_t$ and $\sigma_0 E_{n_0} = \sigma_i E_{n_i}$ bring us to:

$$[[f^e_{sn}]] = [[\tau^e_{nn}]] = \frac{\epsilon_0}{2}\left[\left(1 - \frac{S}{R^2}\right)E^2_{n_0} + (S-1)E^2_t\right] \tag{1.32}$$

$$[[f^e_{st}]] = [[\tau^e_{nt}]] = \epsilon_0 E_{n_0} E_t \left(1 - \frac{S}{R}\right) = q_s E_t. \tag{1.33}$$

Some interesting observations can be made from (1.32) and (1.33).

1. For perfect dielectric fluids where $R = S$, the equation (1.32) suggests that the sign of $[[f^e_{sn}]]$ depends on the value of S. For $S > 1$, $[[f^e_{sn}]] > 0$ and the opposite is true for $[[f^e_{sn}]] < 0$. This implies that in both cases the net normal stresses are directed from the fluid of higher electric permittivity toward the one with lower permittivity, in agreement with the experiments.
   On the other hand, for a perfect conductor in a perfect dielectric, where $R \to \infty$, and therefore, $[[f^e_{sn}]] > 0$, again suggesting that the force is from the fluid of higher electric conductivity toward the one with lower conductivity. Under the above circumstances, the interface will always be prolate, whereas, for leaky dielectric fluids, however, the sense of deformation depends on the relative magnitude of R and S [16], [15].

2. Similarly, equation (1.33) suggests that for perfect dielectric fluids where $R = S$, the jump in tangential electric stresses is zero (as there is no free charge according to (1.25). For a perfect conducting fluid in a perfect dielectric liquid where $R \to \infty$, on the other hand, the electric free charge is not zero. However, the jump in tangential stresses is still zero since $E_t = 0$. The net result is that the perfect dielectric/conductor model precludes the fluid flow as it precludes the imbalance in the tangential electrical forces at the interface. For leaky dielectric fluids, the circulation is not zero and depends on the relative magnitude of R and S, [16], [15].

1.4.6 The interface deformation

The analysis so far was based on the assumption that the interface remains circular. However, the interface is likely to deform as a result of the electric and hydrodynamic stresses. For small deformation, it is possible to calculate the distortion from circular shape using normal stress balance at the interface accounting for the restoring force of surface tension:

$$-(P_0 - P_i) + (\tau^e_{rr_0} - \tau^e_{rr_i}) + (\tau^h_{rr_0} - \tau^h_{rr_i}) = \gamma\kappa \tag{1.34}$$

where κ is the local curvature of the interface and γ is the surface tension.

1.5 Possibilities for formulating EHD problems

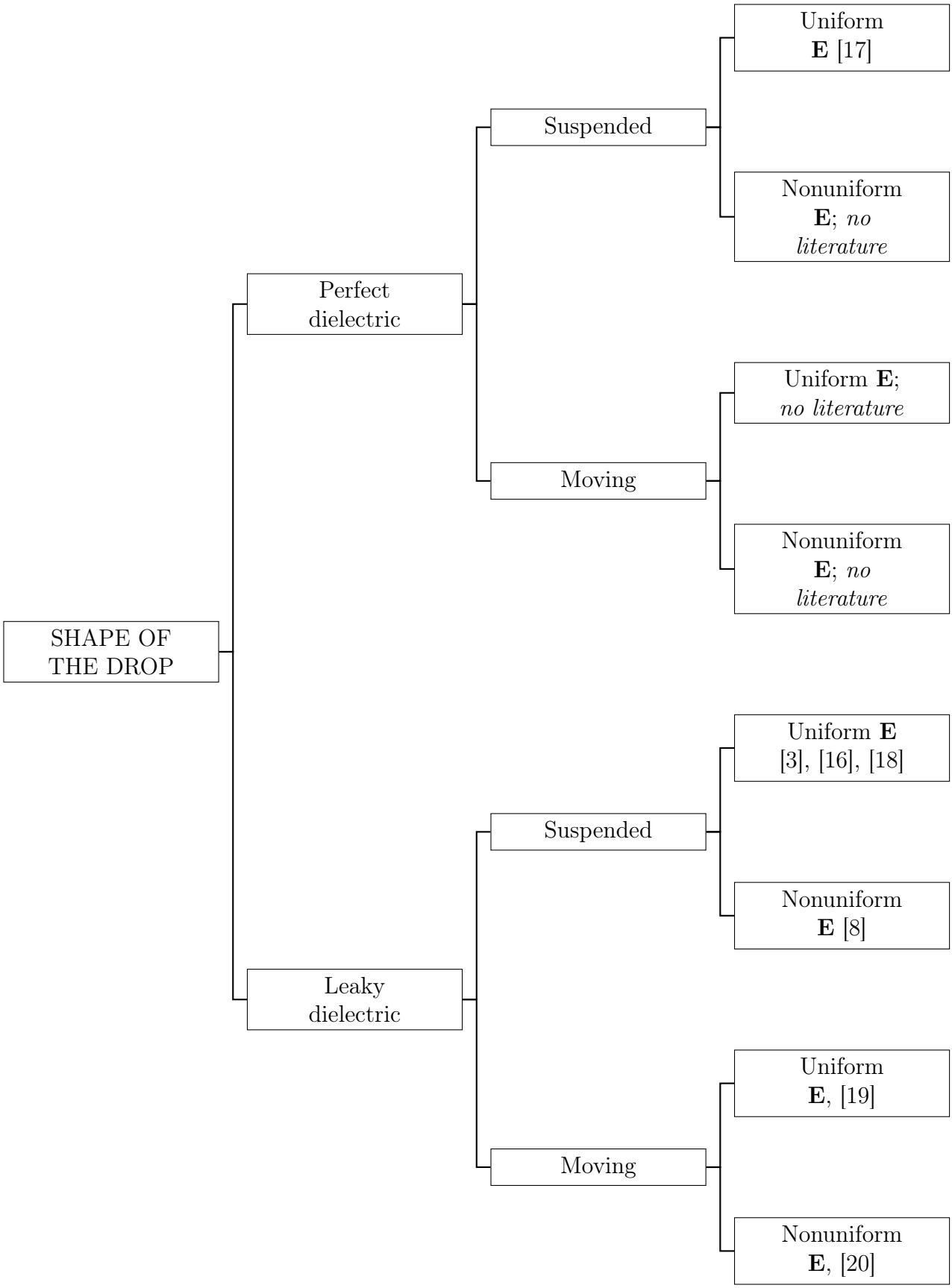

This simple scheme summarizes the various possibilities of formulation of the electrohydrodynamic problem.

Chapter 2

Analytical study of some particular cases

Among all the possible situations referring to the so-called *unbounded* situation[1] we will present some analytically solved cases by appropriately choosing the shape of the drop and by solving the associated EHS/EHD problem.

2.1 Spherical, perfect dielectric drop in uniform E

Let us consider a spherical, neutrally buoyant droplet of fluid immersed and suspended in another fluid of infinite extent and subjected to an electric field. We aim to obtain an analytical expression for the Taylor deformation $\mathcal{D}$ of the drop as a function of time t, that is, $\mathcal{D}(t)$, by using EHS. In the previous chapter we have addresses the importance of the this parameter.

The gradual deformation of the droplet from a sphere to and ellipsoid implies a balance between three forces: the electric stress, the stress due to the interfacial free energy and the hydrodynamic one. We start by analyzing each of those forces separately and then impose the balance equation.
Let us then define the following quantities, which are specific for this case of the sphere:

- r_0, the radius of the spherical drop before the deformation process;
- a and b, respectively, the values of the major and minor semi axes of the final ellipsoid;
- E_∞, the value of the uniform electric field;

2.1.1 Electric stress

First of all, we calculate the electric force acting on the droplet in the absence of space net charges and in the low field limit, as in 1.4.3.
We solve Laplace's equation (1.23) for both the internal and external potential as a function of r; the boundary conditions defined are:

1. $V_i = V_o$ at $r = r_0$;
2. V_i is bounded at $r = 0$;

[1] In which, as already mentioned in 1.4, the outer fluid containing the drop is of infinite extent.

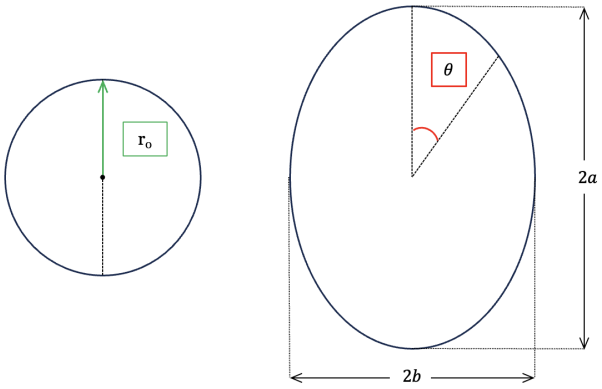

Figure 2.1: A sphere of initial radius r_0 deforming into an ellipsoid.

3. $V_o = -E_\infty \cos\theta$ as $r \to \infty$;

4. $\epsilon_0\epsilon_o \dfrac{\partial V_o}{\partial r} = \epsilon_0\epsilon_i \dfrac{\partial V_i}{\partial r}$ at $r = r_0$.

The solution is then obtained as:

$$V_i(r,\theta) = -3\left(\frac{\epsilon_o}{\epsilon_o + \epsilon_i}\right) E_\infty r\cos\theta \tag{2.1}$$

$$V_o(r,\theta) = \left[\frac{\epsilon_i - \epsilon_o}{(\epsilon_i + 2\epsilon_o)}\left(\frac{r_0}{r}\right)^3 - 1\right] E_\infty r\cos\theta. \tag{2.2}$$

It is straightforward to calculate the radial (apex r) and tangential (apex θ) components of the electric force from the electric field; the latter can in turn be obtained by exploiting equations and using the well-known relation $\mathbf{E} = -\nabla V$.
The complete expressions for the components of field (both inside and outside the drop) are presented below:

$$E^r_{int}(r,\theta) = 3\left(\frac{\epsilon_o}{\epsilon_i + \epsilon_o}\right) E_\infty \cos\theta \tag{2.3}$$

$$E^\theta_{int}(r,\theta) = -3\left(\frac{\epsilon_o}{\epsilon_i + \epsilon_o}\right) E_\infty r\sin\theta \tag{2.4}$$

$$E^r_{ext}(r,\theta) = \left[2\frac{\epsilon_i - \epsilon_o}{(\epsilon_i + 2\epsilon_o)}\left(\frac{r_0}{r}\right)^3 + 1\right] E_\infty \cos\theta \tag{2.5}$$

$$E^\theta_{ext}(r,\theta) = \left[\frac{\epsilon_i - \epsilon_o}{(\epsilon_i + 2\epsilon_o)}\frac{r_0^3}{r^2} - r\right] E_\infty \cos\theta \tag{2.6}$$

from which we obtain the two components of the electric force:

$$F^r_{el} = \frac{9}{2}\epsilon_0 \frac{\epsilon_o(\epsilon_i - \epsilon_i)\left[\epsilon_o + (\epsilon_i - \epsilon_i)\cos^2\theta\right]}{(\epsilon_i + 2\epsilon_o)^2} E^2_\infty \tag{2.7}$$

$$F^\theta_{el} = 0 \tag{2.8}$$

2.1.2 Interfacial stress

By writing F_γ we denote the interfacial stress, meaning the stress across the curved interface between the droplet and the medium due to the interfacial free energy.
In this case, we can derive it from the law of Laplace and Young[2] for the variation of the pressure by considering an unitary area:

$$F_\gamma - \frac{2\gamma}{r_0} = \gamma \left(\frac{1}{R_1} + \frac{1}{R_2} \right) \tag{2.9}$$

with $R_{1,2}$ we indicate the principal radii of the curvature at a generic point (r, θ) of the ellipsoidal drop. For our purposes, it is more useful to rewrite the geometrical factor $\left(\frac{1}{R_1} + \frac{1}{R_2} \right)$ in terms of the deformation $\mathcal{D}$ [21]:

$$\left(\frac{1}{R_1} + \frac{1}{R_2} \right) = \frac{-2 + 4\mathcal{D}(1 + \cos^2\theta)}{r_0(1 - 2\mathcal{D}/3)(1 - 4\mathcal{D}\cos^2\theta)^{3/2}} \tag{2.10}$$

so that by substitution:

$$F_\gamma = \frac{2\gamma}{r_0} + \gamma \left[\frac{-2 + 4\mathcal{D}(1 + \cos^2\theta)}{r_0(1 - 2\mathcal{D}/3)(1 - 4\mathcal{D}\cos^2\theta)^{3/2}} \right] \tag{2.11}$$

2.1.3 Hydrodynamic stress

In this section, we treat the viscous drags on the surface of a deforming droplet due to the velocity fields inside and outside it.
The radial component of the hydrodynamic stress is given by the following formula [17]:

$$\sigma_{rr} = 2\eta \left[(\nabla u)_{rr} - (\nabla u)_{\theta\theta} \right] \tag{2.12}$$

which holds both for the internal and external medium, respectively.

The case under study is characterized by axisymmetric flow, the analytical expression of the radial and tangential velocities can be determined by Stokes's streamfunction method as:

$$u^r(r, \theta, \Psi) = \frac{1}{r^2 \sin\theta} \frac{\partial \Psi}{\partial \theta} \tag{2.13}$$

$$u^\theta(r, \theta, \Psi) = -\frac{1}{r \sin\theta} \frac{\partial \Psi}{\partial \theta} \tag{2.14}$$

with specific boundary conditions [17]:

1. $u_o = 0$ as $r \to \infty$;
2. $u_i^r = u_o^r$ at $r = r_0$;
3. $u_i^\theta = u_o^\theta$ at $r = r_0$.

The simplest case is found by choosing to approximate the **internal** flow (u_i^r, u_i^θ) of a deforming droplet by a simple elongation [17]. This results specifically in the following form :

$$u_i^r(r, \theta, \lambda) = \frac{r}{2}(3\cos^2\theta - 1)\frac{d\lambda}{dt} \tag{2.15}$$

[2] Also known as the *capillary equation*, see section 1.2.

$$u_i^\theta(r,\theta,\lambda) = -\frac{3r}{2}(\sin\theta\cos\theta)\frac{d\lambda}{dt} \tag{2.16}$$

where λ is the elongation ratio. The latter is defined in terms of a and r_0:

$$\lambda(t) = \frac{a(t)}{2r_0} \tag{2.17}$$

but can also be expressed in terms of the deformation [17]:

$$\frac{d\lambda}{dt} = \frac{4}{3}\frac{d\mathcal{D}}{dt} \tag{2.18}$$

so that:

$$u_i^r(r,\theta,\lambda) = \frac{2r}{3}(3\cos^2\theta - 1)\frac{d\mathcal{D}}{dt} \tag{2.19}$$

$$u_i^\theta(r,\theta,\lambda) = -2r(\sin\theta\cos\theta)\frac{d\mathcal{D}}{dt}. \tag{2.20}$$

Equations (2.15) and (2.16) provide the form for the stream function Ψ:

$$\Psi = \sin^2\theta\cos\theta\left[\alpha_1\frac{r_0^4}{r^2} + \alpha_2 r_0^2 + \alpha_3\frac{r^3}{r_0} + \alpha_4\frac{r^5}{r_0^3}\right] \tag{2.21}$$

with $\alpha_{1,2,3,4}$ are coefficients. The latter is used to get the **external** velocity field together with boundary conditions:

$$u_o^r(r,\theta,\lambda) = \frac{(3\cos^2\theta - 1)}{4}\left(\frac{5r_0^3}{r^2} - \frac{3r_0^5}{r^4}\right)\frac{d\lambda}{dt} \tag{2.22}$$

$$u_o^\theta(r,\theta,\lambda) = -\frac{3}{2}\frac{r_0^5}{r^4}(\sin\theta\cos\theta)\frac{d\lambda}{dt} \tag{2.23}$$

that we express again by means of $\mathcal{D}$:

$$u_o^r(r,\theta,\lambda) = \frac{(3\cos^2\theta - 1)}{3}\left(\frac{5r_0^3}{r^2} - \frac{3r_0^5}{r^4}\right)\frac{d\mathcal{D}}{dt} \tag{2.24}$$

$$u_o^\theta(r,\theta,\lambda) = -2\left(\frac{r_0^5}{r^4}\right)(\sin\theta\cos\theta)\frac{d\mathcal{D}}{dt}. \tag{2.25}$$

Finally, equations (2.13) and (2.14) combined with boundary conditions (1-3) result in the expression for the hydrodynamic stresses, respectively inside and outside the drop:

$$\sigma_{int,rr} = \mu_i(8\cos^2\theta - 4)\frac{d\mathcal{D}}{dt} \tag{2.26}$$

$$\sigma_{ext,rr} = \mu_o(8\cos^2\theta - 4)\frac{d\mathcal{D}}{dt} \tag{2.27}$$

2.1.4 Balance equation and deformation rate

The balance equation can be written as:

$$F_{el}^r + F_\gamma = \sigma_{int,rr} + \sigma_{int,rr} + F_0 \tag{2.28}$$

where F_0 is the hydrostatic force deriving from the hydrostatic pressure inside the drop. We aim at deriving an equation in $\mathcal{D}$, which we expect to come out after proper substitution of the expression of the forces, namely equations (2.7), (2.11), (2.26) and (2.27).

2.1.5 Complete expression

A direct substitution would lead to a rather complicated equation in terms of $\mathcal{D}$. In fact, the left member would be the sum of the electric stress and the interfacial one:

$$\frac{9}{2}\epsilon_0\frac{\epsilon_o(\epsilon_i-\epsilon_i)\left[\epsilon_o+(\epsilon_i-\epsilon_i)\cos^2\theta\right]}{(\epsilon_i+2\epsilon_o)^2}E_\infty^2+\frac{2\gamma}{r_0}+\gamma\left[\frac{-2+4\mathcal{D}(1+\cos^2\theta)}{r_0(1-2\mathcal{D}/3)(1-4\mathcal{D}\cos^2\theta)^{3/2}}\right]. \tag{2.29}$$

from which it is not possible to go on.

2.1.6 Simplified expression

However, one can notice that the latter can be simplified if two conditions are verified: the **first** is $\epsilon_i \gg \epsilon_o$ and reduces the electric force to:

$$F_{el}^r=\frac{9}{2}\epsilon_0\epsilon_o E_\infty^2\cos^2\theta. \tag{2.30}$$

The **second** is $\mathcal{D}\ll 1$, used in this case for the interfacial stress: it permits to *taylor-expand*[3] and let us all terms of the form $\mathcal{D}^n$, with $n>1$.

To rearrange the expression:

$$\left[\frac{-2+4\mathcal{D}(1+\cos^2\theta)}{r_0(1-2\mathcal{D}/3)(1-4\mathcal{D}\cos^2\theta)^{3/2}}\right]=\left(\frac{-2+4\mathcal{D}(1+\cos^2\theta)}{r_0}\right)\left(\frac{1}{(1-2\mathcal{D}/3)(1-4\mathcal{D}\cos^2\theta)^{3/2}}\right)$$

we can start from the second term, applying the following steps to its denominator:

* $(1-4\mathcal{D}\cos^2\theta)^{3/2}\sim 1+\frac{3}{2}(-4\mathcal{D}\cos^2\theta)=1-6\mathcal{D}\cos^2\theta$

* $(1-2\mathcal{D}/3)(1-4\mathcal{D}\cos^2\theta)^{3/2}\sim(1-2\mathcal{D}/3)(1-6\mathcal{D}\cos^2\theta)\sim 1-\left(\frac{2\mathcal{D}}{3}+6\mathcal{D}\cos^2\theta\right)$.

Defining $x:=\left(\frac{2\mathcal{D}}{3}+6\mathcal{D}\cos^2\theta\right)$, then:

$$\frac{1}{(1-2\mathcal{D}/3)(1-4\mathcal{D}\cos^2\theta)^{3/2}}\sim(1-x)^{-1}$$

and we can *Taylor expand*: $(1-x)^{-1}\sim(1+x)=1+\frac{2\mathcal{D}}{3}+6\mathcal{D}\cos^2\theta$. The latter is well defined since if $\mathcal{D}\ll 1$, then $x\ll 1$.

Finally:

$$\frac{-2+4\mathcal{D}(1+\cos^2\theta)}{r_0}\left(1+\frac{2\mathcal{D}}{3}+6\mathcal{D}\cos^2\theta\right)\sim\frac{1}{r_0}\left(-2+\frac{8\mathcal{D}}{3}-8\mathcal{D}\cos^2\theta\right).$$

Consequently, F_γ results in a simpler expression:

$$F_\gamma=\frac{2\gamma}{r_0}+\gamma\left[\frac{1}{r_0}\left(-2+\frac{8\mathcal{D}}{3}-8\mathcal{D}\cos^2\theta\right)\right]=\frac{\gamma}{r_0}\frac{8\mathcal{D}}{3}(1-3\cos^2\theta) \tag{2.31}$$

[3]We use the weel-known expansion for $(1\pm x)^\alpha=1\mp x$; in our case it is sufficient to stop at the first order in x.

Therefore, it is possible to obtain the desired equation for $\mathcal{D}$ starting from the balance one:

$$\frac{9}{2}\epsilon_0\epsilon_o E_\infty^2 \cos^2\theta + \frac{\gamma}{r_0}\frac{8\mathcal{D}}{3}(1-3\cos^2\theta) = (\mu_i+\mu_o)(8\cos^2\theta-4)\frac{d\mathcal{D}}{dt} + F_0 \tag{2.32}$$

which can be rearranged as:

$$\cos^2\theta\left[\frac{9}{2}\epsilon_0\epsilon_o E_\infty^2 + \frac{\gamma}{r_0}8\mathcal{D}\right] + \frac{\gamma}{r_0}\frac{8\mathcal{D}}{3} = \cos^2\theta\left[8(\mu_i+\mu_o)\frac{d\mathcal{D}}{dt}\right] - 4(\mu_i+\mu_o)\frac{d\mathcal{D}}{dt} + F_0$$

since the latter should hold for any point of the surface of the drop, we have to impose that:

$$\frac{\gamma}{r_0}\frac{8\mathcal{D}}{3} = -4(\mu_i+\mu_o)\frac{d\mathcal{D}}{dt} + F_0 \tag{2.33}$$

so that $\theta-$*independent* terms fade out and:

$$\frac{9}{2}\epsilon_0\epsilon_o E_\infty^2 + \frac{\gamma}{r_0}8\mathcal{D} = 8(\mu_i+\mu_o)\frac{d\mathcal{D}}{dt}. \tag{2.34}$$

This is a first-order differential equation that can be solved by separation of variables:

$$\mathcal{D}(t) = \mathcal{D}_\infty(1-e^{-t/\tau}) \tag{2.35}$$

where

$$\mathcal{D}_\infty = \frac{9}{16}\frac{\epsilon_o\epsilon_o}{\gamma}r_0 E_\infty \tag{2.36}$$

and

$$\tau = (\mu_i+\mu_o)\frac{r_0}{\gamma} \tag{2.37}$$

2.2 Spherical, leaky dielectric drop in uniform E

As suggested by Taylor [3], spherical coordinates are adopted (r,θ,ϕ) in the simplest case, that is, an axisymmetric system, for which $\partial/\partial\phi = 0$. The droplet is also in this case suspended.

First, the flow of fluids can be considered and the equation (1.14) is solved [3]. The general solution for ψ has to look like $\psi = r^n\sin^2\theta\cos\theta$, whereas the ones for the internal and external streamfunction have the following form:

$$\psi_i = (C_T r_0^{-1} r^3 + D_T r_0^{-3} r^5)\sin\theta^2\cos\theta \tag{2.38}$$

$$\psi_o = (A_T r_0^4 r^{-2} + B_T r_0^2)\sin\theta^2\cos\theta \tag{2.39}$$

which, by means of appropriate boundary conditions [3], yields:

$$A_T = -B_T = C_T = -D_T \tag{2.40}$$

$$A_T = \frac{9r_0\epsilon_0 E_\infty^2}{\mu_o(1+\eta)}\frac{S-R}{10(2+R)^2}. \tag{2.41}$$

Details regarding velocities can be found both in [3] and [16] but are not reported here since they are not relevant.

Viscous stresses at the interface lead to the expression of jumps in hydrodynamic stresses, $[[\sigma^h_{rr}]]$ and $[[\tau^h_{r\theta}]]$:

$$\tau^h_{r\theta} = \frac{9E^2_\infty \epsilon_o}{2(R+2)^2}(R-S)\sin 2\theta \tag{2.42}$$

$$\sigma^h_{rr} = -\frac{9E^2_\infty \epsilon_o}{10(R+2)^2}(R-S)\frac{2+3\eta}{1+\eta}(1-3\cos\theta^2). \tag{2.43}$$

As we have seen in section 1.4, for the electric components one starts by solving Laplace's equation, (1.23), and consequently derives the expression for the electric field and the consequent stresses. The Laplacian operator is expressed in spherical coordinates imposing that $\partial/\partial\phi = 0$, resulting then in the following:

$$\left[\frac{1}{r^2}\left[\frac{\partial}{\partial r}\left(r^2\frac{\partial}{\partial r}\right)\right] + \frac{1}{r^2\sin^2\theta}\left[\frac{\partial}{\partial\theta}\left(\sin\theta\frac{\partial}{\partial\theta}\right)\right]\right]\Phi = 0 \tag{2.44}$$

which is solved according to the boundary conditions expressed in 1.4. This results in:

$$\Phi_i = \frac{3E_\infty}{2+R} r\cos\theta \tag{2.45}$$

$$\Phi_o = E_\infty r\cos\theta + \frac{1-R}{1+R}E_\infty\left(\frac{r^3_0}{r^2}\right)\cos\theta \tag{2.46}$$

$$\mathbf{E}_i = -\frac{3E_\infty}{2+R}\cos\theta\mathbf{e_r} + \frac{3E_\infty}{2+R}\sin\theta\mathbf{e}_\theta \tag{2.47}$$

$$\mathbf{E}_o = \left(-E_\infty\left[1+\frac{2(R-1)}{R+2}\frac{r^3_0}{r^3}\right]\cos\theta\right)\mathbf{e_r} + \left(E_\infty\left[1-\frac{R-1}{R+2}\frac{r^3_0}{r^3}\right]\sin\theta\right)\mathbf{e}_\theta. \tag{2.48}$$

The free charge per unit area at the interface 1.4 can be calculated:

$$q_s = \frac{3E_\infty\epsilon_0(S-R)}{2+R}\cos\theta. \tag{2.49}$$

The electric stresses can also be obtained, resulting in four expressions:

$$\tau^e_{rr_o} = \frac{\epsilon_o E^2_\infty}{2}\left\{-\left[1+\frac{(R-1)^2}{(r+2)^2}\frac{r^6_0}{r^6}-\frac{2(R-1)}{R+2}\frac{r^3_0}{r^3}\right]+[2+\frac{5(R-1)^2}{(r+2)^2}\frac{r^6_0}{r^6}+\frac{2(R-1)}{R+2}\frac{r^3_0}{r^3}]\cos\theta^2\right\} \tag{2.50}$$

$$\tau^e_{r\theta_o} = -\frac{\epsilon_o E^2_\infty}{2}\left[1+\frac{(R-1)^2}{(r+2)^2}\frac{r^6_0}{r^6}-\frac{2(R-1)}{R+2}\frac{r^3_0}{r^3}\right] \tag{2.51}$$

$$\tau^e_{rr_i} = \frac{9E^2_\infty\epsilon_i}{2(R+2)^2}\cos 2\theta \tag{2.52}$$

$$\tau^e_{r\theta_i} = -\frac{9E^2_\infty\epsilon_i}{2(R+2)^2}\sin 2\theta \tag{2.53}$$

note that the latter is actually (2.98) with opposite sign.

Equations (2.50), (2.51), (2.52) and (2.53) are used to find jumps in the traction forces at the interface:

$$[[f_{sn}^e]] = [[\tau_{rr}^e]] = \frac{9E_\infty^2\epsilon_o}{2(R+2)^2}[S-1+(R^2+1-2S)\cos^2\theta] \tag{2.54}$$

$$[[f_{st}^e]] = [[\tau_{r\theta}^e]] = \frac{9E_\infty^2\epsilon_o}{2(R+2)^2}(S-R)\sin 2\theta. \tag{2.55}$$

The balance equation, that is equation (1.34), together with $r = r_0[1+(2\mathcal{D}_T/3)(3\cos\theta^2-1)]$ [3] leads to the equation for the steady state deformation of the interface of the drop:

$$\mathcal{D}_T = \frac{9Ca_{el}}{16}\frac{\Phi_T}{(2+R)^2}, \tag{2.56}$$

$$\Phi_T = R^2+1-2S+\frac{3}{5}(R-S)\frac{2+3\eta}{1+\eta} \tag{2.57}$$

that is the generalization of what we obtained in (2.36).

2.3 Spherical, leaky dielectric drop in nonuniform E

It is possible to generalize the result in the case of a nonuniform electric field as proposed by Feng [8], obtaining[4]:

$$V_i(r,\theta) = -E_\infty\left[\frac{3}{2+R}r\cos\theta+\Lambda\frac{5}{3+2R}r^2P_2(\cos\theta)\right] \tag{2.58}$$

$$V_o(r,\theta) = -E_\infty\left[\left(r+\frac{1-R}{2+R}\frac{r_0^3}{r^2}\right)\cos\theta+\Lambda\left(r^2+2\frac{1-R}{3+2R}\frac{r_0^5}{r^3}\right)P_2(\cos\theta)\right] \tag{2.59}$$

$$q_s = \epsilon_0(\epsilon_o R-\epsilon_i)E_\infty\left[\frac{3}{2+R}r\cos\theta+2\Lambda r_0\frac{5}{3+2R}r^2P_2(\cos\theta)\right] \tag{2.60}$$

$$\psi_i(r,\theta) = \frac{(\epsilon_o R-\epsilon_i)\epsilon_0E_\infty^2}{\mu_i+\mu_o}\sum_{l=2}^{5}\beta_l\frac{r^{l+2}-r_0^2r^l}{r_0^{l-1}}G_l(\cos\theta) \tag{2.61}$$

$$\psi_o(r,\theta) = \frac{(\epsilon_o R-\epsilon_i)\epsilon_0E_\infty^2}{\mu_i+\mu_o}\sum_{l=2}^{5}\beta_l\left(\frac{1}{r^{l-3}}-\frac{r_0^2}{r^{l-1}}\right)G_l(\cos\theta) \tag{2.62}$$

with $r = r_0[1+F(\theta)]$

$$F(\theta) = \sum_{l=2}^{4}\alpha_lP_l(\cos\theta). \tag{2.63}$$

where from the balance equation (1.34) one can derive coefficients α_2, α_3 and α_4:

$$\begin{aligned}\alpha_2 &= \frac{\epsilon_i\epsilon_0r_0E_\infty^2}{4\gamma}\left[\left(\frac{3}{2+R}\right)^2\frac{(SR^2+S-2)}{3}+\left(\frac{5\Lambda r_0}{3+2R}\right)^2\frac{(4SR^2-3S-1)}{7}\right]\\ &= \frac{\epsilon_i\epsilon_0r_0E_\infty^2}{4\gamma}\left\{\frac{(SR-1)(2\eta+3)}{5(\eta)}\left[\left(\frac{3}{2+R}\right)^2+\frac{6}{7}\left(\frac{5\Lambda r_0}{3+2R}\right)^2\right]\right\}\end{aligned} \tag{2.64}$$

[4]We report here only the main results without detailed derivations, that can anyway be found in [8].

$$\alpha_3 = \frac{\epsilon_i \epsilon_0 r_0 E_\infty^2}{50\gamma} \frac{3}{2+R} \left(\frac{5\Lambda r_0}{3+2R} \right) \left[6(SR^2 + S - 2) + \frac{12(SR-1)(3\eta+4)}{7(\eta+1)} \right] \tag{2.65}$$

$$\alpha_4 = \frac{\epsilon_i \epsilon_0 r_0 E_\infty^2}{105\gamma} \left(\frac{5\Lambda r_0}{3+2R} \right)^2 \left[6(SR^2 + S - 2) + \frac{(SR-1)(4\eta+5)}{\eta+1} \right] \tag{2.66}$$

2.4 Spherical drop moving in uniform and non uniform E

This section is devoted to summarize the results obtained by analytical studies on the effects of both a uniform and a nonuniform electric field on the electrohydrodynamic motion of a suspended spherical drop in the presence of an unbounded Poiseuille flow[5] [19], [20].
Both articles, [19] and [20], rely on a double asymptotic expansion in terms of Re_{el} and Ca_{el} assuming small charge convection and small shape deformation. For an uniform field, the droplet is assumed as a Newtonian, leaky dielectric one whereas in the case of the nonuniform field some cases pertaining to perfect dielectrics are also presented.

2.4.1 Uniform Field

The problem formulation is identical to the one that has been proposed in 1.4, with two main specifications, the expression of the field and the one for the imposed background flow:

$$\mathbf{u}_c = u_c(k_0 + k_1 x + k_2 x^2)\mathbf{e}_z \tag{2.67}$$

where

$$k_0 = \frac{4}{H}\left(1 - \frac{2x_d}{H}\right)$$

$$k_1 = \frac{4}{H}\left(1 - \frac{2x_d}{H}\right)$$

and

$$k_2 = -\frac{4}{H}.$$

In the latter, x_d represents the transverse position of the drop centroid, H is the length in the transverse direction separating the two infinite parallel plates. One can note that (2.70) expresses a pressure-driven flow between two parallel plates that are of infinite extension in y and z planes.

The electric field is chosen as:

$$\mathbf{E}_\infty = E_\infty(E_x \mathbf{e}_x + E_z \mathbf{e}_z) \tag{2.68}$$

imposing $1 = E_x^2 + E_z^2$. Thus, it is possible to modify the its direction by opportunely specifying the components along z and x. Lastly, a spherical coordinate system (r, θ, ϕ) placed in the center of the drop (and therefore moving with it) is employed. For better clarity, a graphical representation of the situation is reported below.

[5] Poiseuille flow is a flow that occurs due to pressure in a long duct, typically a pipe. The assumption is that a constant positive pressure difference causes a laminar flow of an incompressible Newtonian fluid. The term pipe refers to a circular cylindrical duct that is right-handed and has a circular cross section that is normal to its axis or generator [13].

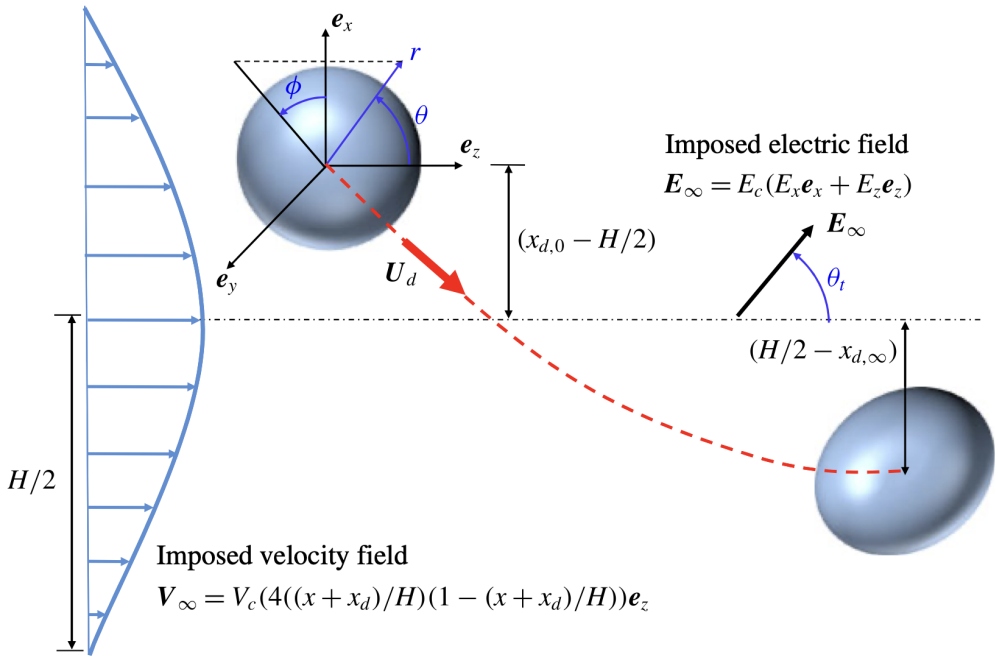

Figure 2.2: Taken from [19].

In the framework of the leaky dielectric model, a double asymptotic expansion choosing the electric Reynolds number and capillary number as parameters is performed. The main result of this expansion is the influence of both charge convection (parameter Re_{el}) and shape deformation (parameter Ca) on $\mathbf{u}_d$, the velocity of the drop, that is unknown *a priori*. The result is:

$$\mathbf{u}_d = (u_d^z)\mathbf{e}_z + (u_d^x)\mathbf{e}_x \tag{2.69}$$

where (u_d^z and u_d^x are functions of expansion parameters. The fact that the result has velocity components in both the axial direction (z) and the cross-stream direction (x) implies a transverse motion, during which the droplet encounters a spatially varying background flow. This latter variation results in a continuous variation of both the internal and external flow field and electric potential. There is thus a constant adjustment of internal and external velocity and surface charge distribution.

The combined effect of charge convention and shape deformation, depending on the magnitude of the controlling parameters, can result in:

1. increase or decrease the drop velocity;

2. lead to cross-stream motion of the drop.

2.4.2 Nonuniform field

In this case, the problem setup is the same as 2.4.1, but with different expression both for the flow and the field:

$$\mathbf{u}_c = u_c \left(1 - \left(\frac{r}{r_0}\right)^2\right) \mathbf{e}_z \tag{2.70}$$

$$\mathbf{E}_\infty = -[E_u r P_1 \cos\theta + E_q r^2 P_2 \cos\theta] \tag{2.71}$$

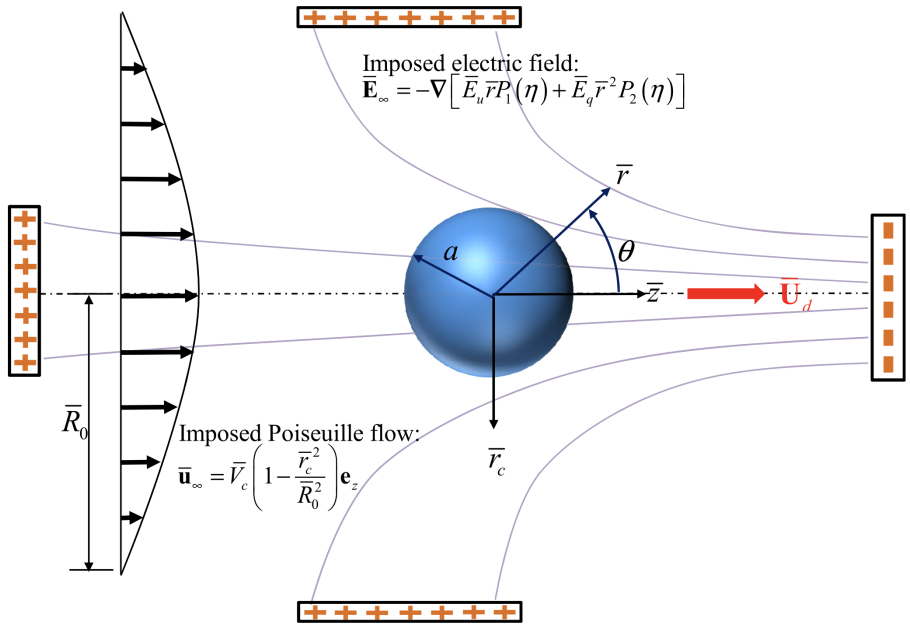

Figure 2.3: Taken from [19]. notice that the field is not necessarily transverse to the motion of the droplet.

where E_u and E_q are he relative strength of the uniform and quadrupole fields: note that (2.71) is nothing but a rewrite of (1.2).

The governing equations are the same as presented before, that is Laplace's equation for the electric field and Stokes and continuity equation for the velocity field with specific boundary conditions (for more details, refer to [20]). The method used for the solution is the same as presented in section 2.4.1 (small-deformation perturbation analysis, asymptotic expansion).

Also in this case the main focus is on determining the unknown drop velocity under the action of both an imposed external flow and a nonuniform electric field.
The latter is achieved by imposing a *force-free* condition, meaning by balancing the hydrodynamic and the dielectrophoretic forces:

$$\mathbf{F}^h + M\mathbf{F}^{el} = 0 \tag{2.72}$$

where M is the Masson number and

$$\mathbf{F}^h = 2\pi \int_{\theta=0}^{\pi} (\tau_o^h \cdot \mathbf{n})[r_s(\theta)]^2 \sin\theta d\theta \tag{2.73}$$

$$\mathbf{F}^{el} = 2\pi \int_{\theta=0}^{\pi} (\tau_o^{el} \cdot \mathbf{n})[r_s(\theta)]^2 \sin\theta d\theta \tag{2.74}$$

are the expression of the forces. $r_s(\theta) = 1 + f(\theta)$ is the radial location of the deformed drop surface [20].

Several cases are analyzed: three for the type of dielectrics and for the type of field.

1. both fluids are perfect dielectrics;
2. the inner fluid is a perfect dielectric and the outer is not;
3. both the inner and the outer fluids are leaky dielectrics.

1. the field has only the linear or only the quadrupolar component;
2. the field has both components;
3. the field is converging or diverging one (respectively, $E_u = E_q = 1$ and $E_u = -E_q = -1$).

The most relevant final result of the work for this thesis is the fact that, in the combined presence of a uniform/quadrupole electric field and Poiseuille flow, a drop always moves in the direction of the Poiseuille flow **irrespective of the value of electrohydrodynamic parameters**.

2.5 Cylindrical, leaky dielectric drop in uniform E

This section regards a drop that is chosen to be a cylinder with circular cross section of radius r_0. This shape is chosen to extend the model to long drops that can not assumed to have a spherical shape.

The cylinder is of infinite length, immersed and suspended in another ambient liquid of infinite extent. It is subjected to an external, uniform, transverse electric field, $\mathbf{E}_\infty$.

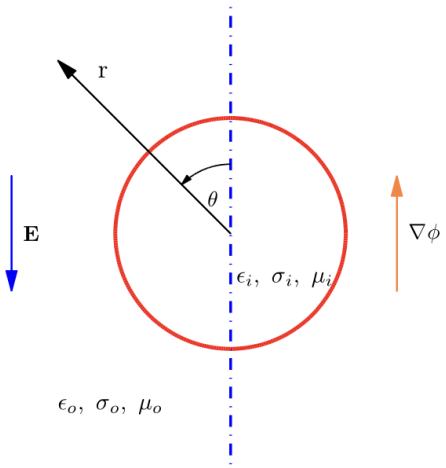

Figure 2.4: Simple scheme showing the circular cross-section of a cylindrical drop [16].

The problem is about to be solved in the framework of the EHD theory, assuming the validity of the leaky dielectric model, both for its steady states and for the transient evolution[6].

2.5.1 Steady states

This part is made up of three main calculations: the solution of Laplace's equation, the solution of the stream function equation and the computations for the deformation of the interface.

Laplace's equation

We adopt cylindrical coordinates (r, θ, z) to solve equation (1.23) by separation of variables. The geometry of the system allows us to assume cylindrical symmetry, that is $\partial/\partial z = 0$. The

[6]That is, we are going to derive the equivalent of equation (2.36) in the case of a different shape.

boundary conditions are:

(i) The electric potential should remain finite inside the cylinder: $V_i(0,\theta)$ has to be bounded;

(ii) The electric potential across the interface should be continuous[7]: $V_i(r_0,\theta) = V_o(r_0,\theta)$;

(iii) The normal component of electric current density should be continuous across the interface[8]: $\sigma_i \dfrac{\partial V_i(r_0,\theta)}{\partial r} = \sigma_o \dfrac{\partial V_o(r_0,\theta)}{\partial r}$

(iv) The electric potential far away from the cylinder[9] behaves as: $V_o(r,\theta) = E_\infty r\cos\theta$.

The obtained solutions are:

$$V_i(r,\theta) = \frac{2E_\infty}{1+R} r\cos\theta \tag{2.75}$$

$$V_o(r,\theta) = E_\infty r\cos\theta - E_\infty \frac{1-R}{1+R}\frac{r_0^2}{r}\cos\theta \tag{2.76}$$

$$\mathbf{E}_i = -\frac{2E_\infty}{1+R}\cos\theta\mathbf{e}_r + \frac{2E_\infty}{1+R}\sin\theta\mathbf{e}_\theta \tag{2.77}$$

$$\mathbf{E}_o = -E_\infty\left[1+\frac{1-R}{1+R}\frac{r_0^2}{r^2}\right]\cos\theta\mathbf{e}_r + -E_\infty\left[1-\frac{1-R}{1+R}\frac{r_0^2}{r^2}\right]\sin\theta\mathbf{e}_\theta. \tag{2.78}$$

For the problem under study, the strength and distribution of the electrical free charges at the interface have profound effect on the sense of deformation of the interface and fluid circulations in the cylinder and in the ambient fluid. The latter results in:

$$q_s = \frac{2E_\infty\epsilon_o(S-R)}{R+1}\cos\theta \tag{2.79}$$

suggesting that the distribution of the free charge on the interface depends on the strength and direction of the electric field and the relative magnitude of R and S. Furthermore, the total free charge is zero.

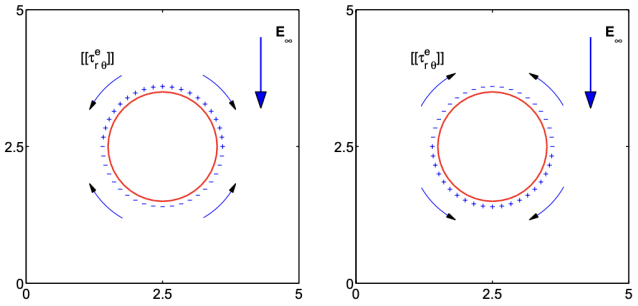

Figure 2.5: This figure shows schematically the distribution of the free charge on the interface for two cases, $R < S$ (the left frame) and $R > S$ (the right frame), along with the directions of the net electrical stresses acting on the interface [16].

For $R < S$, the upper half of the cylinder is induced with positive charges, the same in sign to the electrode that it faces, while the lower half is covered by negative charges. The opposite is true for $R > S$. If the direction of the electric field is reversed, the distribution of the charges will also be reversed. $R = S$ represents a perfect dielectric fluid in a perfect dielectric fluid: as we have already seen, for this type of problem $q_s = 0$.

[7]This can be proved using a two-dimensional pillbox system spanning a portion of the interface and applying Stoke's theorem on eq. (1.20).

[8]This can be proved using again a two-dimensional pillbox system spanning a portion of the interface and applying Gauss' theorem on eq. (1.21).

[9]This boundary condition can be better understood by looking at the figure: far away from the drop, the radial and angular components of the electric field result in $E_r = -E_\infty\cos\theta$ and $E_\theta = E_\infty\sin\theta$.

As for the electric stresses, it is sufficient to substitute equations (2.77) and (2.78) in (1.30) and (1.31) to get:

$$\tau^e_{rr_o} = \frac{1}{2}\epsilon_o E^2_\infty \left[\left(\frac{1-R}{1+R}\right)^2 \left(\frac{r_0}{r}\right)^4 - 1\right] \sin 2\theta \tag{2.80}$$

$$\tau^e_{r\theta_o} = \frac{1}{2}\epsilon_o E^2_\infty \left\{2\left[1+\left(\frac{1-R}{1+R}\right)^2 \left(\frac{r_0}{r}\right)^4\right]\cos\theta^2 - \left[1+\left(\frac{1-R}{1+R}\right)^2 \left(\frac{r_0}{r}\right)^4 - 2\left(\frac{1-R}{1+R}\right)\left(\frac{r_0}{r}\right)^2\right]\right\} \tag{2.81}$$

$$\tau^e_{rr_i} = \frac{2\epsilon_i E^2_\infty}{(R+1)^2}(2\cos\theta^2 - 1) \tag{2.82}$$

$$\tau^e_{r\theta_o} = -\frac{2\epsilon_i E^2_\infty}{(R+1)^2}\sin 2\theta \tag{2.83}$$

Electric stresses, namely equations (2.80)-(2.83), are independent of the electric field polarity; inner stresses do not depend on the radial coordinate. The introduction of the cylinder in the ambient fluid results in a perturbation in the radial and tangential electric stresses that are proportional to $1/r^2$ and $1/r^4$, respectively. To get the stresses associated with the electric field, it is again sufficient to substitute equations (2.77) and (2.78) in (1.32) and (1.33) to get:

$$[[f^e_{sn}]] = [[\tau^e_{nn}]] = \frac{2\epsilon_o E^2_\infty}{(1+R)^2}[S - 1 + (R^2 - 2S + 1)\cos\theta^2] \tag{2.84}$$

$$[[f^e_{st}]] = [[\tau^e_{nt}]] = \frac{2\epsilon_o E^2_\infty}{(1+R)^2}(S - R)\sin 2\theta]. \tag{2.85}$$

Solution of the stream function equation

For the solution of the biharmonic equation (1.14) boundary conditions need to be specified, too. The following ones have been applied:

(i) The velocity field should remain finite inside the cylinder, that is $u_{r_i}(0,\theta)$ and $u_{\theta_i}(0,\theta)$ should be bounded;

(ii) $u_{\theta_o} = u_{\theta_i}$ at $r = r_0$, the *no-slip* boundary condition;

(iii) $u_{r_o}(r_0,\theta) = u_{r_i}(r_0,\theta) = 0$, the *no-through flow* boundary condition;

(iv) at the phase boundary, there has to be no tangential stress, so its balance should be imposed: $(\tau^h_{r\theta_o} - \tau^h_{r\theta_i}) + (\tau^e_{r\theta_o} - \tau^e_{r\theta_i}) = 0$

(v) no velocity field should exist in the far field, $u_{r_o} \to 0$ and $u_{\theta_o} \to 0$ for $r \to \infty$

where (i), (iii) and (v) provide two conditions each, giving the three apparently missing boundary conditions. Both equation (1.14) and the boundary conditions are homogeneous: hence, separation of variables can be used for the solution. The internal and external stream function are found to be:

$$\psi_o = (A + Cr^{-2})\sin 2\theta \tag{2.86}$$

$$\psi_i = (Fr^2 + Hr^4)\sin 2\theta \tag{2.87}$$

where

$$A = r_0^2\epsilon_o E^2_\infty (S - R)/[\mu_o(1+\eta)][2(1+R)]^2, \tag{2.88}$$

and

$$C = -Ar_0^2, \tag{2.89}$$

$$F = -A/r_0^2, \tag{2.90}$$

$$H = A/r_0^4. \tag{2.91}$$

Lastly, one can calculate the jump in the hydrodynamic traction forces across the interfaces are:

$$[[f_{sn}^h]] = [[\tau_{rt}^h]] = \frac{2\epsilon_o E_\infty^2 (R-S)(\eta-1)}{(R+1)^2(\eta+1)} \cos 2\theta \tag{2.92}$$

$$[[f_{st}^h]] = [[\tau_{r\theta}^h]] = \frac{2\epsilon_o E_\infty^2 (R-S)}{(R+1)^2} \sin 2\theta \tag{2.93}$$

The deformation of the interface

The balance equation(1.34) is valid for small deformations and can be used to compute the distortion of the circular cross section, that is likely to deform into an ellipsoid, turning the circular cylinder into an elliptic one.

Let us start from the balance equation:

$$-(P_0 - P_i) + (\tau_{rr_0}^e - \tau_{rr_i}^e) + (\tau_{rr_0}^h - \tau_{rr_i}^h) = \gamma\kappa \tag{2.94}$$

for which we miss the pressure jump across the surface of the drop, $[[P]]$. The latter can be computed simply by specifying the components of equation (1.19):

$$\frac{\partial P}{\partial r} = \mu \left[\frac{\partial}{\partial r} \left(\frac{1}{r} \frac{\partial (r u_r)}{\partial r} \right) + \frac{1}{r^2} \frac{\partial^2 u_r}{\partial \theta^2} - \frac{2}{r^2} \frac{\partial u_\theta}{\partial \theta} \right] \tag{2.95}$$

$$\frac{1}{r} \frac{\partial P}{\partial \theta} = \mu \left[\frac{\partial}{\partial r} \left(\frac{1}{r} \frac{\partial (r u_\theta)}{\partial r} \right) + \frac{1}{r^2} \frac{\partial^2 u_\theta}{\partial \theta^2} - \frac{2}{r^2} \frac{\partial u_r}{\partial \theta} \right] \tag{2.96}$$

note that P is the modified pressure. By combining equations (2.95), (2.96) with the results expressed in the footnote **9** and equations (2.78), (2.77) one can find the pressure jump varying across the interface (retaining only θ-*dependent* terms):

$$[[P]] = \frac{2(3\mu_i - \mu_o)}{r_0} \cos 2\theta \left(\frac{2A}{r_0} \right) \tag{2.97}$$

with A given by equation (2.88).
The latter is grouped with the $(\tau_{rr_0}^h - \tau_{rr_i}^h)$ into σ_{rr}^h, defined as:

$$[[\sigma_{rr}^h]] = [[\tau_{rr}^h]] - [[P]] = \frac{\epsilon_o E_\infty^2 (R-S)}{(R+1)^2} \cos 2\theta. \tag{2.98}$$

The following equation for the evolution of the radius of the cross section[10] is suggested by equations (2.84) and (2.98):

$$\zeta(r) = r_0(1 + \mathcal{D} \cos 2\theta) \tag{2.99}$$

[10]Notice that, since the interface deformation is assumed to be very small, the interfacial jump conditions have been imposed at $r = r_0$ instead of $\zeta(r)$.

that is, a linear variation with respect to $\cos 2\theta$. In a similar way of the calculations presented in 2.1.6, one can also find the curvature:

$$\kappa = \frac{1 + 6\mathcal{D}\cos 2\theta}{[r_0(1 + 2\mathcal{D}\cos 2\theta)^{3/2}]} \sim \frac{1}{r_0}(1 + 3\mathcal{D}\cos 2\theta). \tag{2.100}$$

Substitution and comparison of the θ-terms yields:

$$\mathcal{D} = \frac{Ca_{el}}{3}\frac{\Psi}{(1+R)^2} \tag{2.101}$$

where $\Psi = R^2 + R + 1 - 3S$ is the characteristic function that determines the sense of interface deformation. Notice that, since (1.34) should be valid at any point at the interface, the constant terms on both sides of the equation are balanced and do not influence equation (2.101).

2.5.2 Transient evolution

Whereas the equilibrium dynamic of a drop of liquid surrounded by another fluid in a transversal electrical field is reasonably well understood for spherical and cylindrical droplets, there is little information on the evolution of fluid flow towards the steady state and the deformation time history of a cylinder.

Also in this case the solution of Laplace's equation and the solution of the stream function equation have to be calculated. The first has already been solved in section 2.5.1. As for the second, nine boundary conditions are now needed[18]:

(i) The velocity field should remain finite inside the cylinder, that is $u_{r_i}(0,\theta)$ and $u_{\theta_i}(0,\theta)$ should be bounded;

(ii) $u_{\theta_o} = u_{\theta_i}$ at $r = r_0$, the *no-slip* boundary condition;

(iii) $u_{r_o} = u_{r_i} = d\zeta/dt$ at $r = r_0$, where $\zeta(r) = r_0(1 + \mathcal{D}\cos 2\theta)$;

(iv) at the phase boundary, there has to be no tangential stress, so its balance should be imposed: $(\tau^h_{r\theta_o} - \tau^h_{r\theta_i}) + (\tau^e_{r\theta_o} - \tau^e_{r\theta_i}) = 0$

(v) no velocity field should exist in the far field, $u_{r_o} \to 0$ and $u_{\theta_o} \to 0$ for $r \to \infty$

(vi) $-[[P]] + [[\tau^h_{rr}]] + [[\tau^h_{rr}]] = \gamma\kappa$, the balance equation.

where (i), (iii) and (v) provide two conditions each, giving the three apparently missing boundary conditions. Following the same steps that have been presented in sections 2.5 and 2.1 and using boundary conditions one obtains:

$$\mathcal{D}(t) = \mathcal{D}_\infty(1 - e^{-t/\tau}) \tag{2.102}$$

where

$$\mathcal{D}_\infty = \frac{Ca_{el}}{3}\frac{\Psi}{(1+R)^2} \tag{2.103}$$

and

$$\tau = (\mu_i + \mu_o)\frac{r_0}{\gamma} \tag{2.104}$$

that are consistent with the findings of the previous section.

2.6 Ellipsoidal jet

Actually, in order to model the shape of the drop, an ellipsoidal form for the cross section of the drop has also been proposed [22], [23].

According to Vlahovska [22], if the shape of the drop is chosen to be an axisymmetric ellipsoid parameterized by:

$$r_s = r_0(1 + s(t)P_2(\cos\theta)) \tag{2.105}$$

where the temporal evolution of the s parameter is connected to the one of Taylor's deformation, $\mathcal{D}_T$ through[11]:

$$\mathcal{D} = \frac{3}{4}s. \tag{2.106}$$

Since $s(t)$ evolves as:

$$\frac{\partial s}{\partial t} = \frac{40(1+\eta)}{(3+2\eta)(16+9\eta)}\left[\frac{3}{4}F(R,S,\eta,t) - \frac{s(t)}{Ca}\right] \tag{2.107}$$

where

$$F(R,S,\eta,t) = \frac{(16+19\eta)}{45(1+\eta)}\left(1 - S - (1+2S)\mathcal{P} + \left(\frac{13+7\eta}{(16+19\eta)} - S\right)\mathcal{P}^2\right) \tag{2.108}$$

with $\mathcal{P}$ being a function of time:

$$\mathcal{P}(t) = \frac{1-R}{2+R}(1 - e^{-t}).$$

In the case of instantaneous polarization relaxation[12], the steady state is monotonically approached [22]:

$$\mathcal{D}(t) = \mathcal{D}_\infty(1 - e^{-t/\tau}) \tag{2.109}$$

where

$$\mathcal{D}_\infty = \frac{9}{16}CaF^\star(R,S,\eta), \tag{2.110}$$

$$F^\star(R,S,\eta) = \frac{1}{(2+R)^2}\left[R^2 + 1 - 2S + 3(R-S)\frac{2+3\eta}{5(1+\eta)}\right] \tag{2.111}$$

and

$$\tau = \frac{\mu_o r_0}{\gamma}\left(\frac{(3+2\eta)(16+19\eta)}{40(1+\eta)}\right). \tag{2.112}$$

[11] Note that a direct comparison shows that (2.106) is the same as the one we saw for the elongation ratio, (2.18).

[12] On the contrary, if the dipole evolves on a time scale comparable to the flow time scale the approach to steady state may be nonmonotonic [22].

The case of an ellipsoid has been also treated in a different way[23]. The stability of a two-dimensional liquid jet subject to a transverse electric field in the framework of EHS (so, perfect dielectrics) can be analyzed by modeling the jet as an ellipse. The figure below shows the geometric setup depicting the equilibrium shape of the suspended jet, which is surrounded by another dielectric liquid.
The goal is to relate in some way the aspect ratio, $\alpha = a/b$ to the parameters S and Ca_{el}. $\xi = \xi_0$ corresponds to the jet profile.

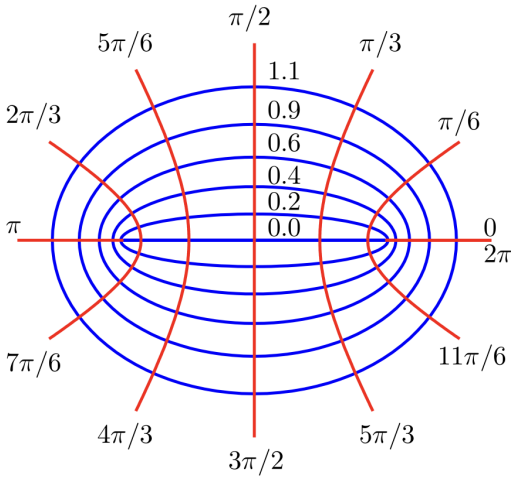

Figure 2.7: Taken from [23].

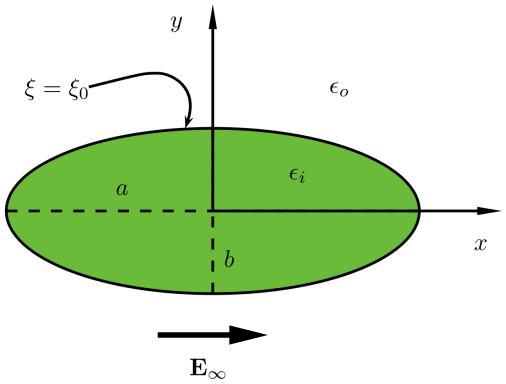

Figure 2.6: Equilibrium shape of the jet [23].

The elliptic coordinate system ξ, ν showed in the next figure to the left is an orthogonal one. It is characterized by the fact that coordinate lines are confocal ellipses and hyperbolae, respectively $\xi = C$, $\nu = C$. Note that $\xi > 0$ and $\nu \in [0, 2\pi]$. The foci of the cross section of the jet are assumed to correspond to the ones of the coordinate lines. Specifically, by referring to figure 2.6 one has:

$$x = c \cosh \xi \cos \nu \tag{2.113}$$

$$y = c \sinh \xi \sin \nu \tag{2.114}$$

where c is the distance from any of the foci to the center.

It is trivial to get the aspect ratio as a function of new coordinates: $\alpha = a/b = \coth \xi_0$. Laplace's equation (1.23) in elliptic coordinates[13] is then solved by imposing appropriate boundary conditions:

(i) the inner electric potential does not depend on ξ at $\xi = 0$, $\dfrac{\partial V_i(0,\nu)}{\partial \xi} = 0$;

(ii) the electric potential across the interface should be continuous: $V_i(\xi_0, \nu) = V_o(\xi_0, \nu)$;

(iii) the normal component of electric current density should be continuous across the interface: $\epsilon_i \dfrac{\partial V_i(\xi_0,\theta)}{\partial r} = \epsilon_o \dfrac{\partial V_o(\xi_0,\nu)}{\partial r}$;

(iv) the electric potential in the far field, $\nu \to \infty$ behaves as: $V_o(\xi, \nu) = -E_\infty x = -E_\infty c \cosh \xi \cos \nu$.

Boundary conditions (i) and (iv) impose that not only $\xi = 0$ is the axis of symmetry, but also that the system is symmetric with respect to ν.
After having found the electric potential and the electric field, the desired relation is found by two different methods:

[13]The Laplacian operator in this current case reads: $\nabla^2 = \partial^2/\partial\xi^2 + \partial^2/\partial\nu^2$

- imposing the balance condition, $[[\tau_{nn}^{el}]] - [[p]] = \kappa\gamma$, at the poles and at the equator. Note that the latter is nothing but equation (1.34) with only normal stresses inside[14].
  This method is referred as *two-point* method [23].
  This leads to the following result:

$$Ca_{el} = \frac{2(\alpha + S)^2(\alpha^3 - 1)}{\alpha^{3/2}(S-1)^2(\alpha+1)^2} \tag{2.115}$$

- After having assumed that the equilibrium shape of the jet under the electric field results as an ellipse, one calculates the difference between total energy of the outer fluid pool without and with the jet. This difference is then minimized with respect to *alpha*. Mathematically speaking, this is equal to:

$$\frac{\partial \Delta U_{tot}}{\partial \alpha} = 0 \tag{2.116}$$

  where $\Delta U_{tot} = \Delta U_{el} + \Delta U_{st}$ is the total difference in energy including the potential electrostatic energy and the surface tension energy [23]. The result is then:

$$Ca_{el} = (\Lambda_1 + \Lambda_2)\left(\frac{S+\alpha}{S-1}\right) \tag{2.117}$$

$$\Lambda_1 = \alpha^{-3/2}(\alpha - 1)\left[1 + \frac{3(\alpha-1)^2}{(\alpha+1)^2(10+\delta)}\right] \tag{2.118}$$

$$\Lambda_1 = \frac{12(\alpha-1)[5 + 20\delta + 5\alpha^2(1+4\delta) + \alpha(22+40\delta)]}{\delta\alpha^{1/2}(\alpha+1)^4(10+\delta)^2} \tag{2.119}$$

$$\delta = \sqrt{\frac{1 + 14\alpha + \alpha^2}{(1+\alpha)^2}}. \tag{2.120}$$

  This result of the energy minimization method is in close agreement with those of (??) and (??), who did not assume the jet profile *a priori* but actually solved for it. Thus, the energy minimization can be considered as a more reliable technique in examining the equilibrium shape of the jet.

Both (2.115) and (2.116) are found to be implicit relations, but the results show evident difference. This depends on a specific error that affects mainly the two-point method for jets. In fact, the two-point method can be then employed for the drops with a great level of accuracy but that is not true for the jets[15].

[14] This is consistent with considerations that have been made in section 1.3.1.

[15] "This is because the error in calculation of the curvature due to approximating the actual shape of a drop as an ellipsoid is smaller than the corresponding error due to approximating a jet" [23]. The curvature of an axisymmetric drop results in the sum of both the azimuthal (curvature of a circle) and the profile curvatures (ellipse): the latter is approximated, but the former is exact.

2.7 Summary

This page summarizes the main results of the problems treated in the chapter.

COMMON PARAMETERS

μ viscosity — γ surface tension — σ electric conductivity — ϵ electric permittivity — E_∞ intensity of the external applied field — r_0 initial characteristic length of the drop (unbounded case)

$$R = \frac{\sigma_i}{\sigma_o} \quad , \quad S = \frac{\epsilon_i}{\epsilon_o} \quad , \quad \eta = \frac{\mu_i}{\mu_o} \quad , \quad Ca = \frac{\epsilon_o E_\infty^2 r_0}{\gamma} \quad \text{and} \quad \mathcal{D}_T = \frac{r_\parallel - r_\perp}{r_\parallel + r_\perp}.$$

Spherical droplet

Initial radius r_0

- Perfect dielectric, suspended, uniform $\mathbf{E}$:

$$\mathcal{D}_T(t) = \mathcal{D}_\infty(1 - e^{-t/\tau_\mathcal{D}}),$$
$$\mathcal{D}_{T,\infty} = \frac{9}{16}\frac{\epsilon_0\epsilon_o}{\gamma} r_0 E_\infty,$$
$$\tau_\mathcal{D} = (\mu_i + \mu_o)\frac{r_0}{\gamma}.$$

- Leaky dielectric, suspended, uniform $\mathbf{E}$:

$$\mathcal{D}_T = \frac{9Ca_{el}}{16}\frac{\Phi_T}{(2+R)^2} \tag{2.121}$$

$$\Phi_T = R^2 + 1 - 2S + \frac{3}{5}(R-S)\frac{2+3\eta}{1+\eta} \tag{2.122}$$

Cylinder, circular cross section

The steady state is approached as:

$$\mathcal{D}(t) = \mathcal{D}_\infty(1 - e^{-t/\tau_\mathcal{D}}).$$

The steady state value deformation is:

$$\mathcal{D}_{T,\infty} = \frac{Ca_{el}}{3}\frac{\Psi}{(1+R)^2},$$

where $\Psi = R^2 + R + 1 - 3S$ and

$$\tau_\mathcal{D} = (\mu_i + \mu_o) r_0/\gamma$$

with $F^\star(R, S, \eta)$ given by equation (2.108).

Ellipsoidal cross section

$$\mathcal{D}(t) = \mathcal{D}_\infty(1 - e^{-t/\tau_\mathcal{D}}).$$

The steady state value deformation is:

$$\mathcal{D}_\infty = \frac{9}{16} Ca_{el} F^\star(R, S, \eta),$$

and

$$\tau_\mathcal{D} = \frac{\mu_o r_0}{\gamma}\left(\frac{(3+2\eta)(16+19\eta)}{40(1+\eta)}\right)$$

Chapter 3

Model implementation from a real case

As we have extensively seen in the theoretical parts, the establishment of an electric field in a region where two immiscible fluids (a drop and an ambient liquid) are separated by an interface, causes discontinuities in some specific physical quantities that are likely to establish a deformation of the droplet.
Experimental evidence of this can be seen by exploiting, for example, an opto-microfluidic platform. In this case, droplets are usually moving due to pressure flow passing through a region where an electric field is imposed. In particular, such platforms permit to investigate electric field effects on liquid droplets in other fluid systems by measuring their lengths in different conditions (that is with and without the field).

However, there is a mismatch between theory and experiments: EHS/EHD models remain simple and limited to some specific assumptions, whereas measured data are a result of the complexity of the real system.
Aiming at extending existing theoretical models (or at least to analyze their strengths, limitations and weaknesses), this chapter compares the results of two of them – actually among those derived in *Chapter 2* – with real data from a specific experiment, that is with measurements of the response of microfluidic water droplets to a time-varying, spatially nonuniform electric field.

Before the comparison, the following aspects are treated in what comes:

1. Lithium niobate (LN), by analyzing its crucial properties, given that the platform is realized on a fully integrated lithium niobate substrate;

2. exposition of the theory on the generation of the electric field, which is a photoinduced one;

3. main theoretical elements for the generation of microdroplets;

4. details on the type of platform that makes it possible to combine points (2) and (3) together;

5. the real configuration, that is, the description of the real field and the actual drop for the system.

3.1 Lithium niobate main properties

At room temperature, Lithium niobate ($LiNbO_3$) is an artificial ferroelectric crystal that appears solid and does not exhibit solubility in water or organic solvents. Zachariasen synthesized it for the first time in 1928 and studied it extensively at Bell laboratories 20 years later [24]. This material belongs to pseudo-binary compound class Li_2O-Nb_2O_5 and bulk growth using the Czochralski technique is the most commonly used method to produce it[1]. Especially in the congruent composition, the solid and liquid phases have the same Li:Nb ratio, allowing controlled and reproducible growth: the ratio between lithium and niobium has a significant impact on the properties of lithium niobate, such as phase transition temperature and UV band absorption edge [26].

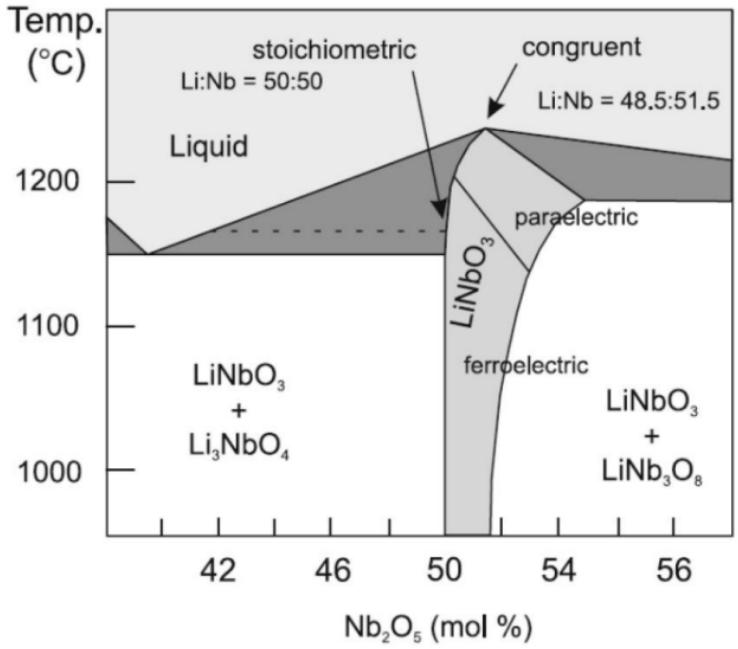

Figure 3.1: Phase diagram of pseudo-binary Li_2O-Nb_2O_5 system [27].

In the ferroelectric phase, for temperatures below $LiNbO_3$ Curie temperature $T_C \approx 1160°C$, a lithium niobate crystal exhibits mirror symmetry about three planes that are 60 °apart, with three-fold rotational symmetry around the axis given by the intersection of these three planes, as shown in figure 3.2. These two symmetry properties classify $LiNbO_3$ as a member of the R3c space group, with point group 3m [24], [25]. There are three possible cells which can be used to describe the structure of the $LiNbO_3$ crystal: rhombohedric, hexagonal and orthohexagonal. The most common in literature is the last one (figure 3.2), with the z-axis, which is also usually referred to as c-axis, along the axis of three-fold rotation symmetry, y-axis laying on a mirror plane and x-axis perpendicular to the others[2].
Lithium niobate's ferroelectricity has a direct impact on its atomic structure, as can be seen in figure 3.3. In a slightly distorted hexagonal close-packed configuration, the structure consists of oxygens distributed in planar sheets. Lithium, niobium, and vacancies along the c axis regularly fill the oxygen-filled octahedral. In the paraelectric phase, for $T \geq T_C$, the oxygen planar sheets are where lithium ions are aligned, while niobium ions are placed in the middle

[1] A uniform growth by this technique is only achievable in the *congruent* composition (Li:Nb =48.5:51.5) which corresponds to a lithium deficiency compared to the stoichiometric composition, as can be seen in figure 3.1.[25]

[2] Directions of these axis are choosen by using the piezoelectricity of the material: +z-axis points toward the z face that becomes negatively charged under uniaxial compression [25].

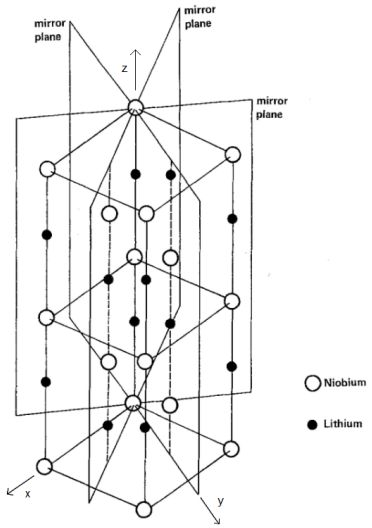

Figure 3.2: Orthohexagonal cell of $LiNbO_3$ and symmetry planes [24].

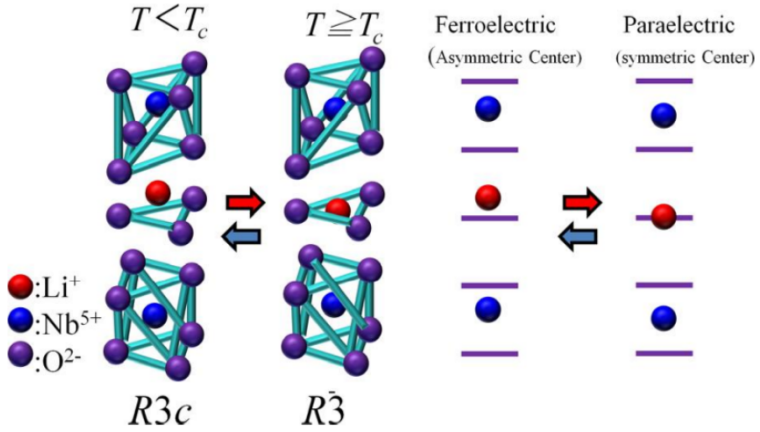

Figure 3.3: Structure of $LiNbO_3$ in the two phases. The horizontal purple lines on the right represent the oxygen planes. Image is taken from [28].

of the previous mentioned octahedras: in this case, the material does not show polarity. In the ferroelectric phase ($T < T_C$), a spontaneous polarization arises due to a 44 pm shift of lithium ions from the oxygens planes in the positive direction of the c-axis; in this case, niobium ions are displaced of 27 pm from the center of octahedras in the same direction.

3.1.1 Physical properties

Lithium niobate is a material that is widely used in integrated optics because of its unique electro-optical, non-linear optical, piezoelectric and photorefractive properties that can be utilized in microfluidic devices. Specifically, the combination of birefringence and electro-optical properties as well as the development of integrated wave guide made this material to become really attractive for modulator application since the beginning of '70, especially in the telecom spectrum. [29].

Optical properties

Lithium niobate is a transparent crystal with high optical transmittivity in the range of $350 - 3500$ per nm. The birefringence of the permittivity tensor is highlighted by the anisotropy of the permittivity tensor in the othohexagonal cell reference framework:

$$\bar{\epsilon} = \begin{bmatrix} \epsilon_{11} & 0 & 0 \\ 0 & \epsilon_{11} & 0 \\ 0 & 0 & \epsilon_{33} \end{bmatrix} \tag{3.1}$$

and starting from ϵ_{11} and ϵ_{33} it is possible to define $n_o = \sqrt{\frac{\epsilon_{11}}{\epsilon_0}}$ and $n_e = \sqrt{\frac{\epsilon_{33}}{\epsilon_0}}$ which are, respectively, the ordinary refraction index seen by light polarized in any direction perpendicular to the c-axis, and the extraordinary refraction index, seen by light polarized in the direction parallel to the c-axis [25]. The presence of extrinsic impurities and wavelength are the two factors that determine these indices. The Sellmayer equation provides an approximation of the dispersion relation [30]:

$$\begin{aligned} n_i^2 = &\frac{50 + C_{Li}}{100} \frac{A_{0,i}}{(\lambda_{0,i} + \mu_{0,i}F)^{-2} - \lambda^{-2})} \\ &+ \frac{50 - C_{Li}}{100} \frac{A_{1,i}}{(\lambda_{1,i} + \mu_{1,i}F)^{-2} - \lambda^{-2})} + A_{UV} + A_{IR,i}\lambda^2 \end{aligned} \tag{3.2}$$

$$F = f(T) - f(T_0)$$

$$f(T) = (T + 273)^2 + 4.0238 \cdot 10^5 \left[coth\left(\frac{261.6}{T + 273}\right) - 1 \right]$$

where the index i refers to the two possible refractive indices, C_{Li} denotes the lithium content of the crystal, expressed in mol%, λ is the wavelength expressed in nanometers and $T_0 = 24.5\,°C$. Coefficients $A_{0,i}$ are related the contribution given by Nb on Nb sites, while $A_{1,i}$ of Nb on Li sites. A_{UV} and A_{IR} account for, respectively, far UV contribution due to plasmons and IR region contributions given by phonons. Table 3.1 shows an example for the parameters in equation 3.2.

	Ordinary	**Extraordinary**
A_0	$4.5312 \cdot 10^{-5}$	$3.9466 \cdot 10^{-5}$
A_1	$2.7322 \cdot 10^{-5}$	$8.3140 \cdot 10^{-5}$
λ_0	223.219	218.203
λ_1	260.26	250.847
μ_0	$2.1203 \cdot 10^{-6}$	$7.5187 \cdot 10^{-6}$
μ_1	$-1.8275 \cdot 10^{-4}$	$-3.8043 \cdot 10^{-5}$
A_{UV}	2.6613	2.6613
A_{IR}	$3.6340 \cdot 10^{-8}$	$3.0998 \cdot 10^{-8}$
n	**2.2866**	**2.2028**

Table 3.1: Fitted parameters for the Sellmayer equation 3.2 [30]; μ_0 and μ_1 are coefficients for the temperature dependence. The refractive indices values are obtained for room temperature and a wavelength $\lambda = 632.8$ nm.

Electro-optic effect

The applied electric field affects the refractive index of a solid, which is the result of this electro-optic effect. The second order tensor variation can be used to describe the relationship between the refractive index variation and the electric field $\Delta\left(\frac{1}{n^2}\right)_{ij}$:

$$\Delta\left(\frac{1}{n^2}\right)_{ij} = \sum_k r_{ijk}E_k + \sum_{k,l} s_{ijkl}E_kE_l + ... \tag{3.3}$$

where the latter contains only linear and quadratic terms in the electric field. The expression of the two tensors r_{ijk} and s_{ijkl} is based on the structure of the material; moreover, they relate respectively to the linear electro-optical effect – also known as the Pockels' effect – and to the quadratic effect – generally known as the Kerr effect. The Kerr effect is not negligible for electric fields with a modulus higher than 65 kV mm^{-1} [31], whereas the Pockels' effect is the dominant effect in lithium niobate. Finally, The Pockels' tensor can be simplified because of its symmetric structure in the following matrix shape:

$$\bar{r} = \begin{bmatrix} 0 & -r_{22} & r_{13} \\ 0 & r_{22} & r_{13} \\ 0 & 0 & r_{33} \\ 0 & r_{42} & 0 \\ r_{42} & 0 & 0 \\ -r_{22} & 0 & 0 \end{bmatrix} \tag{3.4}$$

where:

r_{13}	r_{22}	r_{33}	r_{42}
$8.6 \cdot 10^{-12}$	$3.4 \cdot 10^{-12}$	$30.8 \cdot 10^{-12}$	$28.0 \cdot 10^{-12}$

Table 3.2: Coefficients of the Pockels' tensor 3.7 expressed in m V^{-1} [32].

Pyroelectric effect

The polarization of a pyroelectric solid changes spontaneously, which is present in the ferroelectric phase for $T < T_C$, as a function of temperature: the movement of lithium and niobium ions with respect to the oxygen sheets is responsible for this effect in lithium niobate. The relationship between the polarization vector change, ΔP_i and the temperature variation ΔT may be expressed as follows can be expressed as:

$$\Delta P_i = \rho_i \Delta T \tag{3.5}$$

with $\rho_x = \rho_y = 0$ and $\rho_z = -4 \cdot 10^{-5}$ C m^{-2} K^{-1}, Li and Nb ions are only able to move in the direction that is parallel to the c-axis.

Piezoelectric effect

In response to mechanical stress, lithium niobate exhibits piezoelectricity, which is the appearance of induced polarization in a solid. Therefore, the latter can affect the spontaneous polarization of the crystal. In the orthogonal cell system, this can be described in tensor component form:

$$P_i = \sum_{j,k} d_{ijk}\sigma_{jk} \tag{3.6}$$

where σ_{jk} stands for the applied stress and d_{ijk} is the piezoelectric tensor. The piezoelectric tensor in lithium niobate only has 4 independent components due to its crystal symmetry:

$$\bar{d} = \begin{bmatrix} 0 & 0 & 0 & 0 & d_{15} & -2d_{22} \\ d_{22} & d_{22} & 0 & d_{15} & 0 & 0 \\ d_{31} & d_{31} & d_{33} & 0 & 0 & 0 \end{bmatrix} \tag{3.7}$$

with two subscripts jk properly mapped in one index [24]. This tensor also describes the inverse piezoelectric effect, i.e., the deformation (strain) induced on the material by an applied electrical field. If S_{ij} is the second-rank tensor describing the strain on the material, it can be shown that [25]:

$$S_{jk} = \sum_i d_{ijk} E_i \tag{3.8}$$

Bulk Photovoltaic effect

This effect generally occurs in crystals with a non-centro-geometric structure [33; 26] and is related to photoexcitation and re-combination phenomena: the absorbing centers in the material generate a current through the excited electrons by means of optical interactions and their movement to the neighbouring ions is directed in a preferential manner. The bulk photovoltaic current can be observed even under uniform illumination, contrary to the usual photovoltaic current which requires a heterogeneity of the medium or non-uniformity of the light beam affecting the material. In the case of $LiNbO_3$ the first observation and explanation of this effect occurred in 1974[34], reporting a stationary current in the crystal after it has been illuminated by a homogeneous light. The photovoltaic current can be expressed as:

$$j_{phv,i} = \beta_{ijk} e_j e_k^* I = \alpha k_{G,ijk} e_j e_k^* I \tag{3.9}$$

where $\beta_{ijk} = \beta_{ikj}^*$ is the complex photovoltaic tensor, e_j and e_k are unit vectors describing the polarization of light, while I is the light intensity. If the light absorption coefficient α of the material (assumed to be isotropic) is considered, one can define the so-called Glass constant $k_{G,ijk} = \beta_{ijk}/\alpha$: it describes the photovoltaic activity of a given impurity in the specific lattice. Actually the real and imaginary parts of β_{ijk} tensor are, respectively, symmetric and anti-symmetric in the indices k and j; for a linearly polarised light, only the real part is taken into account [26]. In the case of symmetry, the photovoltaic tensor has the same structure as the piezoelectric tensor, d_{ijk}: therefore $LiNbO_3$ photovoltaic tensor has only four independent components: $\beta_{311} = \beta_{322}$, β_{333}, $\beta_{222} = -\beta_{112} = -\beta_{121} = -\beta_{211}$, $\beta_{113} = \beta_{223}$. The generated photovoltaic current is mainly directed along the z-axis (c-axis), since $k_{G,333} = 2.7 \cdot 10^{-9}$ cm V^{-1} and $k_{G,322} = 3.3 \cdot 10^{-9}$ cm V^{-1}, while, for example, the generated current along the y-axis is one order of magnitude lower, with $k_{G,222} = 0.3 \cdot 10^{-9}$ cm V^{-1} [25] [35].

Photorefractive effect

The combination of electro-optic and photovoltaic effects is what generates the photorefractive effect, which is consequently not a single effect: it consists of the variation of the index of refraction of a material when it is exposed to light illumination. The process is a two-step one: charge migration is followed by electro-optic effect [24]. In general, charge migration can be caused by both photovoltaic effects and diffusion and drift phenomena. In a photorefractive material, such as lithium niobate, the light energizes the electrons at the donor level, which change state and move through the conduction band. Electrons will move to unilluminated regions until acceptors' centers are reached if the light pattern illuminating the crystal is not uniform, causing a non-uniform charge distribution that leads to an internal space-charge electric field. This generated field modulates the material's refractive index through electro-optical effect.

Photorefractivity cannot be achieved without the presence of intrinsic or extrinsic impurities with two valence states: in lithium niobate, niobium antisite plays both a donor and acceptor role, since Nb^{4+} acts as a donor state while Nb^{5+} as an acceptor state. Doping the material with specific impurities in two valence states can enhance the photovoltaic and photorefractive effect: one of the most common choice for doping is iron, which grants the two states Fe^{2+}, acting as a donor, and Fe^{3+}, acting as an acceptor [25], [36].

3.2 The photoinduced electric field

The one-center model, which is well-known in literature, is presented in this section at first; we provide thus a detailed theoretical derivation of the field's time-dependence.

Photoinduced fields are usually used in order to realize a particular configuration, known as "virtual[3] microelectrodes": in fact, the creation of localized, space-tailored electric fields can be achieved by using lithium niobate's photovoltaic effect.

3.2.1 Photo-induced charge transport

As already mentioned, the charge transport of photoinduced carriers has three main components: drift, bulk photovoltaic effect and diffusion [26; 36; 37]. It is possible to write the total current inside the material as

$$\vec{j} = \vec{j}_{drift} + \vec{j}_{phv} + \vec{j}_{diff} \tag{3.10}$$

which has to satisfy Poisson and continuity equations:

$$\begin{aligned} \nabla(\bar{\epsilon}\vec{E}) &= \frac{\rho}{\epsilon_0} \\ \nabla \cdot \vec{j} + \frac{\partial \rho}{\partial t} &= 0 \end{aligned} \tag{3.11}$$

The drift current, also known as the ohmic current, occurs because of the presence of an electric field. The sum of contributions from both external and internal fields is typically used to determine the latter. Examples of the latter are the space-charge field generated by separation of trapped carriers and, in case of high intensity illumination, the pyroelectric field promoted by local heating of the crystal due to illumination itself [25]. However, pyroelectric contributions can be neglected for intensities lower than $10^5\ Wm^{-2}$ [38]. Drift current can be written as

$$\begin{aligned} \vec{j}_{drift} &= \bar{\sigma}\,\vec{E} \\ \bar{\sigma} &= q\bar{\mu}N \end{aligned} \tag{3.12}$$

where $\bar{\sigma}$ is the conductivity tensor, $\bar{\mu}$ and N are, respectively, mobility tensor and density of either holes or electrons, depending on the carrier type considered [25].
The asymmetric charge movement from the absorbing center to the nearest neighboring ions during optical excitation is what causes the bulk photovoltaic current. Charge carriers are excited with a preferred momentum, which is a typical mechanism for non-centrosymmetric crystals; they lose their directional properties only after thermalization, which is responsible for drift and diffusion currents, but not for photovoltaic ones, which has been described in section 3.1.1. The latter is characterized by the photovoltaic tensor β_{ijk}: in lithium niobate, the greatest current density is observed along the c-axis and is often expressed as scalar:

$$\frac{j_{phv,c}}{I} = \alpha k_G = \mu \tau_{phv} E_{phv,c} \frac{\alpha}{h\nu} \tag{3.13}$$

[3]The term *virtual* refers to the fact that there is no requirement for metal electrodes to generate an electric field on the material.

where k_G is the Glass constant, accounting for the anisotropy of the charge transport, and α is the absorbing coefficient [25]. k_G can be rewritten as $k_G = \mu\tau_{phv}E_{phv,c}/h\nu$, in which μ is the mobility of the carriers, τ_{phv} is the time within which carriers contribute to the photovoltaic current, $h\nu$ is the energy of the photon and E_{phv} is the phenomenological field moving the carriers.
The diffusion current is a result of spatial fluctuations in the concentration of charge carriers, N:

$$\begin{aligned} \vec{j}_{diff} &= -q\bar{D}\nabla N \\ \bar{D} &= \bar{\mu}\frac{k_B T}{q} \end{aligned} \tag{3.14}$$

with N, q and $\bar{\mu}$ depending on the type of carriers, electrons or holes.

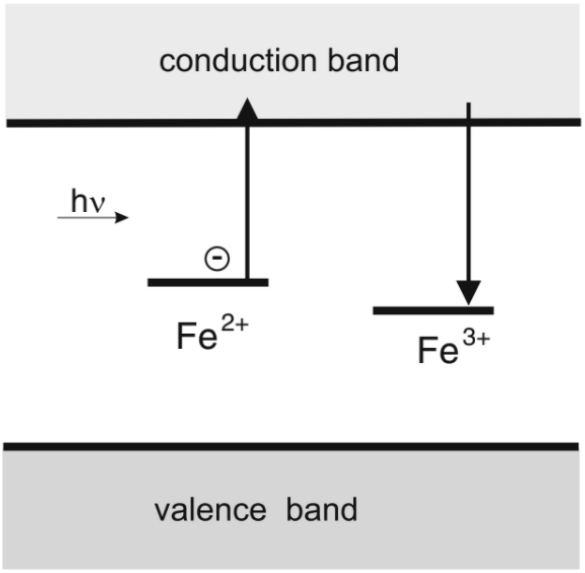

Figure 3.4: Sketch of the working principle of one-center model, taken from [26]. One incident photon excites one electron from the donor state Fe^{2+} to the valence band. Excited electron can then move in the conduction band by means of diffusion, drift and photovoltaic phenomenon until it is trapped by an acceptor state Fe^{3+}.

3.2.2 One-center model

Vinetskii and Kukhtarev's one-center charge-transport model is the first model that was developed to explain photorefractive effect [39]. In this model, only one photorefractive center is considered, iron in the case of Fe:$LiNbO_3$: as shown in figure 3.4, Fe^{2+} acts as a donor state, while Fe^{3+} is the acceptor one. The following equations give a description of the time evolution of carriers' density and their current.

$$\frac{\partial N_i}{\partial t} = (sI + \beta_T)N_{Fe^{2+}} - \gamma_i N_i N_{Fe^{3+}} - \frac{\nabla \cdot \vec{j}}{q} \tag{3.15}$$

$$\frac{\partial N_{Fe^{2+}}}{\partial t} = -\frac{\partial N_{Fe^{3+}}}{\partial t} = -(sI + \beta_T)N_{Fe^{2+}} + \gamma_i N_i N_{Fe^{3+}} \tag{3.16}$$

$$\vec{j} = \mu_i N_i \vec{E} - qD_i \nabla N_i + sN_{Fe^{2+}} k_G I \hat{j} \tag{3.17}$$

where N_i, γ_i, μ_i and D_i are respectively the density, recombination, mobility and diffusion constant of the carriers considered (either electrons or holes, $i = e, h$), s is the photoionization

cross section, I is the intensity illumination, β_T is the thermal generation rate, $N_{Fe^{2+}}$ and $N_{Fe^{3+}}$ are respectively the density of donors and acceptors, while $\vec{E}$ is the total applied field (sum of an eventual external one and a space-charge field) [25]. The current $\bar{j}$ accounts for all the three types of charge transportation discussed in 3.2.1.
The space-charge electric field $\vec{E}_{sc}$ has to obey to the Poisson equation

$$\nabla(\bar{\epsilon}\epsilon_0\vec{E}_{sc}) = \rho = q(N_i + \Delta N_{Fe^{2+}}) \tag{3.18}$$

with $\Delta N_{Fe^{2+}}$ Showing the difference in donor density when there is no illumination.

Equation 3.18 can be simplified, since N_i (standard value 10^{14} m^{-1}) is usually much smaller than $\Delta N_{Fe^{2+}}$ (standard value 10^{24} m^{-1}) and can therefore be neglected [25]. In addition, also the previous set of equations 3.15, 3.16 and 3.17 can be further simplified: under illumination, N_i reaches a nearly instantaneous equilibrium state, according to the adiabatic approximation. Therefore, after this short time it is possible to assume $\frac{\partial N_i}{\partial t} = 0$, implying that carriers are always in a quasi-equilibrium state with trap distributions at any given moment. In $LiNbO_3$ this is a good approximation for long illumination time, since the initial rise time of N_i is of the order of picoseconds [37]. Moreover, within adiabatic approximation, also $\frac{\partial N_{Fe^{2+}}}{\partial t} = 0$ holds, which does not mean that $N_{Fe^{2+}}$ has reached a steady state, since it is present a small and slow contribution due to charge transports [25]. This approximation allows to get an estimate of N_i at any time and any place; this can bee seen from equation 3.16:

$$N_i = \frac{(sI + \beta_T)}{\gamma_i}\frac{N_{Fe^{2+}}}{N_{Fe^{3+}}}. \tag{3.19}$$

By inserting the latter equation in equation 3.12, one has

$$\begin{aligned}\sigma_i &= q\mu_i\frac{sI}{\gamma_i}\frac{N_{Fe^{2+}}}{N_{Fe^{3+}}} + q\mu_i\frac{\beta_T}{\gamma_i}\frac{N_{Fe^{2+}}}{N_{Fe^{3+}}} = \\ &= \sigma_{phv,i} + \sigma_{dark,i}\end{aligned} \tag{3.20}$$

it is clear that conductivity σ_i is made up of two contributions: the first, $\sigma_{phv,i}$ is the so-called photoconductivity (different from zero only if the material is illuminated) $\sigma_{dark,i}$ is the second contribution, called dark conductivity, which is a result of the thermal excitation of charge carriers and does not depend on illumination. Both $\sigma_{phv,i}$ and $\sigma_{phv,i}$ display the same dependence on the so-called reduction degree $\frac{N_{Fe^{2+}}}{N_{Fe^{3+}}}$, as confirmed by several experiments on Fe:$LiNbO_3$ [40]. However, for intensity $I > 1$ Wcm^{-2}, thermal excitation is negligible and hence $\sigma_{phv,i}$ is the dominant contribution [25].

Dark conductivity is a significant characteristic of photorefractive materials. Even though in the presence of illumination $\sigma_{dark,i}$ is often negligible compared to the photoconductivity, it becomes the dominant contributor influencing the temporal evolution of the spatial charge field when the lighting is turned off. In dark conditions, this field decays due to dark conductivity, which may be an obstacle for applications that require the electric field to persist over time or that need a quick vanishing of photo-induced field.
Storage time in dark conditions of space-charge field up to 1 year have been measured in low-doped Fe:$LiNbO_3$ [41], with dark conductivity of the order of $10^{-16} - 10^{-18}$ Ω^{-1}cm^{-1} (room temperature). In high-doped crystals, decay process is faster and typical storage time is around hours, minutes or seconds [25], [42].

Non-homogeneous illumination solution

An analytical solution for the set of equations 3.15, 3.16 and 3.17 can be obtained if two plane waves create a sinusoidal interference pattern. Therefore, for simplicity, a one-dimensional light pattern produced by the interference of two plane wave-vectors $\vec{k_1}$ and $\vec{k_2}$ along z-axis is considered in the following:

$$I(z) = I_0(1 + m\, sin(\vec{k} \cdot \hat{z})) \tag{3.21}$$

where $I = \frac{I_1+I_2}{2}$ is the average intensity, $m = \frac{I_{max}-I_{min}}{I_{max}+I_{min}}$ is the pattern visibility and $\vec{k} = \vec{k_1} - \vec{k_2}$ [25]. The solution was first obtained by Kukhtarev et al. [39] by developing in Fourier series all the involved quantities in equations 3.15, 3.16 and 3.17 that depend on spatial coordinate $\hat{z}$. If modulation is small, i.e. $m \ll 1$, then only zero- and first-order terms can be considered, since any other k-th Fourier term is quickly decreasing with m^k. Each quantity $X(t)$ depending on $\hat{z}$ coordinate can thus be rewritten as $X(t) = X^{(0)} + X^{(1)}\, e^{i\vec{k}\cdot\hat{z}}$, with $X(t) = \vec{E}, N_{Fe^{2+}}, N_{Fe^{3+}}, N$. The following illustrates how the three equations can be simplified (for convenience, $E^{(0)} = E_0$):

$$\begin{aligned}
E_{sc} \approx E^{(1)} &= -\frac{E_0 + E_{phv} + iE_D}{1 + E_D/E_q - iE_0/E_q - iE_{phv}/E_{q'}} \\
E_{phv} &= \frac{j_{phv}}{\sigma_{phv}} = \frac{k_G \gamma_i}{q\mu_i} N_{Fe^{3+}} \\
E_D &= \frac{k_B T}{q} K \\
E_q &= \frac{q}{\epsilon\epsilon_0 K} \left(\frac{1}{N_{Fe^{2+}}} + \frac{1}{N_{Fe^{3+}}} \right)^{-1} \\
E_{q'} &= \frac{q}{\epsilon\epsilon_0 K} N_{Fe^{2+}}
\end{aligned} \tag{3.22}$$

where E_D is the diffusion field, E_{sc} is the space-charge generated field, E_q and $E_{q'}$ are, respectively, the space-charge limiting fields, and $K = \vec{k} \cdot \hat{z}$ [25]. The maximum amplitude of the space-charge field generated by electrons transport inside the material is referred to as E_q when the light frequency and light pattern are fixed. The one-center model is able to provide also the time evolution of space charge field, which turns out to be described by an exponential law with time constant

$$\tau_{sc} = \frac{1 + (E_D - iE_0)/E_M}{1 + E_D/E_q - iE_0/E_q - iE_{phv}/E_{q'}} \tau_M \tag{3.23}$$

$$E_M = \frac{\gamma_i N_{Fe^{3+}}}{\mu_i} \frac{1}{K} \tag{3.24}$$

$$\tau_M = \frac{\epsilon\epsilon_0}{\sigma_{phv,i} + \sigma_{dark,i}} \tag{3.25}$$

From equation 3.25 it is clear that if $\sigma_{phv,i} \gg \sigma_{dark,i}$, then $\tau \propto \sigma_{phv,i}^{-1}$. On the other hand, it is also evident that a significant dark conductivity, when compared to the photoconductivity, leads to a decreasing of τ_M [25].

Simplified first approximation solution

To significantly simplify one-center model equations, some assumptions can be made [25]:

- $E_0 = 0$, i.e. no external field was applied to the lithium niobate sample.

- $i = e$, since in the case of iron-doped lithium niobate [38] and visible light, electrons dominate over holes in transport mechanisms. Equations listed above are the same for both holes and electrons, therefore if electrons provide the most important contributions, $i = e$ holds.

- $Eq \gg E_D$, $E_{q'} \gg E_{phv}$, which means that no space-charge limiting effects are present: in the material enough donors and acceptors are available to support the building up of the space-charge electric field.

- $E_{phv} \gg E_D$; in Fe:$LiNbO_3$ this relation holds for light modulation larger than 1μm [36]. In this work, this condition is verified.

The above assumptions imply also that $E_M \gg E_D$ and accordingly $\tau_M \approx \tau_{sc}$. By inserting equations 3.21 and 3.22 in one-center model rate equations 3.15-3.17 and by using previous assumptions, the time evolution of the space-charge electric field during its establishment (equation 3.26) and its fading out (equation 3.27) can be obtained:

$$E_{sc}(t) = -E_{phv}(1 - e^{-t/\tau_{sc}}) \tag{3.26}$$

$$E_{sc}(t) = E_{sc,0}\ e^{-t/\tau'_{sc}} \tag{3.27}$$

where the saturation value of the space-charge field E_{sc} for $t \gg \tau_{sc}$ is given by the bulk photovoltaic field, and where $E_{sc,0}$ is the value of the space-charge field at the beginning of the fading out process, when illumination has been switched off [25].
Considering that in Fe:$LiNbO_3$ $\sigma_{phv,i} \gg \sigma_{dark,i}$ for illumination intensities $I > 1$ Wcm^{-2}, some useful dependencies can be obtained from the previous analysis:

$$j_{phv} \propto I\, N_{Fe^{2+}} \tag{3.28}$$

$$\tau \propto \sigma_{phv}^{-1} \propto \frac{1}{I}\frac{N_{Fe^{3+}}}{N_{Fe^{2+}}} \tag{3.29}$$

$$E_{phv} \propto N_{Fe^{3+}} \tag{3.30}$$

All of these three dependencies have been experimentally verified [25; 37; 43].
Assuming that the density profile of the accumulated space charge in correspondence with the focus of the laser beam is Gaussian, it is possible to show that the electrical saturation field that arises in a 0.01 % mol iron-doped lithium niobate z-cut crystal is of the order of $10^5 - 10^6$ V/m [44].

A first **crucial consideration** concerns the real electric field: while EHD envisages the possibility to have spatial-dependent fields, it does not address generic time-varying ones[4]. With respect to what has been previously stated in section 1.1, equation (3.26) shows that the electric field we deal with in this real situation is a time-dependent one. It is reasonable to assume that after an interval of 4τ the field will be constant over time, with its value corresponding to the "saturation" one since:

$$E_{sc}(4\tau) = -E_{phv}(1 - e^{-1/4}) \sim -E_{phv}. \tag{3.31}$$

All measurements on the response of the droplet are performed way after switching on the electric field: this means that equation (3.31) is valid and that, unless negligible fluctuations of the value of the external imposed field, we work with a DC one. Therefore, all electrohydrodynamic laws can be employed.

[4]Except for periodic ones, but it is not our case.

3.3 Microdroplets

Analyzing the main elements of microfluidics and droplet generation is necessary in relation to the real water droplet.

3.3.1 Microfluidics

Microfluidics is the science of systems which handle or process small quantities of fluids, ranging from μL to pL and employing channels with dimensions between 10 and 500 μm [45]. Microfluidic devices are able to sample small volumes, while also allowing for low cost and fast analysis, with high resolution [46].
Microfluidics is characterized by values of Reynolds number R_e such that

$$R_e = \frac{\rho d v}{\mu} < 100 \tag{3.32}$$

where ρ is the density of the fluid, v is the average velocity, d is the characteristic linear dimension of the flow and μ is fluid's viscosity. Laminar flows and no mixing between different phases are characteristic of microfluidic channels due to low values of R_e, making microfluidics compatible with the production of controlled emulsions of two or more immiscible fluids.
The production and subsequent high-precision manipulation of very small volumes of fluids has led to an increase in interest in droplet microfluidics in recent years: this feature makes it a promising candidate for chemistry, biological and medical applications [47; 48]. By utilizing specific geometries, it is possible to produce droplets of a phase, commonly known as dispersed phase, into another one, the continuous phase. Among the most used we can find the T-junction (or the cross-junction)[5]. In the most general case, a micro-fluidic droplet circuit is composed of different microchannels with droplets of typical size. Upon production, the droplets from the dispersed phase are transported inside the continuous phase through the main microfluidic channel. Their movement within the channel is akin to rolling against the channel's walls compared to pure translation [49]. The formation of a thin lubrication film composed of continuous phase between the droplet's surface and the channel walls is what distinguishes single droplet transit.
High precision fabrication processes are required for microfluidic channel sizes. Microchannel circuits can be achieved with a high level of precision on polymeric substrates like PDMS and PMMA thanks to photolitography techniques [50; 51]. Despite this, these materials are not always suitable for a high level of integration. In addition, solvents can cause damage or swell with oil-based fluids in many instances. Only recently [35; 36; 47; 52], a valid alternative to polymeric materials for microfluidic and Lab-On-a-Chip applications has been proposed by lithium niobate.

3.3.2 Droplet generation: T-junction configuration

In literature, many kinds of droplets generators have been studied [53]. To guarantee high reproducibility, a droplet generator must have low dispersion in volume of droplets and a high range of droplets frequency. External pumps are necessary to inject both continuous and dispersed phases into the microchannels. Depending on the typology of external devices used in droplet production, droplet generators can be divided into two categories: active and passive generators. External energy sources other than pumps are involved in the former, such as external electric fields or mechanical valves, while the latter includes all the others generators relying mainly on pumps and on geometry of the microchannels [25].

[5]This junction will be further discussed in the following subsection.

In this work, a cross-junction droplet generator in T-junction configuration is used. Cross- and T-junction droplet generators are passive generators, both of them relying on a particular geometry of the junction between the main microchannel, in which continuous phase is made flowing, and the microchannel in which dispersed phases is injected [25]. A crosswise junction is formed when two microfluidic channels cross each other orthogonally in the cross-junction case, while in T-junction the two channels are crossed forming a T-shape junction, as the name itself suggests [47]. Both configurations are similar: a cross-junction with one extremity closed works as a T-junction, which is the configuration employed in this work. For this reason, in the following only T-junctions theory is discussed [25].

In a T-junction different working regimes can be achieved varying important parameters characterizing the system, such as injected fluxes Q_c, Q_d (respectively, continuous and dispersed phase flux), physical properties of employed fluids, such as density ρ_c, ρ_d, viscosity μ_c, μ_d, surface tension and/or wettability properties e.g. contact angle [25]. Depending on the mentioned parameters, three different well-defined working regimes can be identified [25], [35]:

- *Co-flow*: this is the case of fluids with similar viscosity, flowing in the channels with small velocities and with high wettability with channels surface. In this regime, the two phases flow parallel to each other and no droplets are produced.
- *Dripping*: opposing to the previous regime, in the dripping one droplets are produced at the T-junction. In this case, droplets can occupy completely the channel (except for a thin continuous phase film) or not. The first possibility is called *squeezing* regime and thanks to its stability, it is preferred in most of the cases and the one adopted in this work.
- *Jetting*: this is an intermediate regime, since droplets are generated after a small portion of the main channel, in which the two phases are co-flowing. This working condition is characterized by high frequency.

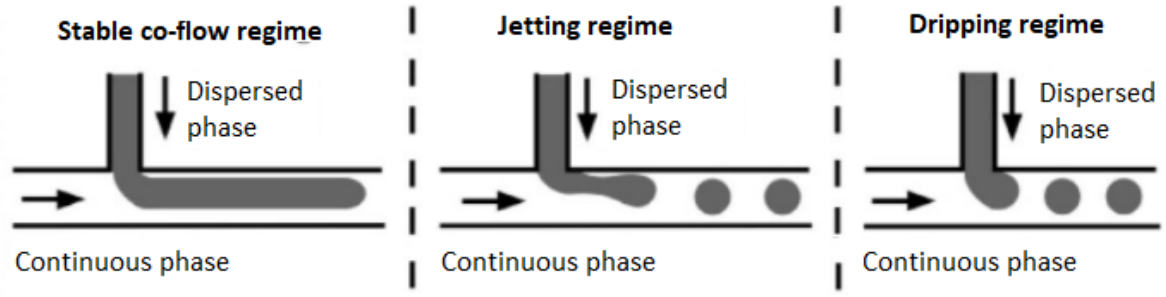

Figure 3.5: Sketch of the three typical working regimes in a T-junction. Image taken from [35].

Independently of the working conditions, droplets are produced thanks to the forces exerted by continuous phase on the dispersed phase entering the main channel at the fluid-fluid interface, causing the shearing off. These forces are due to capillary, drag and pressure contributions. Droplets production in this work is obtained within squeezing regime. Both squeezing and dripping regime are characterized by the size of the droplet during the break up at the junction. In squeezing, droplets completely obstruct the main channel before the break up and pressure term is the dominating one in this process. In dripping regime, droplets produced at the junction do not fill completely the main channel and in this case shear stress is the main contribution in the detachment. Garstecki et al. [54] proposed a model which takes into account the opposition

of the continuous phase flowing in the main channel to the dispersed phase tip growing at the fluid-fluid interface. The same work was also the first proposing to use capillary number Ca, i.e.

$$Ca = \frac{\mu v}{\gamma} \tag{3.33}$$

where γ is the surface tension, as a discriminating value between dripping and squeezing regimes. This parameter expresses the comparison between viscous stress and capillary pressure, that are the the dominating forces in the small geometries considered [25]. The final equation proposed for droplets length in squeezing regime is

$$\frac{L}{w_c} = 1 + \alpha \frac{Q_d}{Q_c} \tag{3.34}$$

where $\frac{L}{w_c}$ is the length of the droplet normalized to the width of the channel and α should in principle be w_d/w_c (see figure 3.6) but it is left as a fitting parameter. This relation has been experimentally verified by the same authors. Equation 3.34 drawback is that it provides a good agreement with experimental values only in squeezing regime, in a small range of Ca values. An improvement to the description of the dripping regime have been carried out by Christopher et al. [55]. Their model is described in detail in the following, since their resulting expression for droplets length can be traced back to equation 3.34.

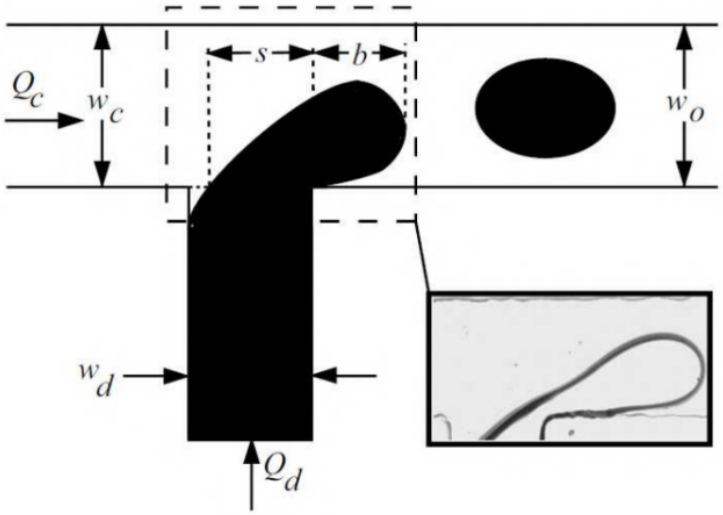

Figure 3.6: Sketch of the emerging droplet right before the break up instant as considered in Christopher et al. model. The image is taken from [55; 36].

The break up instant is considered as the instant when the three main forces acting are balanced:

$$F_\sigma + F_\tau + F_P = 0 \tag{3.35}$$

These three forces are:

- *Capillary force*:

$$F_\sigma \sim \left[-\sigma \left(\frac{2}{b} + \frac{2}{h} \right) + \sigma \left(\frac{1}{b} + \frac{2}{h} \right) \right] bh = -\sigma h \tag{3.36}$$

  that is given by the difference between Laplace pressure upstream, $\sigma \left(\frac{1}{b} + \frac{2}{h} \right)$, and downstream, $-\sigma \left(\frac{2}{b} + \frac{2}{h} \right)$, with respect to the droplet (curvatures are approximated), multiplied by the area of the interface bh (h is the depth of the channel).

- *Drag force*:

$$F_\tau \sim \mu_c \frac{v_c}{w_c - b} bh \sim \mu_c \frac{Q_c}{(w_c - b)^2} b \tag{3.37}$$

that is the force due to the viscous shear stress applied from the continuous phase flowing in the main channel on the emerging dispersed phase droplet. Shear rate is approximated by taking the ratio of the continuous phase velocity v_c in the gap between emerging droplet and channel's walls divided by the gap width $(w_c - b)$.

- *Squeezing pressure force*:

$$F_P \sim \Delta p_c bh \sim \mu_c \frac{v_c}{w_c - b} \frac{b}{w_c - b} bh \sim \mu_c \frac{Q_c b^2}{(w_c - b)^3} \tag{3.38}$$

which is obtained, as the authors specify, from a lubrication analysis [56] for the pressure during flow in a thin gap with aspect ratio $(w_c - b)/b$.

By substituting the three previous equations 3.36, 3.37 and 3.38 in equation 3.35, it is possible to obtain the length of the droplet during the shrinking of the neck, namely the dispersed phase volume connecting the emerging droplet within continuous phase and the dispersed phase completely within the side microchannel [25]. The contribution to the droplet length after the shrinking is approximated by $v_{growth} \cdot t_{squeeze}$, where $v_{growth} = Q_d/bh$ is the growth velocity and $t_{squeeze} \approx w_d/v_c \approx w_d w_c h/Q_c$ is the time between the neck shrinking and the break up. Combining the two contributions, the obtained length law is:

$$\frac{L}{w_c} = \bar{b} + \frac{\Lambda}{\bar{b}} \frac{Q_d}{Q_c} \tag{3.39}$$

where $\bar{b} = b/w_c$ and $\Lambda = w_d/w_c$. The Λ parameter is the same α parameter in Garstecki et al. model (equation 3.34) and in fact in squeezing regime, with $\bar{b} \to 1$ since b during detachment is close to the continuous channel width, equation 3.39 yields equation 3.34. With similar arguments, semi-empirical droplets frequency production trend for constant values of $\phi = \frac{Q_d}{Q_c}$ is derived as:

$$\bar{f} = f\, t_{cap} = f \frac{\mu_c w_c}{\sigma} \propto Ca^{\alpha_f} \tag{3.40}$$

where α_f is a parameter experimentally determined to be 1.31 ± 0.03.
Other theoretical models have been proposed, but the majority of them added further parameters to better reproduce experimental data trend without adding new physical considerations (see for example [57]). Both equations 3.39 and 3.40 have been experimentally verified [36] within $LiNbO_3$ group at University of Padua by exploiting an optofluidic platform integrated in lithium niobate.

3.4 The optomicrofluidic platform

Droplets are generated by exploiting an optofluidic chip [52]: a cross-junction is engraved on a Lithium Niobate (LN) substrate such that the main channel is perpendicular to an array of Ti-indiffused waveguides in a Mach-Zehnder interferometer (MZI) configuration coupled to laser light, allowing the detection of droplets flowing within the main channel (width $w_c = 200$ μm, height $h_c = 100$ μm) and the measurement of length and velocity of each single droplet. The substrate is sealed with a glass cover (thickness of around 1 mm). A detailed description of this optofluidic chip, including design and fabrication, has been provided by our group in [58].

An additional iron-doped lithium niobate (Fe:LN) cover (z-cut, 0.1 % Fe concentration) is integrated on top of glass cover in order to exploit Fe:LN bulk photovoltaic effect [26]. It is well-known [59; 60; 44] that by illuminating this material with suitably not-spatially homogeneous light (green, i.e. 532 nm) photoexcited electrons move in a preferential direction giving rise to a photocurrent (see section 3.2). The latter originates in turn a charge density which results in a local space-charge electric field. The shape of the crystal region in which the field is produced depends on the shape of the illuminated spot.
In this work a z-cut Fe:LN crystal is chosen since the photoexcited electrons move along the z-axis (c-axis) toward its positive direction. Hence the +z face is placed as close as possible to the glass cover, in order to maximize the field's lines entering the microchannel. The scheme of the chip is reported in **Figure 3.7**. The light illumination of the cover is provided by a solid state laser ($\lambda = 532$ nm) with a power of 65.0 mW. The bulk photovoltaic effect is obtained by illuminating the Fe:LN cover at the level of the microfluidic channel with the spot aligned with the MZI waveguide, coupled in turn with a continuous diode laser with power of 7.35 mW and a wavelength $\lambda = 532$ nm, enabling the detection of the flowing droplets and the measurement of length and velocity of each single droplet [58].

MilliQ® water is used as dispersed phase (flow rate Q_d) while Hexadecane (Sigma-Aldrich) with 3 % w/w concentration of SPAN® 80 surfactant (Sigma-Aldrich) as continuous phase (flow rate Q_c), hence producing water droplets dispersed in the latter. The surface tension between water and hexadecane with that surfactant concentration employed in this work was measured by pendant drop method obtaining $\gamma_0 = 4.27 \pm 0.04$ mN/m. The flow rates are controlled by a pressure pump OB1 MK3 (Elveflow, Paris, France) in feedback with flowmeters BFS Coriolis (Bronkhorst, AK Ruurlo, Holland). Liquids are injected in the chip through microfluidic inlets. A scheme of the opto-microfluidic setup is reported in **Figure 3.9**.

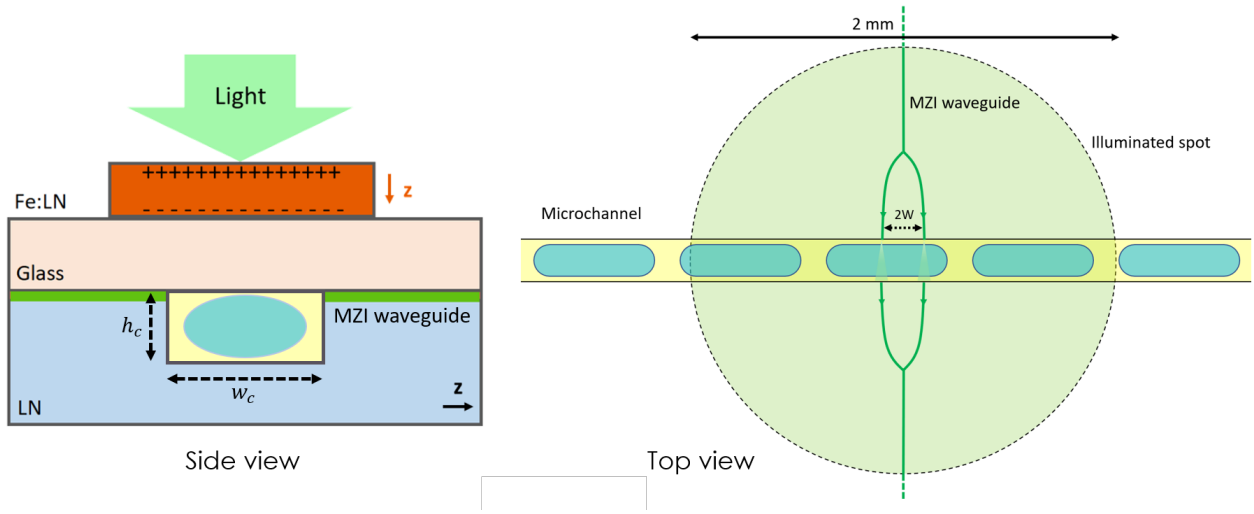

Figure 3.7: Scheme of the opto-microfluidic chip employed in this work. In the figure, $w_c = 200$ μm, $h_c = 100$ μm and $2W = 40$ μm. A detailed description of its design and fabrication and the opto-microfluidic setup employed to generate droplets has been previously provided in [58].

In order to evaluate the effects of the space-charge electric field, lengths and velocities of each generated train of droplets are measured before switching on the PhV-laser (corresponding to $t = 0$ minutes) and after its switching on. Each acquisition has a time duration Δt_i such that at least 100 droplets are detected for any chosen combination of flow rates.

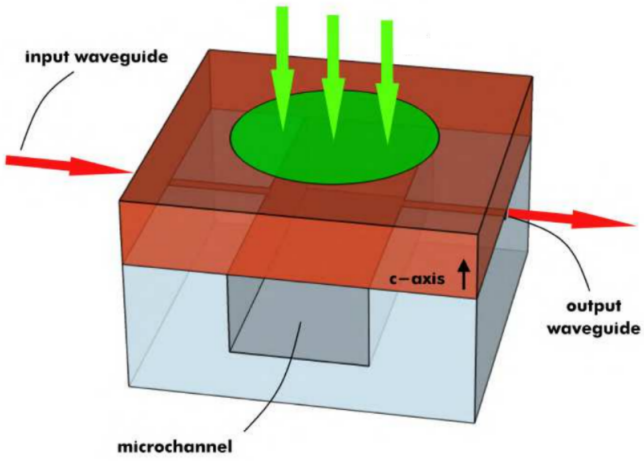

Figure 3.8: This is a simplified three-dimensional version (note that no glass cover is drawn) of the chip [36].

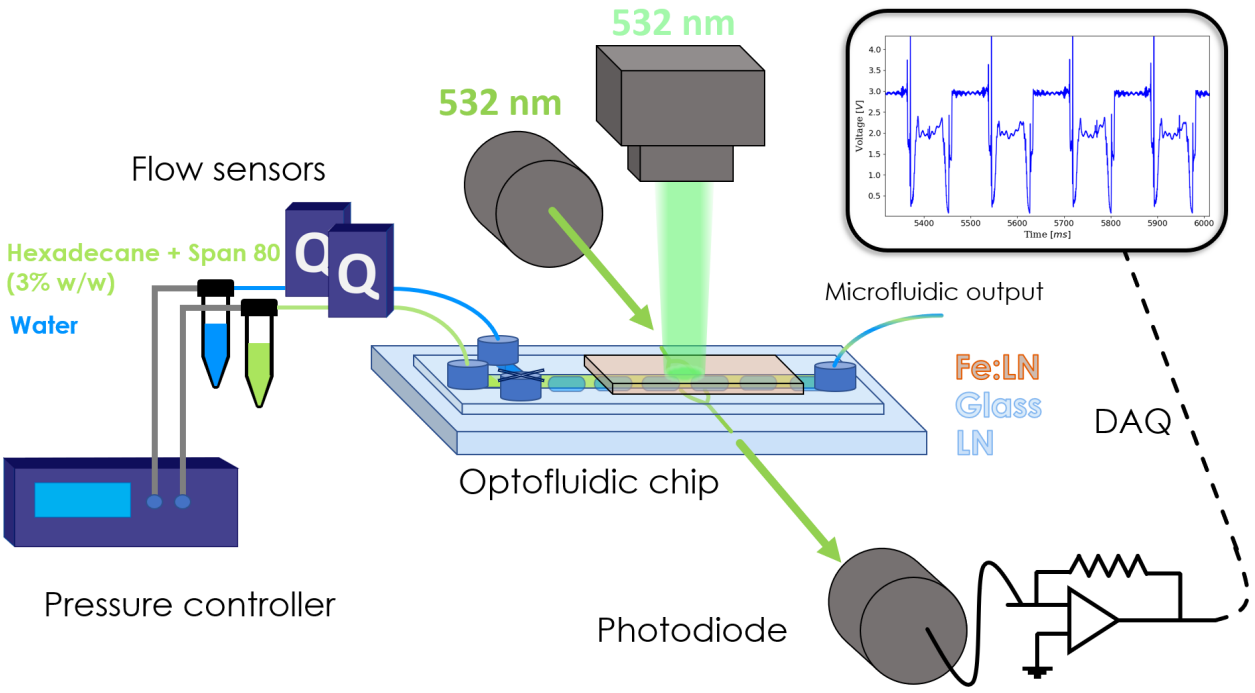

Figure 3.9: Scheme of the whole opto-microfluidic setup [25].

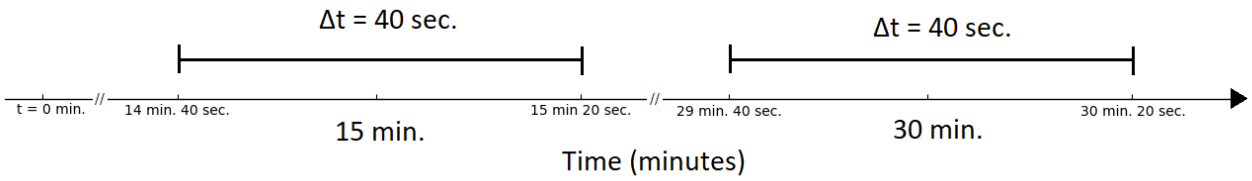

Figure 3.10: Schematic representation of the followed protocol to obtain data sets of at least 100 droplets [25].

The experimental conditions have been chosen so that one single droplet experiences the effect of the space-charge field. This is achieved by generating droplet with such a length that a single droplet can travel completely across the illuminated zone of the channel for a certain time interval.

With regard to single-drop motion, some considerations can be made. The transit in the illuminated zone of the channel can be substantially divided into steps, described in figure 3.11. Figure 3.11a shows the drop before entering the illuminated spot. Then the first one, (3.11b), shows the droplet entering the illuminated zone (coming from the non-illuminated part, 3.11a). From figure 3.11c to 3.11d each droplet travels through the illuminated zone of the microchannel.

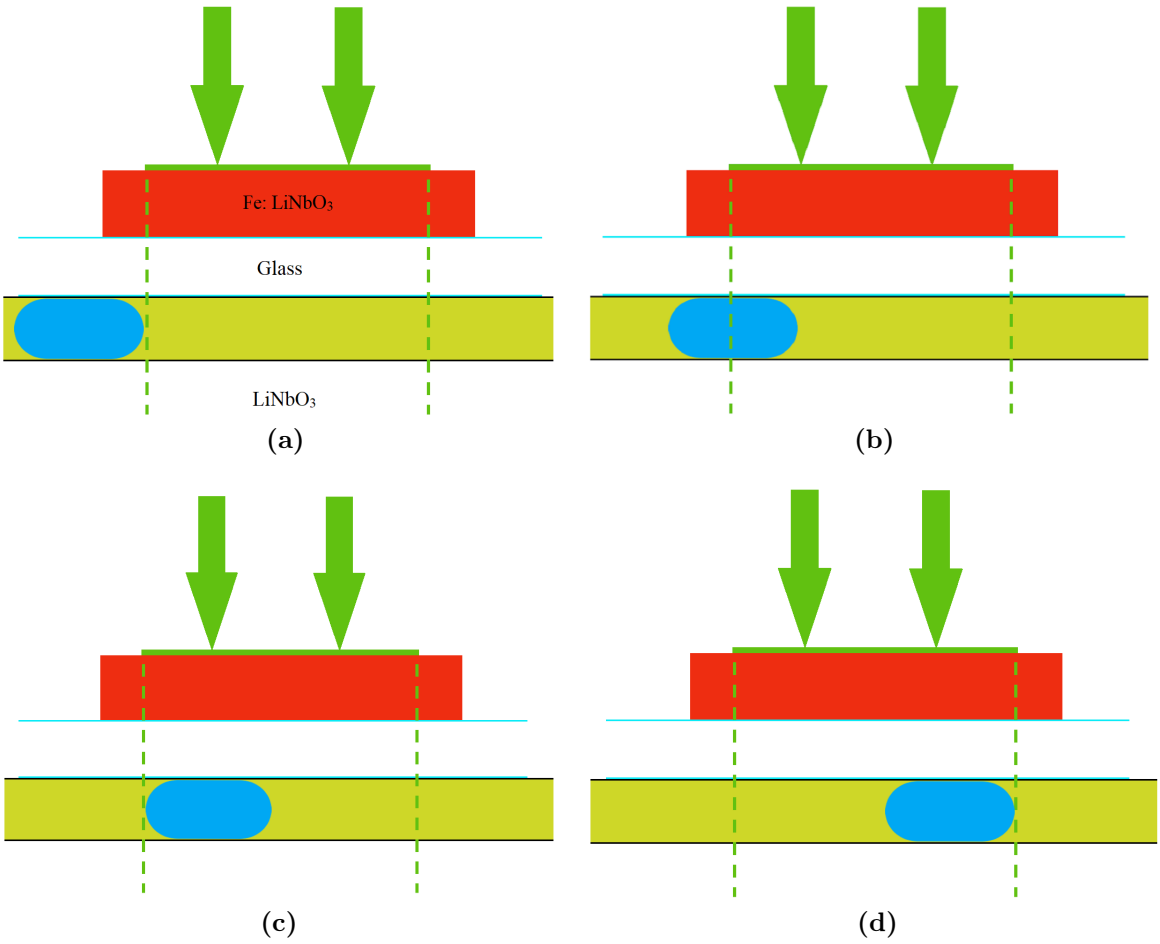

Figure 3.11: This figure is a schematic representation of droplet motion inside the microchannel (in yellow). Laser illumination is represented by the two green arrows, and the two dotted lines represent the limit of the beam spot produced on the iron-doped sample. Taken from [25].

3.5 The employed configuration

3.5.1 The real electric field

The real field distribution is quite complex to be modeled. The figure **3.12** below provides a schematic representation of the beam spot as seen from above the optofluidic platform, highlighting the dependence of saturation E_{sc} on x coordinate due to the shape of the spot. The figure is not to scale.

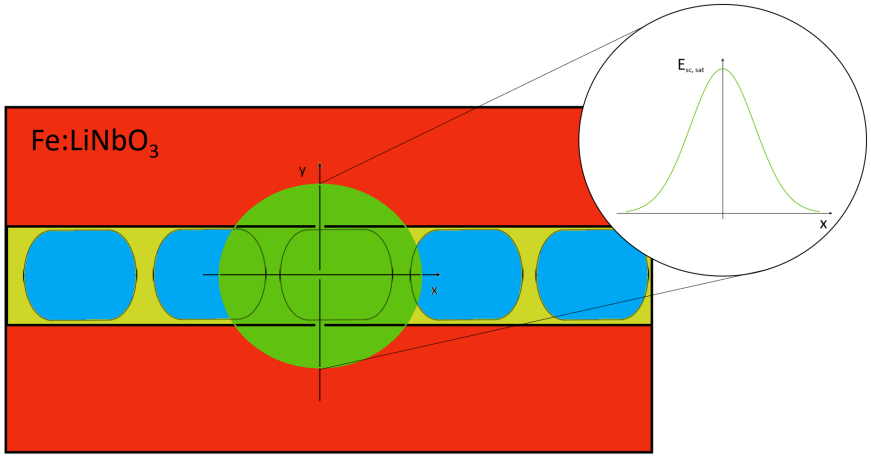

Figure 3.12: The beam spot is depicted in a schematic manner from a top view, demonstrating the dependence of saturation E_sc on the x coordinate due to the spot's shape. The figure is not to scale. Source [25].

In an attempt to provide an analytical description of this field, it is possible to divide the whole illuminated spot can into two parts by means of a circular crown. The outer part (in light green) is the one containing the curved field lines, whereas the inner circle is the uniform part of the field. As a first approximation, the curved part can be considered as a quadrupole field, and the uniform part as a linear one. This approach is one of extreme importance, as it emphasizes the role of the two components – linear and quadrupolar – and their relative strength.
There are two possibilities for the length of the nonuniform part, as can be seen from figures 3.14 and 3.13. It is assumed that the difference between the outer and inner radii of the circular crown is small with respect to the dimension of the drop.

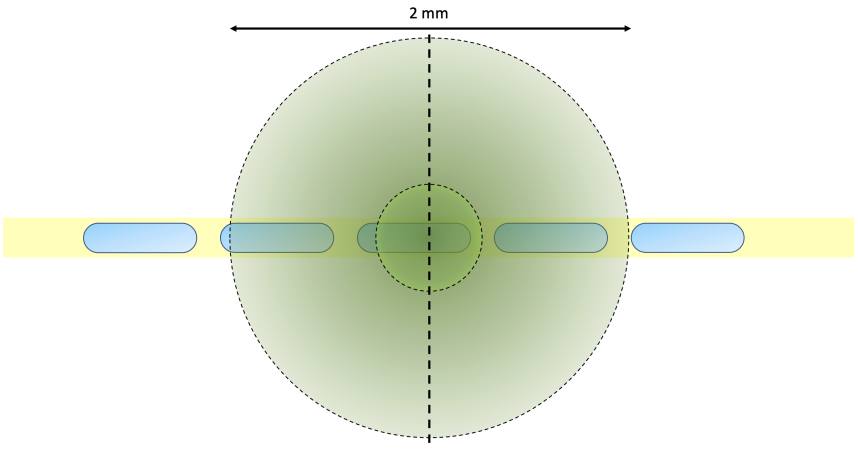

Figure 3.13: The discarded configuration for uniform and nonuniform parts. The figure is to scale.

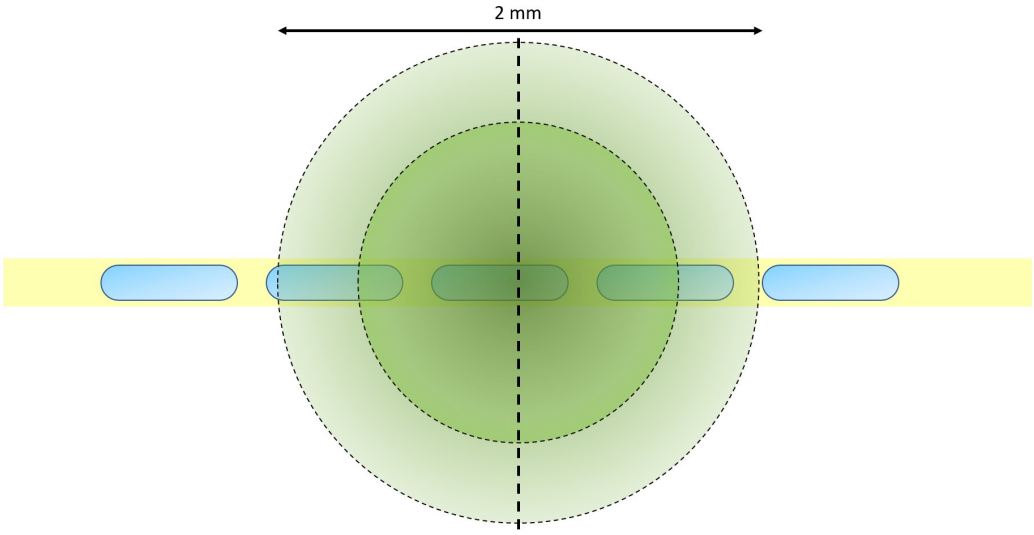

Figure 3.14: The chosen configuration. The figure is to scale.

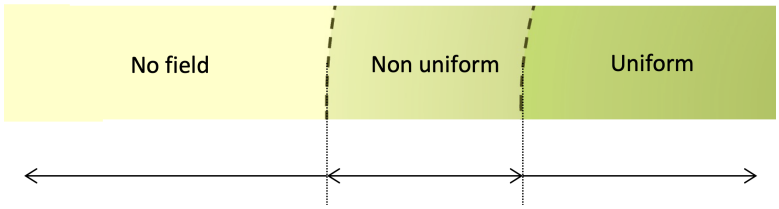

Figure 3.15: Magnification of the region of space where the drop enters/leaves the spot. The figure is not to scale.

Let us now consider the two following figures:

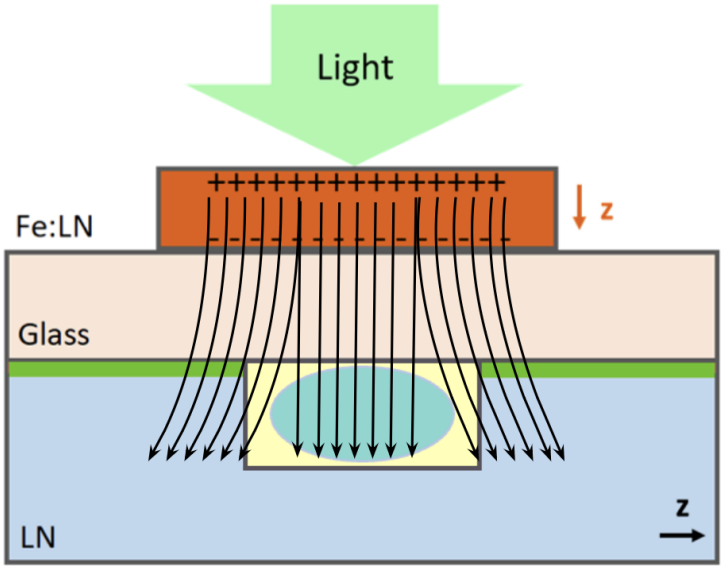

Figure 3.16: Front view of the chip where field lines are drawn. The figure is not to scale.

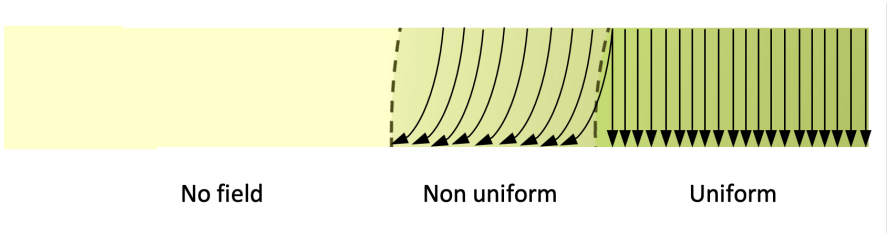

Figure 3.17: Lateral view of the chip where field lines are drawn. The figure is not to scale.

Since we assumed that the the difference between the outer and inner radii of the circular crown is small with respect to the dimension of the drop, the main contribution of the field to the deformation comes from the uniform part in which the deformation can be quantified as $r_\perp$; in fact, in our system $r_\parallel$ is fixed by channel confinement.

3.5.2 The real drop

Droplets that are subjected to measurements are therefore undergoing confinement due to the microchannel: this has clearly an influence on their three-dimensional shape. Actually, the drop is squashed between two parallel plates both from a *top-bottom* perspective and from a *left-right* one (see figure 3.21). The aforementioned parallel plates are actually planes of the microchannel.
Confinement is mainly due to the channel: for large and long drops that actually occupy a big portion of the channel, confinement acts directly on the shape of the drop, modifying it both from a top-bottom perspective and a left-right one. Moreover, the advancing and rear profiles of the drop (consequently contact angles, too) are not equal for the drops under study, as can be seen from the figure below:

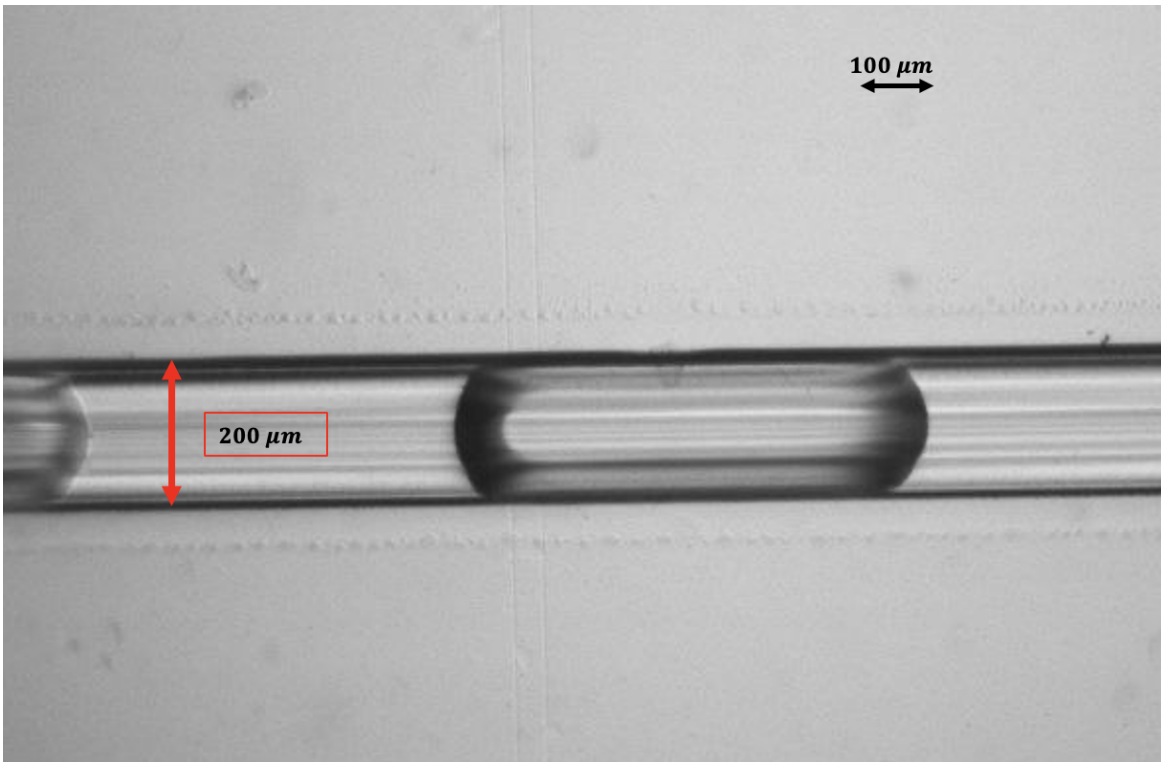

Figure 3.18: Top view of a drop flowing in the channel.

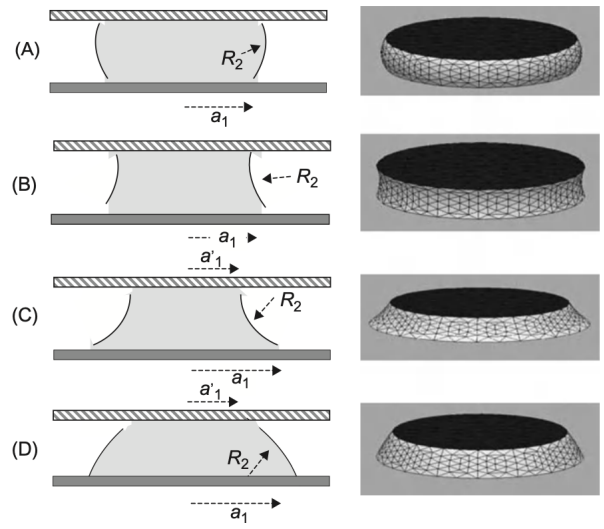

Figure 3.19: Sketch of the possible shapes assumed by a drop between two horizontal plates [10].

An analytical treatment for the shape of confined droplets has actually been proposed in a simpler situation of a *top-bottom* confinement in a symmetric case [10]. However, not only the adopted description – that is the case labeled by (A) – is distant from our real situation (this is in any case a problem we might have overcome by means of appropriate assumptions and approximations): as we will see in a moment, this model focuses mainly on calculating the volume of the drop, which will turn out to be an unnecessarily complex mathematical function itself.

Let us consider the cross-section of a droplet constrained by two parallel plates and having the same contact angle with both planes. This can be represented as:

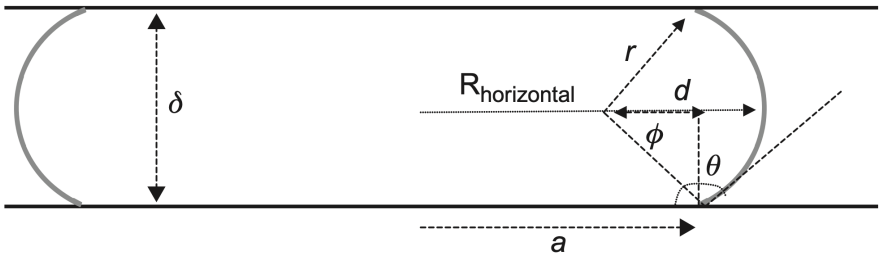

Figure 3.20: Diagram showing the geometry of a droplet that is confined to two parallel planes [10].

The volume, Vol, can be expressed as a function of the triple (R, δ, θ) or the triple (a, δ, θ), resulting in:

$$\mathrm{Vol}(R,\delta,\theta) = 2\pi\left\{\frac{\delta}{2}(R^2 - 2rR + 2r^2)\frac{1}{3}\left(\frac{\delta}{2}\right)^3 + (R-r)r^2\left(\theta - \frac{\pi}{2} + \frac{\sin 2\theta - \pi}{2}\right)\right\} \tag{3.41}$$

$$\mathrm{Vol}(a,\delta,\theta) = \pi a^2\delta + 2\pi\left(\frac{\delta}{2\cos\theta}\right)^2\left\{a f_1(\theta) + \frac{\delta}{2}f_2(\theta)\right\} \tag{3.42}$$

$$f_1(\theta) = \theta - \frac{\pi}{2} + \frac{\sin(2\theta - \pi)}{2} + 2\sin\theta\cos\theta \tag{3.43}$$

$$f_2(\theta) = \tan\theta\left(\theta - \frac{\pi}{2} + \frac{\sin(2\theta-\pi)}{2} + 2\cos\theta\right) - \frac{\cos\theta^2}{3} + (1-\sin\theta)^2 \tag{3.44}$$

As equations (3.41) and (3.42) suggest, this description brings to complicated expressions to solve analytically[6]. Indeed, the development of complete and general **theoretical** model for a faithful description of these real drops has not been fully developed in literature yet. Droplets

[6]For example, one may use the conservation of the volume, $\mathrm{Vol}(R_{initial}, \delta, \theta) = \mathrm{Vol}(R_{final}, \delta, \theta)$ to get an

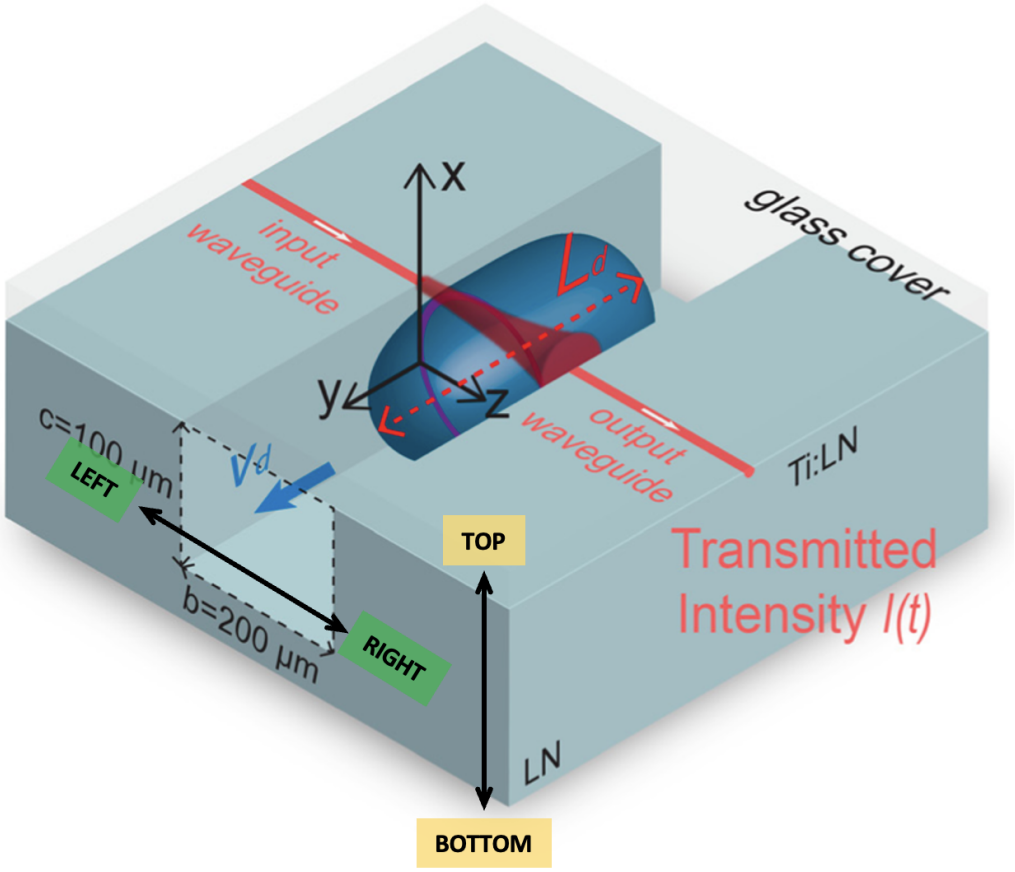

Figure 3.21: A real drop flowing in the rectangular microchannel. Adapted from [61].

base length is almost constant for fixed ϕ[7]: in the case $\phi = 0.8$, it varies between (561 ± 4) μm and (566 ± 7) μm, for $\phi = 0.6$ it is included between (467 ± 3) μm and (488 ± 4) μm while with $\phi = 1.0$ it ranges between (638 ± 4) μm and (641 ± 4) μm.

explicit expression for R_{final}. The final length of the droplet would be then $L_f = 2R_{final}$. Given the clear complexity of (3.41), this is indeed too difficult from a mathematical point of view.

[7]The drop velocity can be assumed to be constant, too.

3.6 Comparison: theory *versus* experiment

By comparing experimental evidence with the results of the models we have presented, we aim at verifying mainly if, and if yes to what extent, these analytical models are suitable to describe real systems that are characterized by a significantly greater level of complexity. A a spontaneous consequence of the comparison process is the enhancement of limits or criticalities of the models, provided that there are no errors in the experimental results, which is assumed hereafter. The approach aims to pave the way for the development of more complicated, possibly analytical models and is therefore based on phenomenology.

The theoretical model

The starting point under study is the shape of the drop. In chapter 2 a lot of cases have been treated; shapes have be assumed to be spherical (most cases), cylindrical (one case) or ellipsoidal (two cases). Spherical models can be immediately rejected, since it is obvious that a sphere is as far as it can go from the shape of the real droplets flowing in the channel and interacting with the photoinduced field. The cylinder and the first case for an ellipsoidal cross section are then considered, since they seem more appropriate. We summarize here again their main analytical results (see section 2.7):

NOTATION AND PARAMETERS

- μ, viscosity;
- γ, surface tension at the interface of the two fluids;
- σ, electric conductivity
- ϵ, electric permittivity
- E_∞, intensity of the external applied field;
- r_0, initial characteristic length of the drop (unbounded case);
- parameters (subscript i for "inner" fluid, whereas o for the "outer" one):

$$R = \frac{\sigma_i}{\sigma_o} \quad , \quad S = \frac{\epsilon_i}{\epsilon_o} \quad , \quad \eta = \frac{\mu_i}{\mu_o} \quad \text{and} \quad Ca_{el} = \frac{\epsilon_o E_\infty^2 r_0}{\gamma}.$$

Cylinder, circular cross section

The steady state is approached as:

$$\mathcal{D}(t) = \mathcal{D}_\infty(1 - e^{-t/\tau_\mathcal{D}}).$$

The steady state value deformation is:

$$\mathcal{D}_{T,\infty} = \frac{Ca_{el}}{3}\frac{\Psi}{(1+R)^2},$$

where $\Psi = R^2 + R + 1 - 3S$ and

$$\tau_\mathcal{D} = (\mu_i + \mu_o)r_0/\gamma$$

Ellipsoidal cross section

$$\mathcal{D}(t) = \mathcal{D}_\infty(1 - e^{-t/\tau_\mathcal{D}}).$$

The steady state value deformation is:

$$\mathcal{D}_\infty = \frac{9}{16}Ca_{el}F^\star(R,S,\eta),$$

and

$$\tau_\mathcal{D} = \frac{\mu_o r_0}{\gamma}\left(\frac{(3+2\eta)(16+19\eta)}{40(1+\eta)}\right)$$

with $F^\star(R, S, \eta)$ given by equation (2.108).

It is interesting to observe that:

- For both the circular and the ellipsoidal cross sections, $\mathcal{D}_\infty$ depends on Ca_{el};
- the parameter η can be found in the elliptical cross section case, affecting both $\mathcal{D}_\infty$ and $\tau_\mathcal{D}$ through a structural parameter $F^\star(R, S, \eta)$;
- in the case of the circular cross section, η enters can be emphasized in the expression for $\tau_\mathcal{D}$ but not in the one of $\mathcal{D}_\infty$, that does not contain it.

To provide a numerical estimate for the physical quantities under study, namely $\mathcal{D}$ and $\tau_\mathcal{D}$, we need to specify the numerical values of the parameters.

- the viscosity[8]: $\mu_i = 0.89$ cP and $mu_o = 3.04$ cP;
- the surface tension at the interface of the two fluids: $\gamma_0 = 4.27 \pm 0.04$ mN/m;
- the electric conductivity: $\sigma_i = 0.055$ μS/ cm and $\sigma_o = 1 \cdot 10^4$ pS/ cm
- the electric permittivity (relative values): $\epsilon_i = 80$ and $\epsilon_o = 2.05$.

As for both E_∞, the intensity of the external applied field and r_0, the initial characteristic length of the drop (in the unbounded case), we do not have a ready to use value. In fact, the first would be the estimate of the external imposed field inside the microchannel that is felt by the drop. In the case of pure LN, the space-charge field can span from 0 to $10^4 - 10^5$ V/m, while it is significantly increased in Fe:LN crystals, with values up to $10 \cdot 10^6$ V/m (with 0.1 % Fe concentration) [44]. We have performed a simulation to get an estimate of $\sim 8.3 \cdot 10^{-4}$ V/m at more or less 200 μm from the glass cover, which is then used as a rough estimate of E_∞.

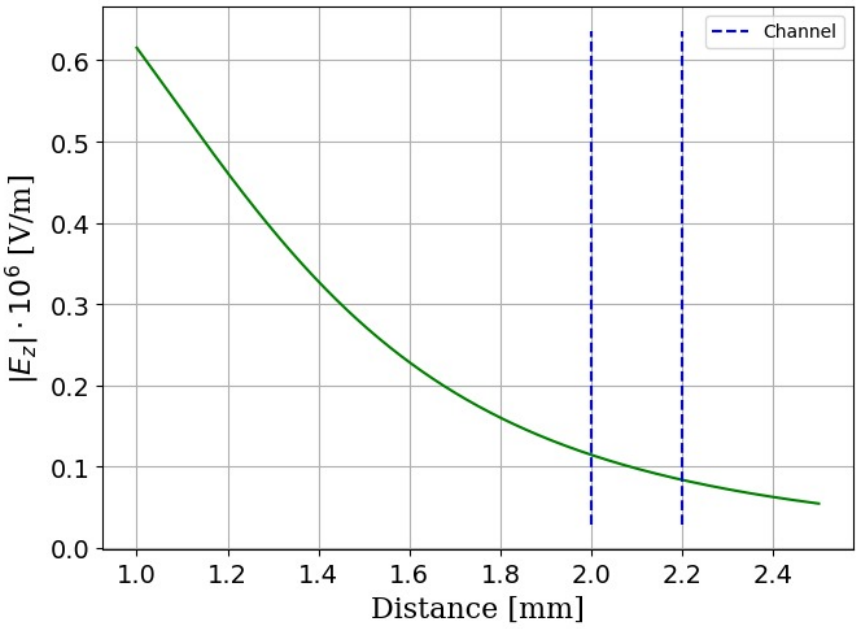

Figure 3.22: Value of the field plotted with respect to the top of the Fe:LN crystal.

[8]The viscosity is expressed here in centipoise, 1 cP = 1 mPa · s.

The value of r_0, the initial characteristic length of the cross section of the drop, is assumed[9] to be 50μm, since it is the maximum possible value for a circle that can be inscribed in the rectangular channel. We provide a numerical estimate of $\mathcal{D}_\infty$ and τ for both models:

Cylinder	**Ellipsoid**
The steady state value deformation is:	The steady state value deformation is:
$\mathcal{D} \sim 10^{-6}$ (3.45)	$\mathcal{D}_\infty \sim 2 \cdot 10^{-6}$, (3.47)
$\tau \sim 0.065$ms (3.46)	$\tau \sim 0.046$ms (3.48)

$\mathcal{D}$, as defined in chapter 1, is a dimensionless parameter telling us that for both models the deformation is small:

$$(r_\parallel - r_\perp) \sim (r_\parallel + r_\perp) \cdot 10^{-6} \tag{3.49}$$
$$(r_\parallel - r_\perp) \sim 2 \cdot (r_\parallel + r_\perp) \cdot 10^{-6}. \tag{3.50}$$

Parameter τ is the characteristic time for the deformation of the cross section. It is reasonable to expect that the drop will deform simultaneously both with respect to the cross section and the axial length, therefore τ can also be assumed to provide a timescale for axial deformation (in our case an elongation). In both estimates, the value of τ is consistent with the assumption that deformation has to be established before the drop is detected[10].

Real measurements

The majority of the existing of theoretical models does not assume or impose the conservation of volume, namely $\text{Vol}_{initial} = \text{Vol}_{final}$; the latter is however a crucial assumption, turning the model from a mathematical one to a physical one. Let us analyze the consequences of the conservation of volume in much detail.

- Cylinder, circular cross section[11]:

$$\text{Vol}_{initial} = \pi r_0^2 L_0, \tag{3.51}$$
$$\text{Vol}_{final} = \pi a b L_f; \tag{3.52}$$

  conservation of volume reads:

$$r_0^2 L_0 = a b L_f. \tag{3.53}$$

  It is straightforward to obtain therefore

$$r_0 = \sqrt{\frac{L_f}{L_0} a b} \tag{3.54}$$

- For a cylinder with elliptic cross section[12]: the same reasoning leads to:

$$a_{in} b_{in} L_0 = a_{fin} b_{fin} L_f \tag{3.55}$$

  Note that if the shape would be a three-dimensional ellipsoid, the standard formula for its volume, $\frac{4}{3}\pi abc$, where $c_{in} = \frac{L_0}{2}$ and $c_{fin} = \frac{L_f}{2}$ in the conservation equation would lead to the exact same result of the cylinder with elliptic cross section.

[9] In fact, our real drop is not a cylinder.
[10] This sets an upper boundary for the value of the characteristic time, $4\tau < 0.16$s.
[11] The circular cross section deforms into an ellipsoid with semiaxes (a, b). See figure 2.1.
[12] That is, the already-ellipsoidal cross section deforms into another ellipsoid with new semiaxes.

Some remarkable comments can already be made from this reasoning. In fact, if the volume is conserved and if L_f is different from L_0 (in our case, drop elongates so $L_f > L_0$), then also the cross section has to modify during the process.

Last but certainly not least, we have assumed generally that γ, the surface tension at the interface of the two fluids is constant. This might be not true, as we observed in our real system.
In **Figure 3.23**, as an example, the average behavior over time of final lengths is reported for the case $Q_c = 10\ \frac{\mu L}{\text{min}}$ and $Q_d = 8\ \frac{\mu L}{\text{min}}$ ($\phi = 0.8$). Each point is the average of the final lengths of at least 100 detected droplets. The fit is performed with the following equation:

$$L_f(t) = L_0 + \Delta L \left(1 - e^{-t/\tau}\right) \tag{3.56}$$

where L_0 is the fixed base length obtained when no laser beam is impinging on the iron-doped sample while ΔL and τ are the fitting parameters, respectively the observed elongation due to illumination and the typical time in which that elongation is established.

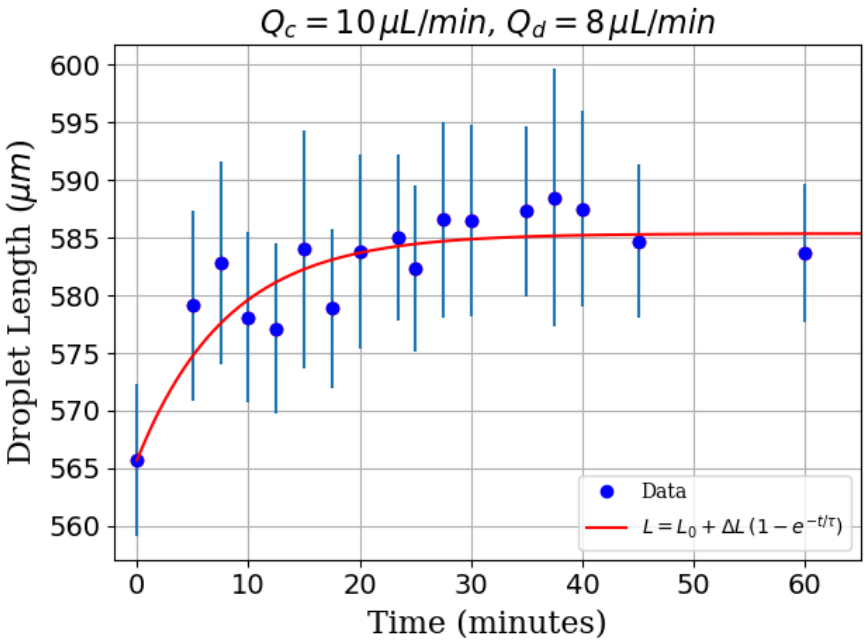

Figure 3.23: Average lengths over time with flow rates $Q_c = 10\ \frac{\mu L}{\text{min}}$ and $Q_d = 8\ \frac{\mu L}{\text{min}}$ ($\phi = 0.8$). In this case, a Fe:LN sample with $N_{Fe^{3+}} = 15.6 \cdot 10^{18}$ atoms/cm^3 is employed.

As already mentioned, the induced elongation of the droplet is due to the Photo-Voltaic effect by way of the interaction of the space-charge field generated in Fe:LN. Our experimental apparatus actually measures the two steady states for each drop. If all the drops were always under the same experimental conditions, we would be dealing with repeated measurements of the same phenomenon. In this perspective, we would expect that, for fixed flow rate $\phi := Q_d/Q_c$:

1. droplets base length L_0 is almost constant, which is true;

2. the values recorded for subsequent final lengths L_f of the droplets are all settling around the same value. It is clear from **Figure 3.23** that this is not true: as time passes, drops elongate more, reaching higher values of L_f.

The fact that the average final lengths are increasing over time reaching a saturation value is witnessing a novel kind of interaction yet to be properly understood.
Not accounting for this change in a theoretical model may be an additional, possible source of discrepancy.

Results of the comparison

All in all, we can conclude that conservation of volume leads to the possibility of expanding theoretical treatment to include the possibility of deformation in the axial direction.
In fact, evidence is that theoretical models work on cross sections, providing insights on their dynamical evolution and estimates of both their deformation rates and characteristic times. This is possible under some specific assumptions of geometric symmetry (e. g. for a cylinder symmetry in the direction of its axis is assumed) and generally reduces the problem to a two-dimensional one as we have previously seen. This is an approximation as it ignores the possibility of growth of random perturbations in the axial direction (which exist in an actual setting). The latter is confirmed also from another fact that has been neglected until this point: field nonuniformity.
Both models suppose the application of a uniform field, that justifies the further assumption of symmetry with respect to the axis of the cylinder, allowing therefore the equations to become two-dimensional. But it is clear that, if the field is nonuniform, this is in general not true and some changes need to be introduced in order to account for this aspect. We will deal with the latter in the next section, providing a novel proposal for the case of the cylinder.
Finally, it is in general not possible to consider γ as a constant.

3.7 Model improvements

In light of the limitations emerged as a result of the theory-experiment comparison, we present here three elements that, if included in the model, may be crucial for its improvement: the confinement, the field nonuniformity and the temporal variation of the surface tension value.
It is reasonably to expect that the more of these three points would be included in an extension of an electrohydrodynamic model, the better the improvement (an ideal condition would be their contemporaneous presence).

Confinement

The first one, that is the **confinement** of the outer fluid in which droplets are suspended has already been addressed by several numerical studies. However, an *analytical* development of EHD theory taking into account the presence of walls is yet to be performed in detail. This is reasonable, since its addition might bring a non-negligible contribution of complexity to the problem up to a point where it could be directly considered as guilty in case of an eventual failure of analytical solution.
In this regard, trying to overcome the latter two new ideas can be carried on:

1. since, as said, the effect of the confinement on large drops results in modifications of the three-dimensional shape of the surface of the drop, one may choose to perform some target modifications to already-existing shapes accounting for the "constrained" deformations and providing thus a shape that is closer to reality. The aim would be to stick to these shapes that can bring to analytical solutions (cylinder or ellipsoid) by opportunely combining them together or by adding some specific analytical conditions to include confinement.

From a simpler viewpoint, it may be possible to start simply by improving the shape of the drop, from a cylinder to an ellipsoid, which is surely closer to the shape of large drop flowing in channels and has jet not been extensively treated in literature.

2. by exploiting the conservation of the volume, one may think to invert one among equations (3.41) and (3.42) to get an expression for R or a in terms of the volume and the contact angles. Measurements of the values of contact angles both with and without electric field may then lead to relevant results in terms of elongation and electrohydrodynamic response. Note that exact results presented in subsection 3.5.2 are derived in a simpler case which may be enlarged to the one of non-symmetric contact angles and both confinements. Again, this proposal is valid only in the case of large drops.

Extension of the model for a leaky cylinder in nonuniform E

As we have seen, the application of a uniform field justifies the further assumption of symmetry with respect to the axis of the cylinder, allowing therefore the equations to become two-dimensional. But it is clear that if the field is not uniform, this is generally not true and a few changes need to be made to take this into account.

The general solution for the Laplace's equation (1.23) in cylindrical coordinates assuming cylindrical symmetry is:

$$V(r,\theta) = A_0 \ln r + B_0 + \sum_{k=1}^{\infty} \left\{ r^k [A_k \cos k\theta + B_k \sin k\theta] + r^{-k} [C_k \cos k\theta + D_k \sin k\theta] \right\} \quad (3.57)$$

that can be expanded according to one's need. It is actually simple to verify (see **Appendix A**) that for the first order with boundary conditions expressed in section 2.5, one regains results of equations (2.75) and (2.76).

To impose a condition for a nonuniform potential, it may be sufficient to expand the potential up to the second order:

$$V^{(2)}(r,\theta) = A_0 \ln r + B_0 + r[A_1 \cos\theta + B_1 \sin\theta] + \frac{[C_1 \cos\theta + D_1 \sin\theta]}{r} + \\ + r^2 [A_2 \cos 2\theta + B_2 \sin 2\theta] + \frac{[C_2 \cos 2\theta + D_2 \sin 2\theta]}{r^2}.$$

Now we have to go on by imposing boundary conditions, that are taken as:

(i) $V_i = V_o$ at $r = r_0$;

(ii) V_i is bounded at $r = 0$;

(iii) $\epsilon_0 \epsilon_o \dfrac{\partial V_o}{\partial r} = \epsilon_0 \epsilon_i \dfrac{\partial V_i}{\partial r}$ at $r = r_0$;

(iv) $V_o = E_\infty [r P_1(\cos\theta) + \Lambda r^2 P_2(\cos\theta)]$ as $r \to \infty$.

The latter is due to the fact that we have to take into account the field nonuniformity, and Feng's potential is one of the few – if not the only one – proposals to treat such cases.

Boundary conditions $(i) - (iii)$ are the same that have been imposed in all this thesis work, so the main point is imposing (iv), which has crucial consequences that we analyze in detail in

the following.
Let us start from:

$$V_o = E_\infty[rP_1(\cos\theta) + \Lambda r^2 P_2(\cos\theta)] = -E_\infty\left[r\cos\theta + \Lambda r^2\frac{(3\cos^2\theta - 1)}{2}\right] \tag{3.58}$$

since $1 = \cos^2\theta + \sin^2\theta$ the latter results in:

$$V_o = E_\infty\left[r\cos\theta + \Lambda r^2\left(\cos^2\theta - \frac{\sin^2\theta}{2}\right)\right]. \tag{3.59}$$

Now let us address the complete expression for the potential: since no $\sin\theta$ appear in the b.c., we can safely set[13] $B_1 = B_2 = D_1 = D_2 = 0$, giving then:

$$V^{(2)}(r,\theta) = A_0\ln r + B_0 + rA_1\cos\theta + \frac{C_1\cos\theta}{r} + r^2A_2\cos 2\theta + \frac{C_2\cos 2\theta}{r^2}. \tag{3.60}$$

in which we substitute $\cos 2\theta = (\cos^2\theta - \sin^2\theta)$ and rearrange:

$$V^{(2)}(r,\theta) = A_0\ln r + B_0 + rA_1\cos\theta + \frac{C_1\cos\theta}{r} + r^2A_2(\cos^2\theta - \sin^2\theta) + \frac{C_2}{r^2}(\cos^2\theta - \sin^2\theta). \tag{3.61}$$

Application of b.c. (iv) to (3.61) yields:

- $A_0^o = 0$, since there is no explicit logarithmic dependence;
- $B_0^o = 0$, since there is no constant term in the far field;
- $A_1^o = E_\infty$;
- C_1^o and C_1^o need to be constant to ensure that $\sim 1/r$ and $\sim 1/r^2$ terms go safely to zero in the far field.

We are then left with

$$r^2A_2^o(\cos^2\theta - \sin^2\theta)$$

that we have to put equal to

$$r^2E_\infty\Lambda\left(\cos^2\theta - \frac{\sin^2\theta}{2}\right).$$

This leads to an absurd, since it would imply that:

$$A_2^o = E_\infty\Lambda = \frac{E_\infty\Lambda}{2}. \tag{3.62}$$

Even relaxing the (iv) boundary condition, i.e. requiring that:

$$V_o \sim E_\infty[r\cos\theta + \Lambda r^2\cos^2\theta] \tag{3.63}$$

[13] Since $\sin 2\theta = 2\sin\theta\cos\theta$, terms containing $\sin 2\theta$ have to go to zero, too.

as $r \to \infty$, leads to an inconsistent result: it would require to put terms with $\sin^2\theta$ to zero in the far field. However, the latter is possible only if $A_2^o = 0$, putting to zero also the $\cos^2\theta$ that, on the contrary, is necessary to impose the relaxed condition (3.63).

To solve this inconsistency, another possibility would be to impose "manually" the missing terms to get the b.c. by searching for a correction, $\mathcal{C}$:

$$r^2 A_2^o(\cos^2\theta - \sin^2\theta) + \mathcal{C} = r^2 E_\infty \Lambda \left(\cos^2\theta - \frac{\sin^2\theta}{2}\right). \tag{3.64}$$

That leads to:

$$\mathcal{C} = \cos^2\theta(1 - A_2^o) - \sin^2\theta\left(\frac{1}{2} - A_2^o\right) \tag{3.65}$$

in which A_2^o is undetermined (to go on, one would have to impose a value for it: this is no sense since we are actually searching for it).
The inconsistency comes from both the fact that we are assuming cylindrical symmetry ($\partial/\partial z = 0$), true only for an uniform field and that we are imposing a nonuniform far field condition that is valid for a spherical coordinate system.

It is then necessary to solve the Laplace's equation in cylindrical coordinates in the generic case and hopefully to propose a novel far field condition for the outer potential in terms of the generalized solution. According to this new idea, the *general* solution of Laplace's equation in cylindrical coordinates has to be considered to go on.

The general Laplace's equation is

$$\nabla^2 V = 0 \tag{3.66}$$

that in cylindrical coordinates reads:

$$\frac{\partial^2 V}{\partial r^2} + \frac{1}{r^2}\frac{\partial^2 V}{\partial \theta^2} + \frac{\partial^2 V}{\partial z^2} = 0 \tag{3.67}$$

where V is the electric potential that now is a function of r, θ and z. By postulating that the solution can be expressed using separation of variables, that is:

$$V(r,\theta,z) = R(r)T(\theta)Z(z) \tag{3.68}$$

an intermediate result can be found (omitting dependencies to facilitate notation):

$$TZ\frac{\mathrm{d}^2 R}{\mathrm{d}r^2} + \frac{TZ}{r}\frac{\mathrm{d}R}{\mathrm{d}r} + \frac{RZ}{r^2}\frac{\mathrm{d}^2 T}{\mathrm{d}\theta^2} + RT\frac{\mathrm{d}^2 Z}{\mathrm{d}z^2} = 0. \tag{3.69}$$

Equation (1.2) can be divided by RTZ and rearranged to get:

$$\frac{1}{R}\frac{\mathrm{d}^2 R}{\mathrm{d}r^2} + \frac{1}{rR}\frac{\mathrm{d}R}{\mathrm{d}r} + \frac{1}{r^2 T}\frac{\mathrm{d}^2 T}{\mathrm{d}\theta^2} = -\frac{1}{Z}\frac{\mathrm{d}^2 Z}{\mathrm{d}z^2} \tag{3.70}$$

which has the advantage of having the (r,θ) dependence separated from the z one.

Standard methods have been developed to solve (3.67) on the basis of (1.2) and (3.70) [62]:

$$\begin{aligned} V(r,\theta,z) = &\sum_{\lambda,m}\{J_m(\lambda r), N_m(\lambda r)\}\{\sin(m\theta), \cos(m\theta)\}\{\sinh(mz), \cosh(mz)\} + \\ &+ \sum_{(\lambda,m)}\{I_m(\lambda r), K_m(\lambda r)\}\{\sin(m\theta), \cos(m\theta)\}\{\sin(mz), \cos(mz)\}. \end{aligned}$$

where J_m, N_m, I_m and K_m are, respectively Bessel and Neumann functions of order m and the modified Bessel functions [62]. Moreover, {[...],[...]} denotes the linear combination of the therms inside the brackets.

The obtained result is complex, and a new proposal for a field has to be carefully chosen in order to be consistent not only with mathematics[14] but mainly with the physical aspects of the problem.

Surface tension: phenomenology of a new interaction

A reasonable assumption to justify the observed increasing trend of final lengths may be a temporal variation (actually, a decrease) of the water-hexadecane surface tension γ: for the electric field it is easier to elongate a drop with a lower surface tension. In the following, we try to explain this unexpected phenomena.

From table 3.3 data it clearly emerges a droplet elongation of 2-3 %, which suggests doubtlessly the impact of photovoltaic induced effects since the deformation follows eq. 3.56.

R	$N_{Fe^{3+}}$ ($\frac{\text{atoms}}{\text{cm}^3}$)	$\Delta L/L_0$ (%)	τ (minutes)
0.100 ± 0.006	$(17.0 \pm 0.3) \cdot 10^{18}$	3.2 ± 0.2	11 ± 3
0.205 ± 0.007	$(15.6 \pm 0.2) \cdot 10^{18}$	3.4 ± 0.2	8 ± 2
0.270 ± 0.007	$(14.8 \pm 0.2) \cdot 10^{18}$	2.3 ± 0.7	20 ± 13

Table 3.3: Fit parameters of eq. 3.56 with flow rates $Q_c = 10\ \frac{\mu L}{\text{min}}$ and $Q_d = 8\ \frac{\mu L}{\text{min}}$ ($\phi = 0.8$) and density of acceptors of the three employed Fe:LN samples.

If the droplets elongation were due to the photo-induced field, we would expect that $\Delta L/L_0$ values would follow an increasing trend (Equation 3.30). The data in table 3.3 displays indeed an increasing trend with $0.100 \leq R \leq 0.270$.
Some hypothesis have been formulated to explain this experimental evidence:

1) $N_{Fe^{3+}}$ investigated range is not wide enough, hence our system has not enough resolution to measure a trend;

2) it may be sufficient that $E_{sc} \geq E_{threshold}$ ("threshold effect") for an elongation to take place. In this specific case, the above inequality would be verified for each of the three Fe:LN samples;

3) the elongation may be due to a "gradient effect". It is reasonable to assume that droplets' elongation is directly caused by the dielectrophoretic force F_{dep}, in turn due to the spatial variation of the photo-induced electric field:

$$F_{dep} \propto \nabla |E(t)|^2$$

Since the single droplet is elongating only in the illuminated zone of the channel and returning to its "standard" dimension (L_0) after traveling through the field lines, it is expected to display a sort of spring-like behavior, with

$$F_{dep} \approx k\Delta L(t) \approx \gamma \Delta L(t) \tag{3.71}$$

[14]For example, one may exploit the properties of Bessel and Neumann functions. In fact, since K_m and N_m diverge at $r = 0$ they should be excluded from problems where the region of interest includes the origin; similarly, both J_m and I_m diverge as $r \to \infty$ and will therefore be excluded from any exterior solution.

because of dimensional arguments.

In this work it is clear that, for all the employed samples, $E_{sc} \geq E_{threshold}$ holds and hypothesis 1) does not exclude 3).

Let us discuss the time scale of the phenomenon we are investigating, starting from hypothesis 3. The latter implies that the typical time τ of the observed elongation must be the same of the photo-induced field, namely $\tau = \tau_{sc}$, assuming that the time dependencies appear exclusively in $E(t)$ and $L(t)$. On the other hand, τ_{sc} depends only on the characteristics of the Fe:LN sample and on the illumination intensity (eq. 3.29): considering $R = 0.205$, $\tau_{sc} \approx 17$ seconds since $I \approx 2.2 \cdot 10^4$ W / m^2 while $\varepsilon = \varepsilon_{11} = \varepsilon_{22} = 84$ [26] because the chosen geometry is such that light impinging on the sample is polarized on the xy plane.
As shown in table 3.3, the experimental τ values are one order of magnitude bigger than τ_{sc} which means that the observed phenomenon is much slower than the building up of the photo-induced field. When $t = 4\tau$ it must be $E(t) \approx E_{phv}$ and therefore all the $L(t_i)$ values for $t_i > 0$ in figure 3.23 (and in this work) are obtained when the field has already reached its saturation value E_{phv}.

As a further consequence, in eq. 3.71, F_{dep} has no more temporal dependence and the same must hold for the right-hand side, $\gamma \Delta L(t)$. If $L(t)$ follows the experimentally observed trend $L(t) \propto (1 - e^{-t/\tau})$ then the only way to cancel out the time dependence would be to have γ decreasing over time as $\gamma(t) \propto (1 - e^{-t/\tau})^{-1}$.

In this thesis we propose a way to obtain the time variation of γ over time accounting also the effect of droplets velocity.

In a T-junction, the dimensions of droplets are predicted by equation 3.72, where the capillary number Ca contains viscosity of continuous phase μ_o and surface tension between the two phases, γ.

$$L = (\varepsilon + \omega\phi)\, Ca^{-m} \tag{3.72}$$

where $Ca = \mu_o\, u/\gamma$ is the capillary number, μ_c is the viscosity of the continuous phase, v is droplets velocity, γ the surface tension between the two phases, ε, ω, m are (in principle) geometry-dependent parameters and $\phi = Q_d/Q_c$. Therefore, once the two phases have been chosen, it is possible to vary droplets length (and velocity) by properly changing the flow rates. All the chosen flow rates' combination are reported in table 3.4. Non-polar liquids viscosity is not subjected to appreciable variation in presence of electric fields up to 10^5 V/m [63; 64], hence μ_c can be considered constant during the PhV illumination. This in turn further suggests that γ plays a crucial role in this kind of dynamics.

In particular, by rewriting eq. 3.72 as

$$L = A(\phi)\, Ca^{-m} = A(\phi)\, \left(\frac{\mu\, v}{\gamma}\right)^{-m} \tag{3.73}$$

since γ and μ_c are known when no electric field is applied, it is possible to estimate $A(\phi)$ and m at zero electric field by fixing ϕ and fitting L_0 as a function of Ca with $A(\phi)$ and m as free parameters by using eq. 3.72.
We obtain $A(\phi) = 520 \pm 20$ μm and $m = m_0 = 0.015 \pm 0.007$ (figure 3.24). Assuming that these values holds also when $E_{phv} \neq 0$, we fitted $L(t_i)$ as a function of v with eq. 3.73 for each set of acquisitions at different times, namely with $t_i = 5, 10, 15, 20, 25, 30, 35, 40$ minutes. However, the optimal parameter fits fails in appropriately describe the trend of $L(t_i)$ as shown in figure

$\phi = Q_d/Q_c$	Q_c ($\frac{\mu L}{\text{min}}$)	Q_d ($\frac{\mu L}{\text{min}}$)	L_0 (μm)	v_0 (μm /ms)
0.8	10	8	566 ± 7	6.29 ± 0.03
	11	8.8	566 ± 6	6.97 ± 0.04
	12.5	10	561 ± 4	8.03 ± 0.02
	15	12	563 ± 5	9.49 ± 0.07
	16.25	13	562 ± 6	10.44 ± 0.03
	17.5	14	561 ± 4	11.29 ± 0.05
	20	16	569 ± 4	13.59 ± 0.06
0.6	12	7.2	488 ± 4	7.02 ± 0.02
	16.5	9.9	476 ± 3	9.56 ± 0.03
	23.5	14.1	467 ± 7	13.65 ± 0.06
1.0	9	9	639 ± 6	6.31 ± 0.03
	13.4	13.4	638 ± 4	9.47 ± 0.04
	19	19	641 ± 4	13.6 ± 0.04

Table 3.4: List of all the flow rates' combinations in this work. The standard deviation σ_Q associated to each flow rate value is $\sigma_Q = 0.2\ \frac{\mu L}{\text{min}}$. Base lengths L_0 and velocities v_0 are obtained from the acquisition at time $t = 0$ min. before switching on the PhV illumination averaging over more than 100 droplets.

3.25.

Therefore, to relax the hypothesis on the parameters $A(\phi)$ and m, we fitted again $L(t_i)$ as a function of v letting the exponent m to be a fitting parameter together with γ. The fits at $t_i = 10, 20, 30$ minutes are reported as an example in figure 3.26 and in this case the experimental data trend is well reproduced. Each performed fit at $t = t_i$ yields the values $\gamma(t_i)$ and $m(t_i)$. The time behavior of $\gamma(t)$ and exponent $m(t)$ are reported in figures 3.27 and 3.28 respectively. Surface tension displays a decreasing trend over time as expected while exponent m is instead increasing with a behavior similar to the $L(t)$ time-dynamics. It is possible to fit $\gamma(t_i)$ values with the following function:

$$\gamma(t) = \frac{\alpha}{\frac{1}{\gamma_0} + \beta(1 - e^{-t/\tau_\gamma})} = \frac{\alpha\gamma_0}{1 + \beta\gamma_0(1 - e^{-t/\tau_\gamma})} \tag{3.74}$$

obtaining $\alpha = 1.000 \pm 0.006$, $\beta = (6.4 \pm 0.6) \cdot 10^3$ m/N, $\tau_\gamma = 10 \pm 2$ minutes and it is immediate to notice that τ_γ and τ are of the same order of magnitude.

It is also evident, despite the matching of the time scales, how in eq. 3.71 the canceling out of the time dependence is not achieved. This however can suggest to revise (3.74) or to consider the contribution due to the electric field connected to the droplets motion through the field lines, that we are not taking into account here.

Nevertheless, another argument can be used to support the decreasing trend of the surface tension. In the spring-like behavior hypothesis (hypothesis 3), if we assume pure elastic behavior of the interface Hexadecane-Water we can introduce an effective Young modulus E^* and we can write:

$$\gamma \approx k = \frac{E^* \cdot S}{L}$$

where S is the droplet section. It is clear that is $L = L(t)$, then:

$$\gamma = \frac{E^* \cdot S}{L(t)} = \frac{E^* \cdot S}{L_0 + \Delta L\,(1 - e^{-t/\tau})}$$

which allows to recover the shape of equation 3.74.

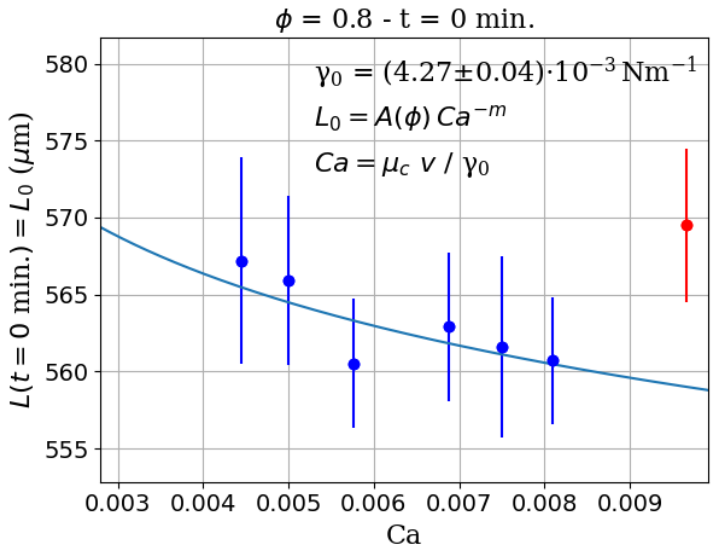

Figure 3.24

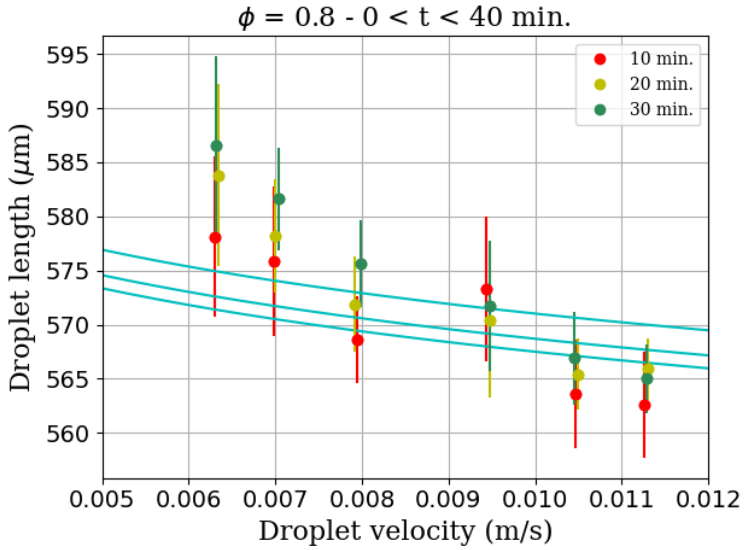

Figure 3.25

In 3.24, fit of experimental data with equation 3.73. The free parameters are $A(\phi)$ and m. The red point on the left, corresponding to the combination of flow rates $Q_c = 20\ \frac{\mu L}{\text{min}}$, $Q_d = 16\ \frac{\mu L}{\text{min}}$, has been excluded from the fitting procedure. In 3.25, three examples of fits of $L(t_i)$ as a function of v with eq. 3.73 with $t_i = 10, 20, 30$ minutes, by employing $A(\phi)$ and m parameters obtained from the fit with eq. 3.73. Optimal parameters fits fail in properly describing the trend of $L(t_i)$.

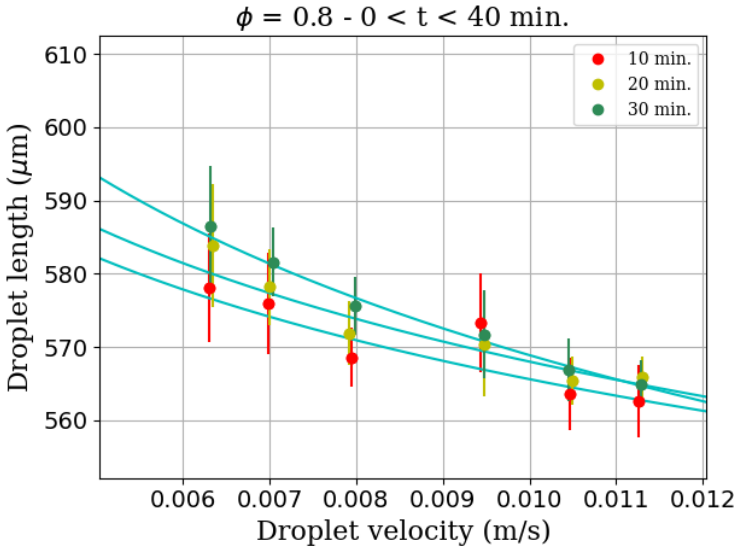

Figure 3.26

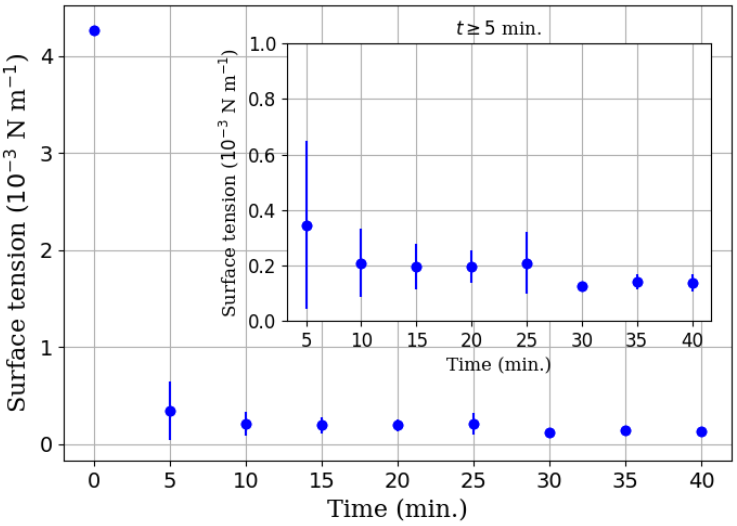

Figure 3.27

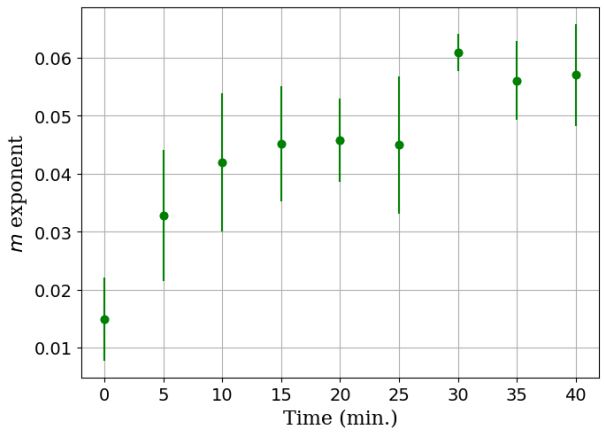

Figure 3.28

In fig. 3.27 surface tension values obtained from all the fits. The point at t = 0 min. is an experimental value obtained with the pendant drop method: $\gamma_0 = 4.27 \pm 0.04$ mN/m. In fig. 3.28 the correspondent m values.
In figure 3.26 three examples of fits of $L(t_i)$ as a function of v with eq. 3.73 with t_i = 10, 20, 30 minutes, by employing $A(\phi)$ parameter obtained from the fit with eq. 3.73 with $0.004 \leq Ca \leq 0.009$, with γ and m as fit parameters.

The modification over time of $\gamma(t)$, a property connected to the interface between the two phases, may be due to the presence of the electric field and its action on SPAN® 80 surfactant dispersed in the continuous phase.
These promising results pave the way for studies on interfacial rehology of these interfaces and future improvement of EHD. In fact:

- These theoretical considerations enter the paradigm of electrically stressed water drops, a field that has yet to be explored in detail. As said, in this perspective the droplet may be displaying a sort of spring-like behavior that has not been reported yet:

  $$F_{DEP} \approx k\Delta L(t) \approx \gamma \Delta L(t)$$

  because of dimensional arguments. Assuming pure elastic behavior of the interface, we have introduced a sort of effective Young modulus $E^\star$:

  $$\gamma \approx k = \frac{E^\star S}{L}$$

  with S being the droplet section. Consequently, γ would be inversely proportional to L.

- this has a great impact on the modifications that need to be done to the theoretical model. In fact, EHD predicts that $\tau_{\mathcal{D}}$ depends on γ; therefore a time dependence in γ would induces a time dependence in the characteristic time of the deformation of the droplet, $\tau_{\mathcal{D}}(t)$.

Conclusions

The aim of this thesis was to study the modeling of the response of water droplets in a generic time- and space-dependent electric field. Thus, Electrohydrostatics and electrohydrodynamic modeling are the broad context in which this this thesis work can be framed.

Theoretical modeling represent an important tool in many areas of scientific activity: both EHD and EHS modeling concern the interaction between the flow of fluid and the electric field. Their governing laws can be presented in a general way, since the differential equations into play come from Stokes equations coupled with Maxwell's equations. In principle, there is no need to refer to a specific, experimental setup addressing a particular problem. The starting point is generally the formulation of the problem, for which it is necessary to specify the appropriate coordinate system (Cartesian, spherical, cylindrical, ellipsoidal) that will be adopted. This decision will affect the whole derivation of the eventual analytic solution, since equations will be then written in these specific coordinates from the very early beginning. Obviously, such a choice depends on the shape of the drop and has to be suitable to describe the problem. In most cases is accompanied by some further assumptions (geometrical symmetries, discard of nonlinear effects, limited range for certain parameters), whose goal is to simplify even more the equations in order to increase the possibility of finding analytical solutions.

As a consequence, in the first place a general revise of the already-existing EHS and EHD works on droplets in an electric field was necessary: in a summary outline we presented the different, possible formulations of the problem, emphasizing that not all of them have been treated in literature. Indeed, the majority of the works focuses on spherical (circular if two-dimensional) drops, with just a few cases for a cylindrical shape and no extensive treatment has been for an ellipsoid yet[15].

As far as more complex situations are involved – and that is actually the case of almost all real systems – just a few (if any) attempts have been done to extend or at least examine the limitations of EHS/EHD theories to describe such problems. Therefore, we went on by proposing a novel comparison between these models and real data coming from measurements of the response of microfluidic water droplets to a time-varying, spatially nonuniform electric field of a particular system[16]. The comparison highlighted the need to extend existing theoretical models in order to pave the way for the development of new analytical models.

We have been able to identify some of the aspects that can be considered as sources of this inconsistency between theory and real data. In particular, choosing the EHD cylindrical case to mimic the shape of real droplets, we have witnessed that the model has some criticalities:

[15]Concerning the latter, two papers have dealt with two-dimensional elliptical shapes.

[16]The latter is based on a wide-ranging scientific project that has already developed several new methods of real-time detection and monitoring of micro and submicrometric objects dispersed in fluid media.

- the drop is considered as suspended (not moving) and immersed in an unbounded domain, which is never the case for a real system;
- the conservation of the volume is generally not imposed in the theory, making the model a **mathematical** but not a **physical** one;
- theoretical treatment works on cross-sections (2D) by assuming specific symmetries (since, for example, the electric field is taken as uniform); this is a problem especially when dealing with real fields, that are rarely uniform;
- the majority of the literature assumes that fluids have constant electric and physical properties; however, this may not be the case, as we have witnessed by observing an anomalous trend for the deformation of droplets: this suggested that γ, the surface tension between the two fluids may be varying during the process.

In this perspective, we also proposed some novel, phenomenological-based theoretical modeling to explain some of those incongruities:

- we proposed to treat the consequences of the confinement by means of the real volume of the droplet itself. By writing the volume as an analytical function of the "shape" parameters (e.g. the radii of curvature) of the real drop and imposing its conservation, one may invert the formula to get direct insight on the desired quantities;
- we showed for the first time that the only case of nonuniform potential, the one proposed by Feng [8], is valid **only** for the case of spherical drop. If the shape on the drop – and consequently the coordinate system – is not a sphere (or a 2D circular cross section), Laplace's equation has to be solved from scratch *without* assuming specific symmetries: this implies that also, a new external potential has to be imposed accordingly;
- as long as the surface tension is concerned, it was observed that the final length of subsequent drops grows over time. This enters the paradigm of electrically stressed water drops, a field that has yet to be explored in detail. A reasonable assumption to justify this increasing trend of final lengths was identified to be a temporal variation (actually, a decrease) of the water-hexadecane surface tension γ: for the electric field it is easier to elongate a drop with a lower surface tension. This partially shifts the problem to interfacial rheology: a model for this time-variation of the surface tension has being investigated and an equation for the temporal evolution of γ has been found. In this perspective, the droplet may be displaying a sort of spring-like behavior that has not been reported yet:

  $$F_{DEP} \approx k\Delta L(t) \approx \gamma \Delta L(t)$$

  because of dimensional arguments. Assuming pure elastic behavior of the interface, we may introduce a sort of effective Young modulus $E^\star$:

  $$\gamma \approx k = \frac{E^\star S}{L}$$

  with S being the droplet section.
  Consequently, γ would be inversely proportional to L.

Therefore, the thesis has paved the way for new features in the droplet response, presenting the first attempt in the literature to explain such a mixture of complicated phenomena.

Appendix A

The streamfunction formulation

Navier-Stokes equations for two-dimensional incompressible flows can be recast by using the streamfunction-vorticity formulation, that can be considered ad one of the first unsteady, incompressible Navier-Stokes algorithms.
Such formulation provides an alternative, simpler form for them in terms of two dependent variables, the streamfunction and the vorticity. In many cases, this formulation offers a deeper understanding of the physical mechanisms that drive the flow.

The streamfunction is defined as:

$$\psi_A(P) = \int_A^P \mathbf{u} \cdot \mathbf{n} ds \tag{3.75}$$

where A is an arbitrary but fixed point and $\mathbf{n}$ is the unit normal vector on the A-to-P line. $\psi_A(P)$ is a function of the location of the P point.

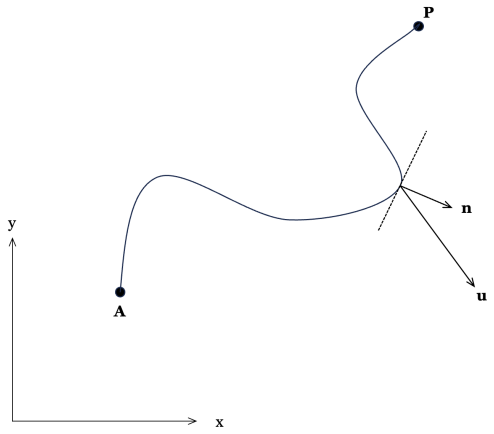

Figure 3.29

- From the image 3.29, it is clear that $\psi_A(P)$ represents the volume flux per unit depth in the $z-$direction through the line that goes from A to P;
- $\psi_A(P)$ does not depend on a specific path, that is its value only depends on the locations of points A and P;
- Commonly, the explicit dependence on point A is not indicated: $\psi_A(P) = \psi(P) = \psi(x, y)$, since a change in the position of A only modifies $\psi_A(P)$ by a constant value and such changes are irrelevant with respect to all applications;

- The name *streamlines* indicates those lines that are everywhere parallel and constant[17] to the velocity field, i.e. $\mathbf{u} \cdot \mathbf{n} = 0$;

ψ is connected to the Cartesian velocity components u and v through the following[18]:

$$u = \frac{\partial \psi}{\partial y} \quad \text{and} \quad v = -\frac{\partial \psi}{\partial x}. \tag{3.76}$$

If a specific flow is given *via* the streamfunction, it satisfies automatically the continuity equation:

$$\frac{\partial u}{\partial x} + \frac{\partial v}{\partial y} = \frac{\partial}{\partial x}\left(\frac{\partial \psi}{\partial y}\right) + \frac{\partial}{\partial y}\left(-\frac{\partial \psi}{\partial x}\right) = 0. \tag{3.77}$$

Lastly, one can define the vorticity vector $\omega := \nabla \times \mathbf{u}$; for two-dimensional velocity fields the $z-$component of the latter is nonzero, $\omega = (0\mathbf{e}_x, 0\mathbf{e}_y, \omega\mathbf{e}_z)$. In the latter

$$\omega = \frac{\partial v}{\partial x} - \frac{\partial u}{\partial y} \tag{3.78}$$

and by substituting equations of (3.76) it is straightforward to see that:

$$\omega = -\nabla^2 \psi \tag{3.79}$$

being ∇^2 the Laplacian operator in two dimensions.

As far as the Navier-Stokes equations are involved, one can show that the three-dimensional momentum equation can be written in terms of the vorticity becoming the *vorticity transport equation*:

$$\frac{D\omega}{Dt} = (\omega \cdot \nabla)\mathbf{u} + \nu \nabla^2 \omega \tag{3.80}$$

where D/Dt is the material derivative and ν is the kinematic viscosity. Equation (3.80) becomes simpler in the two-dim. case, since $(\omega \cdot \nabla) = 0$ and therefore:

$$\frac{D\omega}{Dt} = \nu \nabla^2 \omega. \tag{3.81}$$

Equations (3.81) and (3.79), together with (3.76) provide the streamfunction-vorticity formulation of the Navier-Stokes equations: it is made of only two partial differential equations for scalars ω and ψ.

Lastly, if the $R_e \sim 0$ limit is valid, then it is sufficient to solve[19] only one fourth-order partial differential equation, $\nabla^4 \psi = 0$, where

$$\nabla^4 = \frac{\partial^4}{\partial x^4} + 2\frac{\partial^4}{\partial x^2 \partial y^2} + \frac{\partial^4}{\partial y^4}$$

the latter is generally solved by specifying appropriate boundary conditions and exploiting separation of variables.

[17] Since the condition $\mathbf{u} \cdot \mathbf{n} = 0$ holds on stationary impermeable boundaries, ψ is also constant along those boundaries.

[18] This can be shown by invoking that integral incomprehensibility constraint for an infinitesimally small triangle.

[19] This can be proved by taking the curl of the Stokes equations.

Cylinder from first order expansion

The general solution for the Laplace's equation (1.23) in cylindrical coordinates assuming cylindrical symmetry is:

$$V(r,\theta) = A_0 \ln r + B_0 + \sum_{k=1}^{\infty} \left\{ r^k [A_k \cos k\theta + B_k \sin k\theta] + r^{-k} [C_k \cos k\theta + D_k \sin k\theta] \right\}. \quad (3.82)$$

In the case of an uniform potential, to solve Laplace's equation it is sufficient to expand the potential up to the first order:

$$V^{(1)}(r,\theta) = A_0 \ln r + B_0 + r[A_1 \cos\theta + B_1 \sin\theta] + \frac{[C_1 \cos\theta + D_1 \sin\theta]}{r}. \quad (3.83)$$

The problem assumes cylindrical symmetry, so it is a two-dimensional one (we work on the cross section) in polar coordinates. Boundary conditions are as presented before:

(i) The electric potential should remain finite inside the cylinder: $V_i(0,\theta)$ has to be bounded;

(ii) The electric potential across the interface should be continuous: $V_i(r_0,\theta) = V_o(r_0,\theta)$;

(iii) The normal component of electric current density should be continuous across the interface: $\sigma_i \dfrac{\partial V_i(r_0,\theta)}{\partial r} = \sigma_o \dfrac{\partial V_o(r_0,\theta)}{\partial r}$

(iv) The electric potential far away from the cylinder behaves as: $V_o(r,\theta) = E_\infty r \cos\theta$.

It then follows that:

- $\sin\theta$ do not appear in the boundary conditions, so $B_1 = D_1 = 0$ and consequently:

$$V^{(1)}(r,\theta) = A_0 \ln r + B_0 + rA_1 \cos\theta + \frac{C_1 \cos\theta}{r}; \quad (3.84)$$

- since the internal potential should be bounded – boundary condition (i) – it must be $A_0^i = C_1^i = 0$ to avoid divergences at $r = 0$;
- application of boundary condition (iv) implies that $A_0^o = 0$ (in fact there is no logarithmic dependence), $A_1^o = E_\infty$ and $C_1^o \neq 0$ (to ensure that V_i and V_o are different);
- boundary condition (iii) yields a condition for $C_1^o = r_0^2[E_\infty - RA_1^i]$;
- from the remaining (ii), two relations emerge:

  $$B_0^i = B_0^o$$

  that can be put to zero for convenience; collecting all $\cos\theta$ terms one gains:

  $$C_1^o = r_0^2[A_1^i - E_\infty]$$

  that combined with the other expression gives:

  $$A_1^i = \frac{2E_\infty}{1+R}$$

  and

  $$C_1^o = r_0^2 E_\infty \frac{1-R}{1+R}.$$

Inserting the expressions for the coefficients in the $V^{(1)}$ expansion for V_i and V_o gives back equations (2.75) and (2.76).

Appendix B

This part presents a more detailed description of the setup of the platform. It has been adapted from [25].

Experimental setup

The experimental setup employed can be divided in two parts, reported in figures 3.30 and 3.31. The first one (figure 3.30) is related to the optofluidic coupling, i.e. the control of the flows inside the optofluidic platform described in the previous sections and the coupling of the waveguides, while the second one (figure 3.31) is devoted to the illumination of the Fe:LN sample integrated in the aforementioned platform (the chip is the same reported in figure 3.30).

The pump setup employed to inject the fluids in the microchannels is the OB1 MK3 pressure driver pump equipped with 3 channels with a range 0-8 bar (Elveflow, Paris, France). The flows control was achieved by a feedback system provided by the coupling of three flowmeters BFS Coriolis10 (Bronkhorst, AK Ruurlo, Holland) to the main pressure driver (figure 3.30, on the left).

The coupling of the waveguides with laser light was achieved by employing a near field system (see figure 3.32). A continuous diode laser with power of 7.35 mW and a wavelength $\lambda = 532$ nm was coupled to the single waveguide. An half plate and a polarizer were added, so that both the TE and TM mode of the waveguide can be excited. The optofluidic device is mounted on a platform with 6 degrees of freedom, which allows translation and rotation of the sample. Laser light is collected by a 20X Objective, is focused on and coupled to the single waveguide by properly setting the platform, and it is then recollected by a long working distance 50X Objective. The output light was coupled to a silicon photodiode and amplified by means of a transimpedance amplifier, whose signal was then collected by the acquisition fast card Ni 6023.

Several techniques to couple laser light inside a waveguide have been developed, for example prism couplers [65] and permanent pigtailing [66]. The latter, in particular, offers the optimal features for an optofluidic application, since it is permanent, stable and portable. However, it does not represent the best solution for this work, since it does not ensure flexibility during the test phase. The direct coupling exploited in this thesis, achieved by means of Objectives, is a reliable alternative. The main drawback is the fact that the coupling is not permanent, thus requiring recoupling procedures after a measurement.

The experimental apparatus showed in figure 3.31 is straightforward: a solid state laser, with a nominal power of 100 mW, is employed to illuminate the iron-doped lithium niobate sample integrated in the optofluidic platform. It has to be noted however that the real power provided during the acquisitions, measured with a semiconductor power sensor connected to FieldMaxII-TO Power Meter (Coeherent Inc., Santa Clara, CA, USA) ranges from 43.0 mW up to 65.0 mW.

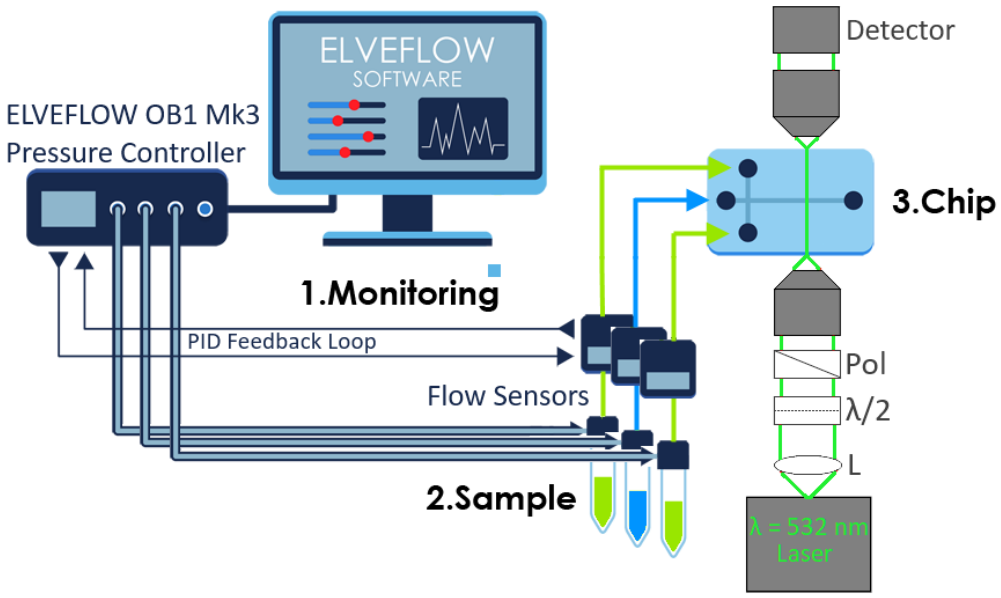

Figure 3.30: Experimental setup to achieve the control of the flows inside the microchannels and the coupling of the waveguides.

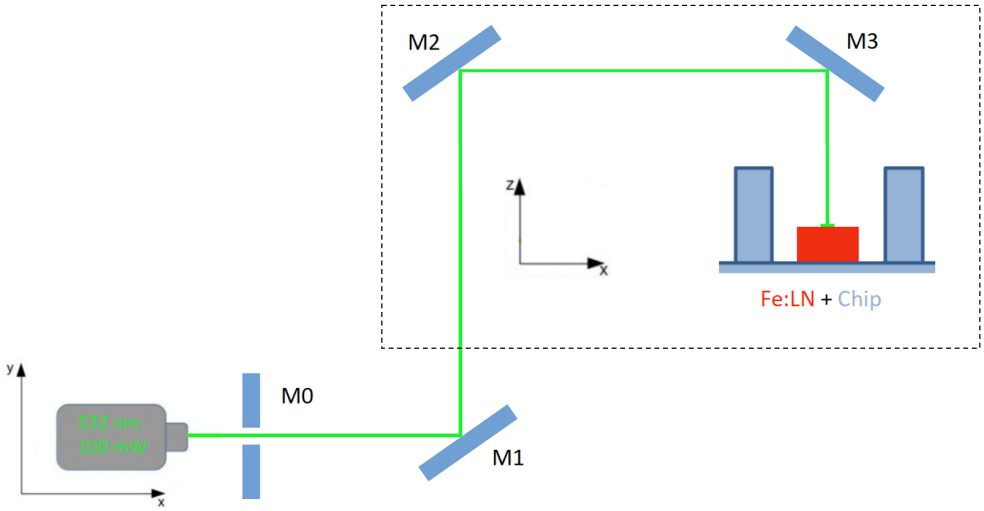

Figure 3.31: Scheme of the optical apparatus devoted to the illumination of the Fe:LN sample. M0, M1, M2 and M3 are mirrors.

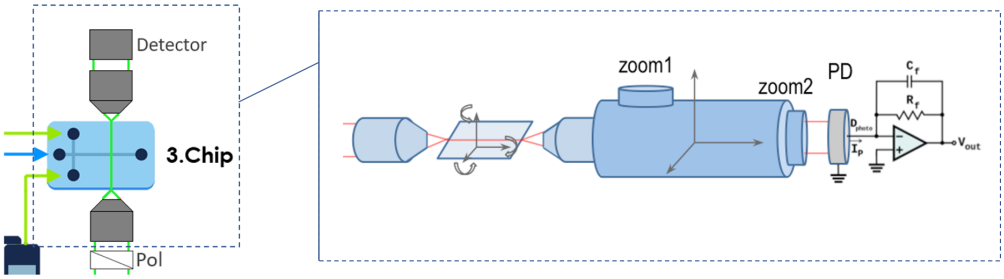

Figure 3.32: Scheme of the near field system for coupling the waveguides to the laser light and collecting the output.

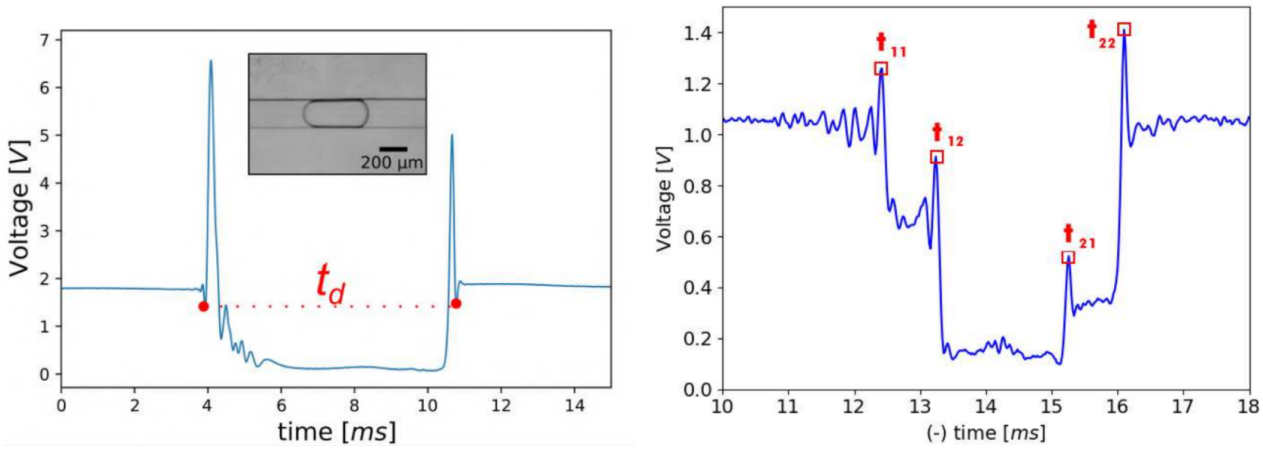

(a) (b)

Figure 3.33: Examples of acquired signals during the transit of a droplet in front of a straight waveguide (3.33a) and a Mach-Zehnder one (3.33b). Both graphs are taken from [36].

Optical trigger

The optofluidic setup presented in the previous section and reported in figure 3.31 acts as an optical trigger for detecting flowing objects in the microchannels such as, as in the case of this work, droplets. The study can be carried out by measuring droplets lengths and velocities in different moments before, during and after the illumination. Therefore, a reliable and versatile optofluidic configuration is needed. In fact, the reason behind the choice of MZI configuration for the integrated waveguides is connected to its versatility and independence from any type of previous calibration with additional imaging setups or other integrated stages. To provide an example, it is possible to compare straight waveguides and Mach-Zehnder ones in terms of measurement of droplets' lengths and velocities. Figure 3.33 shows two examples corresponding to the two different acquired signals, with a straight waveguide (3.33a) and a Mach-Zehnder one (3.33b), when droplets of MilliQ dispersed in hexadecane are produced [36].

In the first case (3.33a), the time passage Δt (t_d) that can be obtained from the signal is an effective indirect measurement of the droplet velocity v, being $v = L/\Delta t$, where L is droplet's length. In this case, the measurement of the velocity is always correlated to the length and it is therefore required a preliminary calibration, for example, as mentioned before, with an imaging system.

The waveguide in MZI configuration is a way to avoid this inconvenient and make the device more versatile. In this case, actually, the crucial upgrade consists in employing two different points at a known distance, indicated as $2W$, as reference, which are the two straight sections of the Mach-Zehnder waveguide. As can be seen in figure 3.33b, taking into account also figure 3.34a for a better visualization, when a droplet with length $L > 2W$ transit in front of an illuminated optical MZI waveguide, the trigger times are four: t_{11} corresponds to the interaction between the front droplet's meniscus with the first MZI arm, t_{12} represents the interaction between the front meniscus with the second arm, t_{21} is the instant of time corresponding to the transit of the rear meniscus in front of the first arm and at t_{22} the rear meniscus is exiting from the second MZI arm. As it can be noticed, t_{11} and t_{12} are connected to a drop of the transmitted signal, since the presence of the droplet scatters the transmitted light and it has a refractive index lower than hexadecane's one, respectively $1.33 < 1.43$. The opposite holds for t_{21} and t_{22}. Once determined the four trigger times, both velocities of front and rear meniscus can be obtained as:

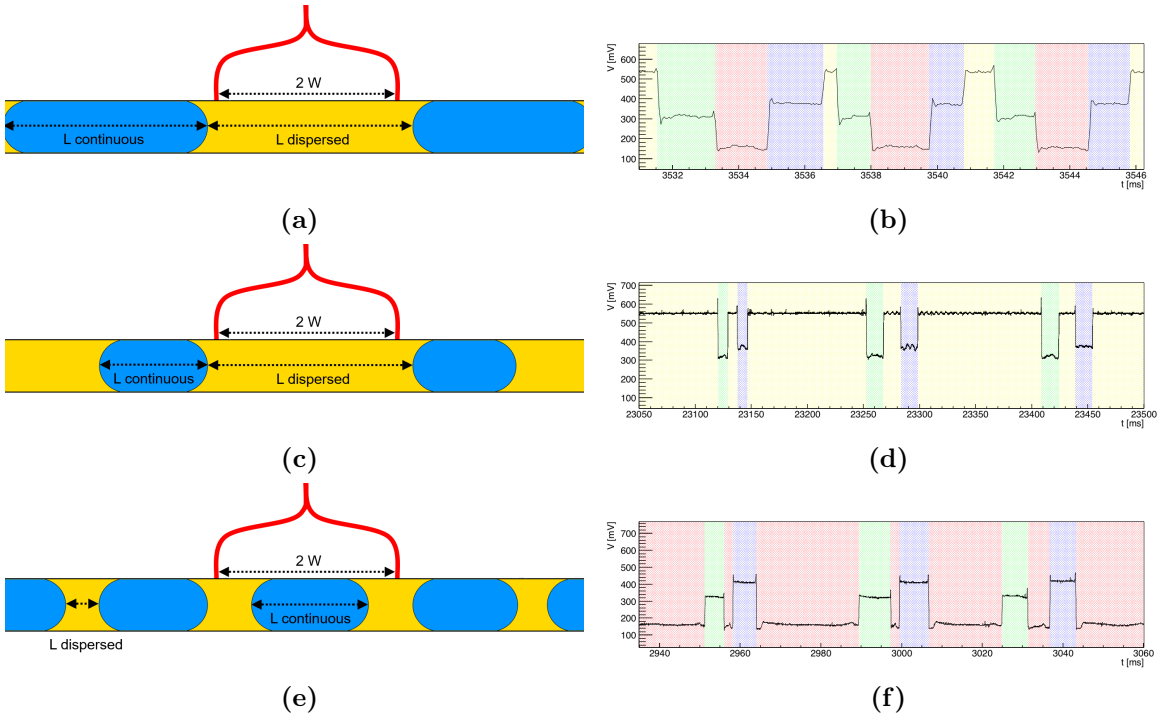

Figure 3.34: On the left, sketches of three different regimes in terms of acquired signal behaviour, depending on the ratio $R = L/2W$ and the distance between consecutive droplets. In particular, 3.34a corresponds to $R > 1$, while 3.34c and 3.34e to $R < 1$. On the right, the three graphs report the respective signals. The yellow highlighted plateaus represent the case in which both arms are transmitting through oil inside the channel, the red one when a droplet covers both arms, the green and blue when only one of the two arms is covered by a droplet. The images are taken from [36].

$$\begin{aligned} v_{front} &= \frac{2W}{t_{12} - t_{11}} \\ v_{rear} &= \frac{2W}{t_{22} - t_{21}} \end{aligned} \tag{3.85}$$

and the estimation of the single droplet's velocity v is obtained performing the average between these two values. Similarly, from v_{front} and v_{rear}, two lengths can be calculated as:

$$\begin{aligned} L_1 &= v_{front}\,(t_{21} - t_{11}) \\ L_2 &= v_{rear}\,(t_{22} - t_{12}) \end{aligned} \tag{3.86}$$

and the average droplet's length Lcan be obtained by averaging L_1 and L_2.
In this work, $2W = 40$ μm and all the droplets produced are such that their length is $L > 2W$. However, this is not the only working regime that can be achieved in terms of signal [36]. As can be seen in figure 3.34, the differences between the three presented regimes are the ratio $L/2W$, where L is the droplet's length, and the distance between two consecutive droplets. However, as previously stated, the only working condition considered here is the one such that $L/2W > 1$, which is also the only regime with univocal matching between droplets in the microchannel and acquired signal.
An optofluidic device with MZI waveguides integrated in lithium niobate has been characterized and successfully validated in [36; 67], where the main application was the employment of such platform as a droplets velocimeter. The aforementioned $LiNbO_3$ platform was demonstrated to be a reliable integrated device for velocities measurements of flowing objects inside

a microchannel, with precision up to three times higher than the one guaranteed by a standard video camera microscope setup.

Bibliography

[1] W. A. Macky and Charles Thomson Rees Wilson. Some investigations on the deformation and breaking of water drops in strong electric fields. *Proceedings of the Royal Society of London. Series A, Containing Papers of a Mathematical and Physical Character*, 133(822):565–587, 1931.

[2] Chester T. O'Konski and Henry C. Jr. Thacher. The distortion of aerosol droplets by an electric field. *The Journal of Physical Chemistry*, 57(9):955–958, 1953.

[3] Geoffrey Ingram Sir Taylor. Studies in electrohydrodynamics. i. the circulation produced in a drop by an electric field. *Proceedings of the Royal Society of London. Series A. Mathematical and Physical Sciences*, 291:159 – 166, 1966.

[4] Lorenzo De Bortoli. Study of light driven phenomena in integrated opto-microfluidic lithium niobate platforms. 2017.

[5] Md. Abdul Halim and Asghar Esmaeeli. Computational studies on the transient electrohydrodynamics of a liquid drop. *Fluid Dynamics & Materials Processing*, 9(4):435–460, 2013.

[6] Matthew Foreman, Saverio Avino, Rosa Zullo, Hans-Peter Loock, Frank Vollmer, and Gianluca Gagliardi. Enhanced nanoparticle detection with liquid droplet resonators. *Eur. Phys. J. Spec. Top.*, 223:1971–1988, 09 2014.

[7] Dominik G. Rabus, Cinzia Sada, and Karsten Rebner. *Optofluidics*. De Gruyter, Berlin, Boston, 2019.

[8] James Q. Feng. Dielectrophoresis of a deformable fluid particle in a nonuniform electric field. *Phys. Rev. E*, 54:4438–4441, 1996.

[9] Mariusz Gadzinowski, Damian Mickiewicz, and Teresa Basinska. Spherical versus prolate spheroidal particles in biosciences: Does the shape make a difference? *Polymers for Advanced Technologies*, 32(10):3867–3876, 2021.

[10] Jean Berthier. *Microdrops and Digital Microfluidics*. Elsevier, 2012.

[11] D. A. Saville. Electrohydrodynamics: The taylor-melcher leaky dielectric model. *Annual Review of Fluid Mechanics*, 29:27–64, 1997.

[12] Chapter 1 - interaction of colloidal particles. In Hiroyuki Ohshima and Kimiko Makino, editors, *Colloid and Interface Science in Pharmaceutical Research and Development*, pages 1–28. Elsevier, Amsterdam, 2014.

[13] G.K. Batchelor. *An Introduction to Fluid Dynamics*. Cambridge mathematical library. Cambridge University Press, 2000.

[14] Debasish Das and David Saintillan. Electrohydrodynamics of viscous drops in strong electric fields: numerical simulations. *Journal of Fluid Mechanics*, 829:127–152, 2017.

[15] Etienne Lac and G. M. Homsy. Axisymmetric deformation and stability of a viscous drop in a steady electric field. *Journal of Fluid Mechanics*, 590:239–264, 2007.

[16] Marrivada N. Reddy and Asghar Esmaeeli. The ehd-driven fluid flow and deformation of a liquid jet by a transverse electric field. *International Journal of Multiphase Flow*, 35:1051–1065, 2009.

[17] Satoru Moriya, Keiichiro Adachi, and Tadao Kotaka. Deformation of droplets suspended in viscous media in an electric field. 1. rate of deformation. *Langmuir*, 2(2):155–160, 1986.

[18] Asghar Esmaeeli and Payam Sharifi. The transient dynamics of a liquid column in a uniform transverse electric field of small strength. *Journal of Electrostatics*, 69(6):504–511, 2011.

[19] Shubhadeep Mandal, Aditya Bandopadhyay, and Suman Chakraborty. The effect of uniform electric field on the cross-stream migration of a drop in plane poiseuille flow. *Journal of Fluid Mechanics*, 809:726–774, 2016.

[20] Shubhadeep Mandal, Suryapratim Chakrabarti, and Suman Chakraborty. Effect of nonuniform electric field on the electrohydrodynamic motion of a drop in Poiseuille flow. *Physics of Fluids*, 29(5):052006, 2017.

[21] J.J. Stoker. *Differential Geometry*. Wiley Classics Library. Wiley, 1989.

[22] Petia M. Vlahovska. Electrohydrodynamics of drops and vesicles. *Annual Review of Fluid Mechanics*, 51(1):305–330, 2019.

[23] Asghar Esmaeeli and Ali Behjatian. Equilibrium shape and hysteresis behavior of liquid jets in transverse electric fields. *Journal of Electrostatics*, 75:5–13, 2015.

[24] RS Weis and TK Gaylord. Lithium niobate: summary of physical properties and crystal structure. *Applied Physics A*, 37(4):191–203, 1985.

[25] Giovanni Bragato. Study of light-driven phenomena for opto-microfluidic sensing on multifunctional lithium niobate platforms. 2021.

[26] Tatyana Volk and Manfred Wöhlecke. *Lithium niobate: defects, photorefraction and ferroelectric switching*, volume 115. Springer Science & Business Media, 2008.

[27] Armin Räuber. Chemistry and physics of lithium niobate. *Current topics in materials science*, 1:481–601, 1978.

[28] Chihiro Koyama, Jun Nozawa, Kozo Fujiwara, and Satoshi Uda. Effect of point defects on curie temperature of lithium niobate. *Journal of the American Ceramic Society*, 100(3):1118–1124, 2017.

[29] Ed L Wooten, Karl M Kissa, Alfredo Yi-Yan, Edmond J Murphy, Donald A Lafaw, Peter F Hallemeier, David Maack, Daniel V Attanasio, Daniel J Fritz, Gregory J McBrien, et al. A review of lithium niobate modulators for fiber-optic communications systems. *IEEE Journal of selected topics in Quantum Electronics*, 6(1):69–82, 2000.

[30] Uwe Schlarb and Klaus Betzler. Refractive indices of lithium niobate as a function of temperature, wavelength, and composition: A generalized fit. *Physical Review B*, 48(21):15613, 1993.

[31] M Luennemann, U Hartwig, G Panotopoulos, and K Buse. Electrooptic properties of lithium niobate crystals for extremely high external electric fields. *Applied Physics B*, 76(4):403–406, 2003.

[32] E Bernal, GD Chen, and TC Lee. Low frequency electro-optic and dielectric constants of lithium niobate. *Physics Letters*, 21(3):259–260, 1966.

[33] VM Fridkin. Bulk photovoltaic effect in noncentrosymmetric crystals. *Crystallography Reports*, 46(4):654–658, 2001.

[34] AM Glass, D von der Linde, and TJ Negran. High-voltage bulk photovoltaic effect and the photorefractive process in linbo3. In *Landmark Papers On Photorefractive Nonlinear Optics*, pages 371–373. World Scientific, 1995.

[35] Giacomo Bettella. Integrated opto-microfluidic lab-on-a-chip in lithium niobate for droplet generation and sensing. 2016.

[36] Riccardo Zamboni. Study of light driven phenomena for optofluidic applications in lab-on-a-chip platforms in lithium niobate. 2019.

[37] Annamaria Zaltron. Local doping of lithium niobate by iron diffusion: a study of photorefractive properties. 2011.

[38] Peter Günter, Jean-Pierre Huignard, and Alastair M Glass. *Photorefractive materials and their applications*, volume 1. Springer, 1988.

[39] NV Kuhktarev, VB Markov, SG Odulov, MS Soskin, and VL Vinetskii. Holographic storage in electrooptic crystals. *Ferroelectrics*, 22(949):949–960, 1979.

[40] K Peithmann, A Wiebrock, and K Buse. Photorefractive properties of highly-doped lithium niobate crystals in the visible and near-infrared. *Applied Physics B*, 68(5):777–784, 1999.

[41] E Krätzig and R Orlowski. Litao 3 as holographic storage material. *Applied physics*, 15(2):133–139, 1978.

[42] D Kip, J Hukriede, and E Krätzig. Holographic measurement of dark conductivity in linbo˜ 3: Ti: Fe planar optical waveguides. *PHYSICA STATUS SOLIDI A APPLIED RESEARCH*, 168:R3–R4, 1998.

[43] R Sommerfeldt, L Holtman, E Krätzig, and BC Grabmaier. Influence of mg doping and composition on the light-induced charge transport in linbo3. *physica status solidi (a)*, 106(1):89–98, 1988.

[44] L Lucchetti, K Kushnir, V Reshetnyak, F Ciciulla, A Zaltron, C Sada, and F Simoni. Light-induced electric field generated by photovoltaic substrates investigated through liquid crystal reorientation. *Optical Materials*, 73:64–69, 2017.

[45] George M Whitesides. The origins and the future of microfluidics. *nature*, 442(7101):368–373, 2006.

[46] Chun-Xia Zhao and Anton PJ Middelberg. Two-phase microfluidic flows. *Chemical Engineering Science*, 66(7):1394–1411, 2011.

[47] Riccardo Zamboni. Optofluidic application of a mach-zehnder interferometer integrated in lithium niobate for droplet sensing. 2016.

[48] Xavier Casadevall i Solvas and Andrew DeMello. Droplet microfluidics: recent developments and future applications. *Chemical Communications*, 47(7):1936–1942, 2011.

[49] Charles N Baroud, Francois Gallaire, and Rémi Dangla. Dynamics of microfluidic droplets. *Lab on a Chip*, 10(16):2032–2045, 2010.

[50] George M Whitesides, Abraham D Stroock, et al. Flexible methods for microfluidics. *Phys. Today*, 54(6):42–48, 2001.

[51] Jessamine MK Ng, Irina Gitlin, Abraham D Stroock, and George M Whitesides. Components for integrated poly (dimethylsiloxane) microfluidic systems. *Electrophoresis*, 23(20):3461–3473, 2002.

[52] G Bettella, Riccardo Zamboni, G Pozza, A Zaltron, C Montevecchi, M Pierno, G Mistura, C Sada, L Gauthier-Manuel, and Mathieu Chauvet. Linbo3 integrated system for opto-microfluidic sensing. *Sensors and Actuators B: Chemical*, 282:391–398, 2019.

[53] Pingan Zhu and Liqiu Wang. Passive and active droplet generation with microfluidics: a review. *Lab on a Chip*, 17(1):34–75, 2017.

[54] Piotr Garstecki, Michael J Fuerstman, Howard A Stone, and George M Whitesides. Formation of droplets and bubbles in a microfluidic t-junction—scaling and mechanism of break-up. *Lab on a Chip*, 6(3):437–446, 2006.

[55] Gordon F Christopher, N Nadia Noharuddin, Joshua A Taylor, and Shelley L Anna. Experimental observations of the squeezing-to-dripping transition in t-shaped microfluidic junctions. *Physical Review E*, 78(3):036317, 2008.

[56] Howard A Stone. On lubrication flows in geometries with zero local curvature. *Chemical engineering science*, 60(17):4838–4845, 2005.

[57] Li Lei, Yuting Zhao, Wukai Chen, Huiling Li, Xinyu Wang, and Jingzhi Zhang. Experimental studies of droplet formation process and length for liquid–liquid two-phase flows in a microchannel. *Energies*, 14(5):1341, 2021.

[58] M. Chauvet C. Sada Cinzia R. Zamboni, A. Zaltron. Real-time precise microfluidic droplets label-sequencing combined in a velocity detection sensor. *Scientific reports*, 11(1):1–12, 2021.

[59] S.G. Odulov M.S. Soskin V.L. Vinetskii N.V. Kukhtarev, B V.B.Markov. Holographic storage in electrooptic crystals.: I. steady state. In *Landmark Papers On Photorefractive Nonlinear Optics*, pages 37–48. World Scientific, 1995.

[60] J.P. Huignard P. Günter. *Photorefractive materials and their applications*, volume 114. Springer, Germany, 2007.

[61] Riccardo Zamboni, Annamaria Zaltron, Davide Ferraro, and Cinzia. Sada. Droplet transition from non-axisymmetric to axisymmetric shape: Dynamic role of lubrication film in a rectangular microfluidic channel. *Physics of Fluids*, 34(12):122014, 2022.

[62] Hans J Weber and George B Arfken. *Essential mathematical methods for physicists, ISE*. Elsevier, 2003.

[63] E.D. Alcock. The effect of an electric field on the viscosity of liquids. *Physics*, 7(3):126–129, 1936.

[64] C. Dodd E. Andrade, Neville Da Costa. The effect of an electric field on the viscosity of liquids. *Proceedings of the Royal Society of London. Series A. Mathematical and Physical Sciences*, 187(1010):296–337, 1946.

[65] PK Tien and R Ulrich. Theory of prism–film coupler and thin-film light guides. *JOSA*, 60(10):1325–1337, 1970.

[66] E Murphy, T Rice, Leon McCaughan, G Harvey, and P Read. Permanent attachment of single-mode fiber arrays to waveguides. *Journal of lightwave technology*, 3(4):795–799, 1985.

[67] Giovanni Bragato. Velocimetro per gocce microfluidiche basato su di un interferometro fotonico integrato in niobato di litio. 2019.

[68] Jako Greuters and Nadeem Hasan Rizvi. Uv laser micromachining of silicon, indium phosphide, and lithium niobate for telecommunications applications. In *Opto-Ireland 2002: Optics and Photonics Technologies and Applications*, volume 4876, pages 479–486. International Society for Optics and Photonics, 2003.

[69] Rafael R Gattass and Eric Mazur. Femtosecond laser micromachining in transparent materials. *Nature photonics*, 2(4):219–225, 2008.

[70] Roberto Osellame, Giulio Cerullo, and Roberta Ramponi. *Femtosecond laser micromachining: photonic and microfluidic devices in transparent materials*, volume 123. Springer Science & Business Media, 2012.

[71] Jintian Lin, Yingxin Xu, Zhiwei Fang, Min Wang, Jiangxin Song, Nengwen Wang, Lingling Qiao, Wei Fang, and Ya Cheng. Fabrication of high-q lithium niobate microresonators using femtosecond laser micromachining. *Scientific reports*, 5(1):1–4, 2015.

[72] Manoj Sridhar, Devendra K Maurya, James R Friend, and Leslie Y Yeo. Focused ion beam milling of microchannels in lithium niobate. *Biomicrofluidics*, 6(1):012819, 2012.

[73] Stephen Winnall and Saul Winderbaum. Lithium niobate reactive ion etching. Technical report, DEFENCE SCIENCE AND TECHNOLOGY ORGANIZATION SALISBURY (AUSTRALIA), 2000.

[74] Sean M Langelier, Leslie Y Yeo, and James Friend. Uv epoxy bonding for enhanced saw transmission and microscale acoustofluidic integration. *Lab on a Chip*, 12(16):2970–2976, 2012.

[75] M Chauvet, L Al Fares, B Guichardaz, F Devaux, and S Ballandras. Integrated optofluidic index sensor based on self-trapped beams in linbo3. *Applied Physics Letters*, 101(18):181104, 2012.

[76] Giacomo Bettella, Gianluca Pozza, Sebastian Kroesen, Riccardo Zamboni, Enrico Baggio, Carlo Montevecchi, Annamaria Zaltron, Ludovic Gauthier-Manuel, Giampaolo Mistura, Claudio Furlan, et al. Lithium niobate micromachining for the fabrication of microfluidic droplet generators. *Micromachines*, 8(6):185, 2017.

[77] Rita Scolaro. Studio dei fenomeni di intrappolamento di sistemi microscopici indotti dalla luce in cristalli di niobato di litio. 2016.

[78] Cándido Arregui, JB Ramiro, A Alcázar, A Méndez, Juan F Muñoz-Martínez, and M Carrascosa. Comparative theoretical analysis between parallel and perpendicular geometries for 2d particle patterning in photovoltaic ferroelectric substrates. *Journal of the European Optical Society-Rapid publications*, 10, 2015.

[79] Alvaro Mata, Aaron J Fleischman, and Shuvo Roy. Characterization of polydimethylsiloxane (pdms) properties for biomedical micro/nanosystems. *Biomedical microdevices*, 7(4):281–293, 2005.

[80] Jonathan Bennès, Sylvain Ballandras, and Frederic Cherioux. Easy and versatile functionalization of lithium niobate wafers by hydrophobic trichlorosilanes. *Applied Surface Science*, 255(5):1796–1800, 2008.

[81] Marco Bazzan and Cinzia Sada. Optical waveguides in lithium niobate: Recent developments and applications. *Applied Physics Reviews*, 2(4):040603, 2015.

[82] G Griffiths and R Esdaile. Analysis of titanium diffused planar optical waveguides in lithium niobate. *IEEE Journal of Quantum electronics*, 20(2):149–159, 1984.

[83] Ovidio Peña-Rodríguez, José Olivares, Mercedes Carrascosa, Ángel García-Cabañes, Antonio Rivera, and Fernando Agulló-López. Optical waveguides fabricated by ion implantation/irradiation: A review. *Ion implantation*, pages 978–953, 2012.

[84] Masaharu Fukuma, Juichi Noda, and Hiroshi Iwasaki. Optical properties in titanium-diffused linbo3 strip waveguides. *Journal of Applied Physics*, 49(7):3693–3698, 1978.

[85] S Fouchet, Alain Carenco, C Daguet, R Guglielmi, and Luc Riviere. Wavelength dispersion of ti induced refractive index change in linbo 3 as a function of diffusion parameters. *Journal of lightwave technology*, 5(5):700–708, 1987.

[86] Geoffrey Ingram Sir Taylor. Disintegration of water drops in an electric field. *Proceedings of the Royal Society of London. Series A. Mathematical and Physical Sciences*, 280:383–397, 1964.

[87] Limin He, Xin Huang, Xiaoming Luo, Haipeng Yan, Yuling Lü, Donghai Yang, and Yunrui Han. Numerical study on transient response of droplet deformation in a steady electric field. *Journal of Electrostatics*, 82:29–37, 2016.